Cataloguing of Objects on High and Intermediate Altitude Orbits

vorgelegt von

Johannes Herzog

von Deutschland

Cataloguing of Objects on High and Intermediate Altitude Orbits

Contents

Contents

Contents

IV

List of Figures

List of Figures

List of Tables

List of Tables

VIII

List of Abbreviations and Acronyms

$\mathcal{A}$
AIUB . . . . Astronomical Institute of the University of Berne
ALOS . . . . Advanced Land Observing Satellite
AMR . . . . Area-to-Mass Ratio
ASA . . . . Astrosysteme Austria

$\mathcal{C}$
CNES . . . . Centre National d'études Spatiales

$\mathcal{D}$
d.o.f. . . . . Degrees Of Freedom
DRP . . . . Direct Radiation Pressure

$\mathcal{E}$
ESA . . . . European Space Agency
ESASDT . . . . ESA Space Debris Telescope
EWSK . . . . East-West station-keeping

$\mathcal{F}$
FoV . . . . Field of View

$\mathcal{G}$
GEO . . . . Geostationary Ring
GLONASS . . . . Globalnaja Nawigazionnaja Sputnikowaja Sistema
GNSS . . . . Global Navigation Satellite System
GTO . . . . Geostationary Transfer Objects

$\mathcal{H}$
HAMR . . . . High Area-to-Mass Ratio Objects

$\mathcal{I}$
ISON . . . . International Scientific Optical observation Network
ISS . . . . International Space Station
IAA . . . . International Academy of Astronautics

List of Abbreviations and Acronyms

> Space: the final frontier. The
> mission: to explore strange new
> worlds and to boldly go where no
> man has gone before
>
> ———————————————
> based loosely on Star Trek

Since the beginning of space age the set of problems concerning space debris is unsolved. The International Academy of Astronautics (IAA) defined in 1993 the term orbital debris (synonym of space debris, [IAA 93]):
Orbital debris is herein defined as any man-made object, which is non-functional with no reasonable expectation of assuming or resuming its intended function, or any other function for which it is or can be expected to be authorized, including fragments and parts thereof.

The definition does not state anything about the origin or creation of space debris, which implies that every kind of inactive objects in space, may it be created by intention, accident, ageing or erosion, counts as space debris. The most obvious mechanism is the shut down at the end of the life time of a satellite.

It is remarkable that the first definition of space debris was written around 36 years after the start of the Space Era. Yet in the 80's of the 20th century only experts got involved in the topic of space debris.

The population of space debris does not only consist of non-functional satellites but also rocket bodies or fragments thereof. This may happen by ageing like temperature differences between passages through the Sun and shadow of the Earth, ageing through ultra-violet and X-ray radiation, respectively. Collisions and explosions do not only destroy objects completely, but also create large amounts of fragments. Another, but comparably small group of space debris objects consists of lost equipment of crewed spaceflights.

The first artificial object sent into an orbit around the Earth was the satellite Sputnik 1 in 1957. It lasted about three month in orbit before it re-entered into Earth's atmosphere and eventually burned up. In the end nothing of the whole launch created space debris, but it was the key for every further space mission, considering that is was the start of the Cold War Space Race, too.

The next milestone in history of space debris was Vanguard I, a satellite of the US-American Space Agency NASA. This satellite was launched in 1958 to get information about the shape of the Earth. It was the first satellite with solar cells for self-sufficient energy production. The mission lasted more than six years until the solar cell powered transmitter finally broke down. Its secondary mission was to get information about the atmospheric drag. Due to the Solar radiation pressure the satellite was moved approximately 1600 km out of its orbital plane within the first 28 month, but still (as of 2013) its orbit is stable. This satellite was the first space debris object in the sense of a decommissioned satellite and is expected to stay there about 240 more years (see e. g. [NASAc]).

One of the first space debris object created by accident was a spare thermal glove of Edward Higgins White II (1930 − 1967), first US-American on a space walk and pilot of the Gemini 4 mission in 1965. It

floated away through the open hatch of the spacecraft while White was on a walk in space. The glove did not remain in orbit for a long time as it re-entered and eventually burned up in the Earth's atmosphere.

As time went by, more and more countries started their own satellite missions: for example Great Britain and Canada in 1962, France in 1965 and Germany in 1969. Although many objects re-entered into the atmosphere, the number of abandoned satellites, upper stages and rocket bodies increased.
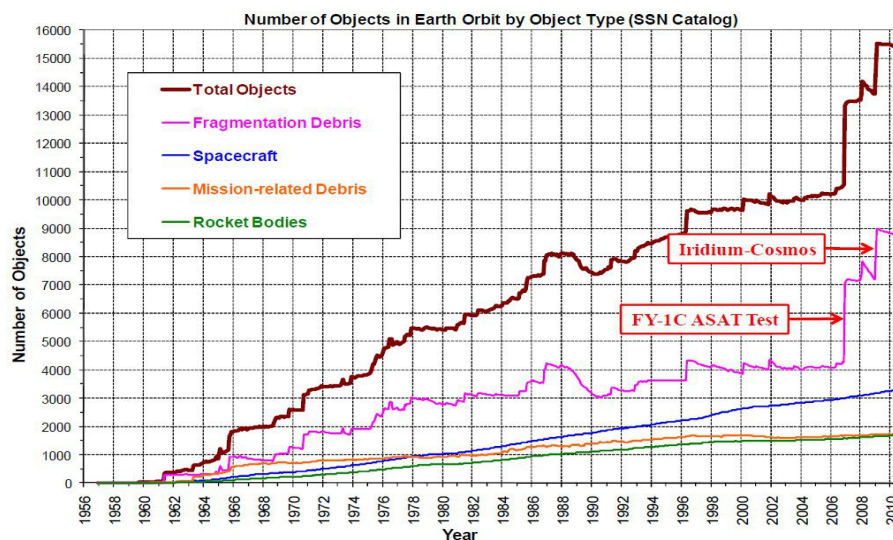
Figure 0.1: Number of objects in an orbit around the Earth by year and object type (taken from [Liou 10])

In Fig. 0.1 one can see the increasing number of objects in orbits around the Earth. The total number of objects (brown line) has increased constantly during the years but in 2007 and 2009, respectively, two incidents provoked a sudden increase of the total number of particles and brought the problem of space debris again to mind. With the pink increase at the same epochs, it is clear that the increase of the total number is related to an increase of fragmentation debris.

1. On January 11, 2007 the Chinese weather satellite Fengyun-1C was destroyed by a Chinese intermediate-range missile. Ignoring the fact of a military arms race in space, the destruction created a huge amount (at least 3000 pieces) of space debris, partly on orbits where they will stay for a long time. Therefore they are a possible threat for future space missions.

2. Another event to mention here was a collision of two satellites on February 10, 2009. The non-functional Cosmos 2251 satellite collided with the active Iridium 33, with both completely destroyed. The position of the Cosmos 2251 satellite was unknown as it was not observed anymore. In this case the minimal distance was predicted to be approximately 580 m, which is large enough that both satellites could have passed each other. Referring to Fig. 0.1, the collision created a total amount of 2000 pieces and, again, some of them are dangerous for upcoming space missions.

Other incidents which were reported detailed in the media:

1. On November 18, 2008, astronaut Heidemarie Stefanshyn-Piper (born 1963) lost a tool bag on a walk in space. Unfortunately for her, it was recorded by a camera on the outside of the ISS and later published in many internet platforms and news. But, due to its low orbit of less than 400 km it decayed and burned up in the Earth's atmosphere on August 3, 2009.

2. During 2011 two non-functional satellites re-entered the Earth's atmosphere, but did not burn up completely: first the satellite UARS (91063B) which re-entered on September 24th over the Pacific Ocean (see [NASAb]) and then the satellite ROSAT (90049A) on October 23rd (see e. g. [DLR]).

Re-entries of satellites at the end of their life time is the only method to avoid space debris. They are decelerated and heated by the atmosphere of the Earth and eventually they break up. Several part will burn up completely, but for each re-entry it is possible that the largest parts may reach the surface of the Earth. This method is only applicable for LEO satellites, rocket bodies on highly elliptical orbits, which interact with the outer layer s of the atmosphere of the Earth, need decades to re-enter.

For each re-entering satellite, the location of the of the re-entry is uncertain for a long time. Only within the last two to three orbital periods it can be estimated, meaning that regions on the Earth's surface, which might be at risk, can only be alarmed on short notice. The mass and number of fragments which will reach the surface of the Earth is also unknown, but with simulations an approximation can be made.

Every other object remaining in an orbit around the Earth is a possible threat. Even objects with diameters smaller than 1 cm can cause a catastrophic collision, resulting in a breakdown of the satellite.

The presented events shall make one point clear: not only a satellite's mission but also by intention or accident the amount of space debris increases. Even a collision event cannot be prevented by observing regularly in certain regions of the sky, but with knowing as much as possible how many objects are revolving around the Earth and in which orbits, one can determine collision probabilities more precisely.

But observing objects and building up an object catalogue is only a start, that catalogue has to be maintained, which means that the objects have to be observed regularly. Only this way a determination of an orbit which is accurate enough to predict the orbit several days into the future.

The maintenance may be a difficult task, when there are little observations due to bad weather conditions or technical problems. Also, an increasing number of objects in the catalogue may make it more difficult to observe each object often enough to maintain its orbit. Therefore observation strategies have to be developed to compensate periods without observations and observe as much objects as possible within one night.

Considering the points mentioned above, this thesis will focus on the following questions: which strategies are optimal for ZimSMART to observe objects in different orbit regions, what must processing algorithms take into account to link successfully observations of one night and/or several nights, respectively, and is there anything else, which has to be taken into account?

The work of this dissertation will answer these questions by analysing observations of ZimSMART.

Motivation

Chapter 1

Introduction

1.1 Protected Regions and Object Classification

Each orbiting object, satellite or space debris, is classified roughly by its semi-major axis. In general, there are two protected regions with specific requirements for the satellites: at the end of the life time a satellite has to re-enter the Earth's atmosphere and burn up or has to to be put into so-called graveyard orbits. Both strategies are meant to prevent collisions and the creation of space debris in heavily used orbit regions. The protected regions are shown in Figure 1.1 with their altitude above the Earth's surface. The numbers of both regions are taken from [IADC 02].
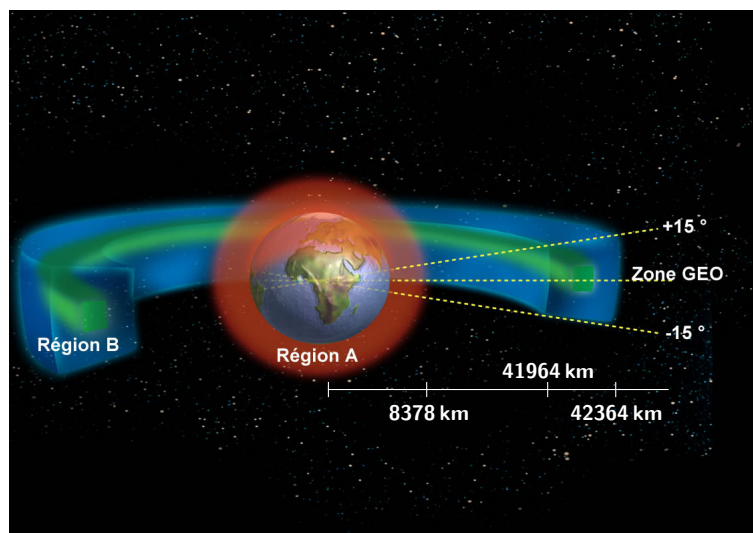
Figure 1.1: Protected regions of orbits around the Earth (figure not to scale, [CNES], numbers taken from [IADC 02])

The first protected region (Région A in Fig. 1.1) and closest to Earth is the region of the Low Earth Orbits (LEO), up to a semi-major axis of 8378 km. Objects in low altitude orbits interact with the atmosphere

of the Earth. The International Space Station (ISS) has a nominal altitude of about 400 km and has to be lifted regularly to keep this altitude (see [HeavAb] for a plot of the height of the ISS during the past year). In lower altitudes, satellites would loose energy fast, re-enter too early and burn up eventually. Satellites in the LEO region perform at the end of their life time manoeuvres to decrease their altitude, re-enter the atmosphere and burn up after a while.

Objects with distances between approximately 7900 km and 8378 km are influenced by charged particles in the Van Allen radiation belt. These particles may cause computer failures and can shorten a satellite's mission dramatically. Consequently, only a small number of satellites are located in the Van Allen radiation belt.

The second protected region (Région B) is the region of the Geostationary Earth Orbits (GEO), also called geostationary ring, between 41 964 km and 42 364 km. Satellites in this region do not re-enter into the atmosphere, at the end of their life time they are put in so-called graveyard orbits 200 km above the geostationary ring. The range is narrow to establish geosynchronous orbits. With a semi-major axis larger or smaller an object will drift and will not be geostationary or geosynchronous any longer.

Between 8378 km and 41 964 km from the geocentre there is the Medium Earth Orbits (MEO) region, where mostly the satellites of the Global Navigation Satellite Systems (GNSS) are located. However, there is no unique definition of the MEO region, it is defined here as the complete region between the Van Allen radiation belt and the geostationary ring. Satellites in this region are also do not re-enter into the atmosphere and are put in higher or lower orbits at the end of their life time, to avoid interferences with other satellites.

Table 1.1 summarises the orbital regions with their individual range of semi-major axes.

Table 1.1: Orbital regions

	Range of semi-major axes (km)
LEO	6650 – 7900
Van Allen Belt	*7900 – 8378*
MEO	8378 – 41964
GEO	41964 – 42364

Nevertheless, in many cases the semi-major axis as the only selection criterion is not a good choice, as there are also objects, including space debris objects, which move through several regions. Other orbital elements, like the eccentricity or the inclination, have to be used for a finer subdivision.

1.1.1 Overview on Objects in geostationary and geosynchronous Orbits

Geostationary and geosynchronous satellites was proposed by Hermann Noordung (aka Herman Potočnik) in 1929 ([Noor 29]). Later, in 1945 the Science-Fiction-author Arthur C. Clarke proposed his idea of three geostationary satellites separated by 120° to get a worldwide coverage for communication (see [Clar 45]). Only 18 years later his idea was partially realised with the satellites Syncom 2 and Syncom 3. While Syncom 2 was intentionally a geosynchronous satellite, Syncom 3 was a geostationary satellite to telecast the Games of the XVIII Olympiad, 1964 in Tokyo, Japan.

Perfect geostationary objects perform one revolution around the Earth within one sidereal day, which is the time the Earth requires to rotate around its axis once. With Kepler's 3$^{\text{rd}}$ law of planetary motion one can calculate the semi-major axis a of an orbits of those objects (see e.g. [Basc 05]):

$$\frac{a^3}{T^2} = \frac{G}{4\pi^2} \left(M_\oplus + m \right),$$

(1.1)

where T is the revolution period and m the mass of an object orbiting around the Earth, $M_\oplus$ the mass of the Earth and G the gravitational constant. Because the mass of any artificial object in Earth's orbit is negligible with respect to the mass of the Earth, we may set $M_\oplus + m \approx M_\oplus$. Furthermore, the product of Earth's mass times gravitational constant is $GM_\oplus = (3.986\,004\,415 \pm 0.000\,000\,008) \times 10^{14}\,\mathrm{m^3\,s^{-2}}$ (taken from [Ries 92]) and the revolution period is one sidereal day, $T = 86\,164.099\,\mathrm{s} = 23\,\mathrm{h}\,56\,\mathrm{min}\,4.099\,\mathrm{s}$. The resulting the semi-major axis then becomes

$$a \approx 42\,164.17\,\mathrm{km}.$$

One revolution per sidereal day means $360°$ within $23\,\mathrm{h}\,56\,\mathrm{min}\,4.099\,\mathrm{s}$ or approximately $15.041°\,\mathrm{h^{-1}}$. An object with inclination $i = 0°$ seems staying above one fixed point of the Earth's equator. Inclinations different from $0°$ result in a "8"-shaped ground track, called analemma. If an object also has an eccentricity different from $\varepsilon = 0$ the Northern part of the analemma is bigger than the Southern part or vice versa. Therefore, these objects are called geosynchronous objects.

In Figure 1.2 one can see the different types of ground tracks related to geostationary and geosynchronous objects over 24 hours. The red dot represents the ground track of a geostationary object above Ecuador. The dimension of the dot is much larger than the actual ground track. The green curve represents the ground track of a geosynchronous object with an inclination of $20°$ but an eccentricity equal to zero. Finally, the blue curve is the ground track of a geosynchronous object with an inclination of about $8°$ and an eccentricity of 0.1.
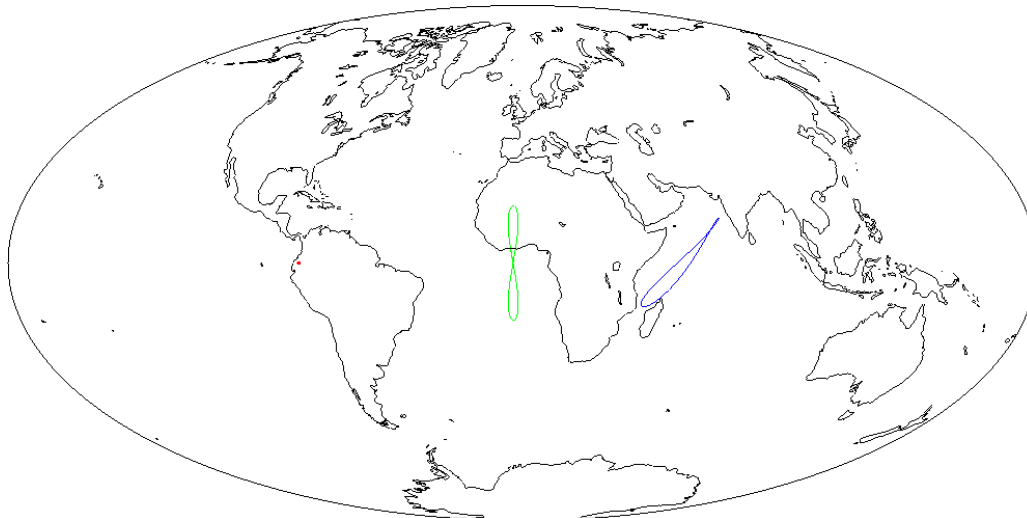
Figure 1.2: Types of ground tracks of typical GEO objects:
geostationary object (red dot) with $i = 0°$ and $\varepsilon = 0$
geosynchronous object (green curve) with $i \neq 0°$ and $\varepsilon = 0$
geosynchronous object (blue curve) with $i \neq 0°$ and $\varepsilon \neq 0$

Real objects in the GEO region are influenced by several types of gravitational perturbations: firstly, the gravitational potential of the Earth is not homogeneous resulting in forces which change the orbit. Secondly, the gravitational potentials of the Sun and the Moon also perturb the orbits.

Furthermore, when the semi-major axis is not exactly $42\,164.17\,\mathrm{km}$, objects drift in longitudinal direction.

Active satellites, which are controlled, perform station-keeping manoeuvres regularly to compensate for these effects and to stay in a predefined region around their original positions.

Space debris is by definition uncontrolled, so the perturbing effects are not compensated and an object will probably drift, not only in longitudinal but also in latitudinal direction. Figure 1.3 shows the distribution
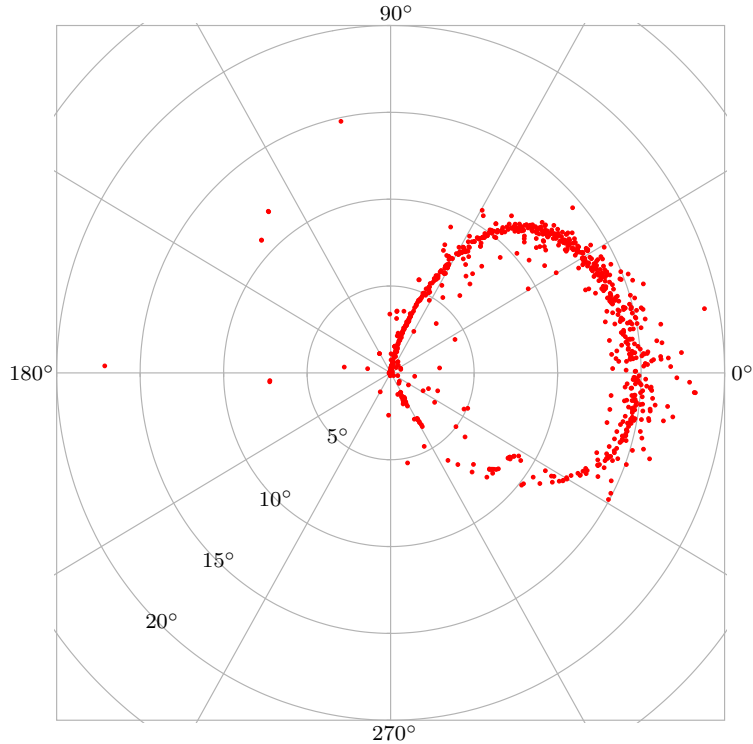
Figure 1.3: Distributions of the orbital planes of GEO objects in the USSTRATCOM catalogue (as of July 2011). The radial distance to the centre represents the inclination i and the azimuth the RAAN Ω.

of the orbital planes of GEO-objects in the USSTRATCOM catalogue. The polar plot of the inclination i (in radial direction) and the right ascension of the ascending node (RAAN) Ω, and represents the pointing direction of the normal vectors of the objects' orbital planes. The centre of the graph ($i = 0°$, $\Omega = 0°$) represents the rotation axis of the Earth and is mostly populated by controlled satellites. If a satellite is not controlled anymore, the normal vector will move away from ($i = 0°$, $\Omega = 0°$) and perform a precession motion with an period of about 54 years due to the perturbations of the Sun, Moon and the gravitational potential of the Earth.

In the internal AIUB object catalogue, a finer classification of objects is used which takes also the eccentricity ε of the orbit into account. For ZimSMART and its survey-only approach this classification has just statistical relevance, but for follow-up observations with other telescopes of certain objects discovered with ZimSMART the exact object type is important to schedule those observations.

Objects of the internal AIUB catalogue are subdivided into three categories:

- GEO (geosynchronous objects): Here, objects with a semi-major axis of more than $30\,000$ km and an eccentricity below 0.1 and an area-to-mass ratio (AMR) below $0.5\,\mathrm{m^2\,kg^{-1}}$ are merged. This class includes GEO and inclined geosynchronous objects (IGSO)

- eGEO (eccentric geosynchronous objects): Objects with a semi-major axis of more than $30\,000$ km, but with an eccentricity larger than 0.1 or an area-to-mass ratio of more than $0.5\,\mathrm{m^2\,kg^{-1}}$ fall in this class. It includes a small fraction of objects in highly-eccentric orbits (HEO).

- GTO (geostationary transfer objects): Objects in this class are not geosynchronous, but related to the launch of GEO objects (e. g. upper stages). Their initial apogee is in or near the geostationary

ring, but their perigee is in the LEO region. This leads to an interference with the atmosphere, the orbit will decay and objects will re-enter after a certain time.

Graveyard Orbits of the Geostationary Ring

At the end of their life time, satellites in the geostationary ring should be moved out of their orbits into so-called graveyard orbits. Therefore, manoeuvres are applied to raise the perigee by at least 235 km above the geostationary ring. The lift of 235 km consists of 200 km, which is dimension of the protected region, plus 35 km due to the lunisolar perturbations (taken from [IADC 02]). A more detailed computation takes the area-to-mass ratio (AMR) into account and leads to a lift ΔH of the perigee (see again [IADC 02]):

$$\Delta H = 235\,\text{km} + 1000\,\text{km} \cdot C \cdot \frac{A}{m}.$$

The factor C represents reflective properties of a satellite or space debris object. The term A/m stands for the AMR.

In a first order approximation, the AMR can be set to zero, which is valid for large satellites (e. g. GPS satellites with an AMR of $0.02\,\text{m}^2\,\text{kg}^{-1}$, [Beut 05]).

1.1.2 Overview on GNSS Objects

The Medium Earth Orbit region is populated by the satellites of the Global Navigation Satellite System (GNSS) and of the Molniya as well as of the Oko satellite system. In the scope of this thesis, only the orbits of GNSS satellites were investigated.

Currently, the GNSS consists of the full operating systems NAVSTAR GPS (USA) and GLONASS (RUS), and the systems in build-up Compass (CHN, currently consisting of 8 satellites) and Galileo (EU plus 9 non-EU countries[1] plus 8 countries in negotiation[2], currently consisting of four satellites as well as the test satellites GIOVE-A and -B). Table 1.2 shows some orbital characteristics, the semi-major axis a, the inclination i, the revolution period T and the number of orbital planes each system consists of. They perform approximately two revolutions per day around the Earth. The ascending nodes of the orbital planes are distributed around the Earth: in the NAVSTAR GPS system they are separated by 60°, in the GLONASS, Galileo and Compass systems it is or will be, respectively, a separation of 120°. The eccentricities of all orbits are approximately zero.

Table 1.2: Characteristics of GNSS orbits

Satellite system	Orbital characteristics			number of
	a (km)	i (°)	T (hh:mm)	orbital planes
NAVSTAR GPS	26600	55	11:58	6
GLONASS	25500	65	11:15	3
Galileo	29600	56	14:05	3
Compass	27900	55	12:53	3

In the GLONASS system, eight active satellites share one orbital plane, separated by 45° in their orbit, in the NAVSTAR GPS system there are six satellites separated by 60°. So, normal vectors of satellites of the GNSS are grouped in clouds, separated by the values given above (see Fig. 1.4). Only visible are the clouds of the completed systems NAVSTAR GPS and GLONASS, the Galileo and Compass systems are represented by a few satellites and do not form clouds in this diagram. In ideal case one would expect point like structures because many satellites share one orbital plane, but in reality the distribution is broadened.

[1] PR China, India, Israel, Morocco, Norway, Saudi Arabia, Switzerland, South Korea, Ukraine
[2] Argentina, Australia, Brazil, Canada, Chile, Malaysia, Mexico, Russian Federation
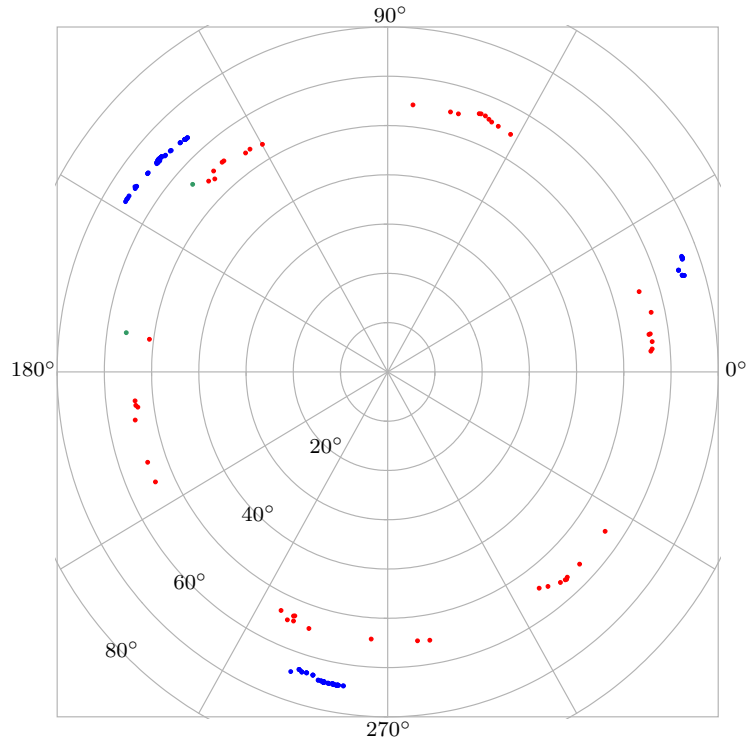
Figure 1.4: Distribution of orbital planes of object in the GNSS. The radial distance to the centre represents the inclination i and the azimuth the RAAN Ω (as of July 2011).
red dots: NAVSTAR GPS, blue dots: GLONASS,
green dots: Galileo (represented by GIOVE-A and -B)

The ground tracks are more diverse than in the geostationary ring. In Fig. 1.5 one can see one ground track for each GNSS system. The were not taken from present satellites, but the orbital parameters are chosen to simulate an object in the GPS regime (red line), GLONASS regime (blue) and (Galileo regime (green), respectively. Each ground track is plotted for a time span of 24 hours. The track of the GPS satellite is nearly closed, those of the other satellites need several periods to form a closed track.

All objects, operating or not, underlie the same ageing effects like objects in the geostationary ring. So after a while, one expects the same kind of events to happen: collisions, explosions, fragmentation and ageing by thermal expansion. Thus, one might expect similar object types. Hence, a finer subdivision of object types is similar to that of the geostationary ring:

- MEO (roughly spoken Medium Earth orbiters): Objects with a semi-major axis below $30\,000\,\text{km}$ and an eccentricity below 0.1 and an area-to-mass ratio (AMR) below $0.5\,\text{m}^2\,\text{kg}^{-1}$.

- eMEO (eccentric Medium Earth orbiters): Objects with an semi-major axis below $30\,000\,\text{km}$, but with an eccentricity larger than 0.1 or an area-to-mass ratio of more than $0.5\,\text{m}^2\,\text{kg}^{-1}$ fall in this class. Like the eGEO objects the eMEO objects represent a small fraction of the highly-eccentric orbits (HEO) objects.
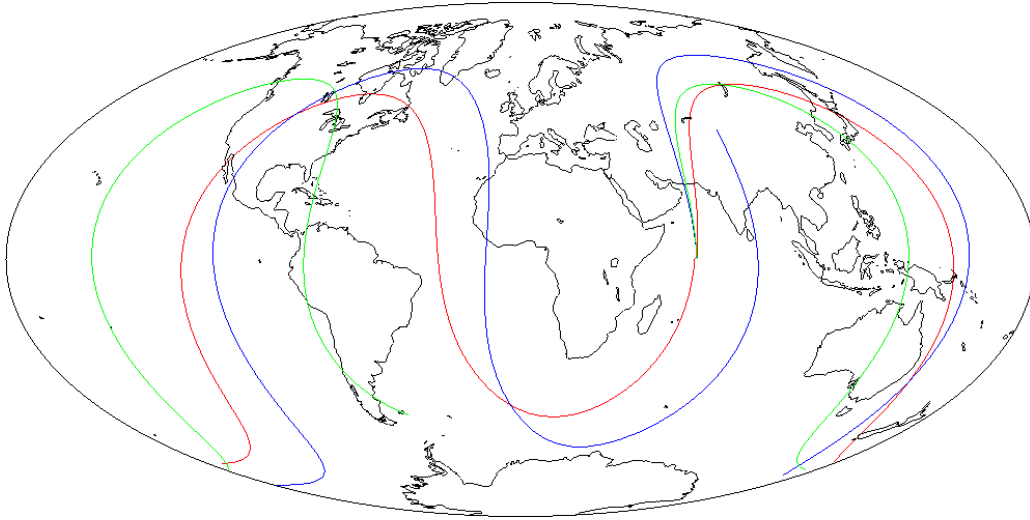
Figure 1.5: Examples of ground tracks: NAVSTAR GPS regime (red), GLONASS regime (blue) and Galileo regime (green).

1.2 The Telescope ZimSMART

ZimSMART, an acronym for Zimmerwald Small Aperture Robotic Telescope, is located at the Zimmerwald Observatory, 10 km South of Bern, Switzerland. The purpose is to perform survey observations during the night.

Throughout the period of the dissertation, ZimSMART was kept in a experimental state to test new hardware and software components. The mount was exchanged in 2009, while the optical tube assembly was changed twice: first in 2009, together with the mount, and in 2010. The same camera was used during the entire period. Figure 1.6 shows the time line of the used components, divided into mount, optical tube assembly and camera. The components are presented in detail in the following paragraphs.

Figure 1.6: Time line of the hardware components of ZimSMART

The Fig. 1.7(a) to 1.7(c) show the three different set-ups of ZimSMART, presented in Fig. 1.6. The camera is visible in the left image, on top of the tube. In the image of the second set-up, the camera is on the opposite side of the telescope and therefore not visible. Due to the changed position, the tube is visible from the front in the right image.

1.2.1 Mounts

ZimSMART was first built with the mount ME MKS 4000, developed by Paramount, in 2006 and was still used in the same configuration in June 2008, when the acquisition of the observations for the data set of this dissertation started. The mount was replaced in September 2009 by the mount DDM85, developed by Astrosysteme Austria (ASA).

(a) First set-up   (b) Second set-up   (c) Third set-up

Figure 1.7: Set-ups of the telescope ZimSMART

Paramount ME MKS 4000

The specifications of the Paramount are given in [Paramount]. The pointing accuracy is specified to be between $10''$ and $30''$. The tracking accuracy without periodic error correction is about $7''$ and with that correction below $1''$. The maximum tracking velocity in right ascension is about $3.5°\,s^{-1}$ and in declination about $5°\,s^{-1}$.

ASA DDM85

The second mount was developed by ASA, the specifications are given in [ASAb]. The pointing accuracy is given to be below $12''$ RMS when a pointing file is available. A pointing file contains epochs and positions, of which observations shall be taken. Another possibility is to set positions manually, but for this case no values for the accuracy are provided.

Measurements by ASA led to a tracking accuracy below $0.35''$ RMS within $5\,min$ of tracking. The maximum tracking velocity is about $13°\,s^{-1}$.

1.2.2 Optical Tube Assemblies

The size of the area on the sky, which can be observed at once, i.e. which can be imaged in the focal plane, is defined by the parameters of the optical system.

First, a optical tube assembly of Takahashi was used. In September 2009, it was replaced by one of Astrosysteme Austria, which was used till March 2010. Thereafter, the first one was used again.

Takahashi ε-180ED

The optical tube assembly Takahashi ε-180ED, presented in [Takahashi], has a Newton optical design with a hyperbolic primary mirror and an effective aperture of $180\,mm$. The diameter of the primary mirror is $190\,mm$ and $80\,mm$ of the secondary mirror. With a focal length of $500\,mm$, the focal ratio becomes F/2.8.

The resulting field of view is $4.1° \times 4.1°$.

ASA 12N-OK3 f 3.6

This optical tube assembly also has a Newton optical design, but the primary mirror is parabolic with a diameter of $300\,mm$. The secondary mirror has a diameter of $120\,mm$. The focal length of the system is $1080\,mm$, which results in a focal ratio of F/3.6 (see [ASAa]).

The field of view becomes $2° \times 2°$.
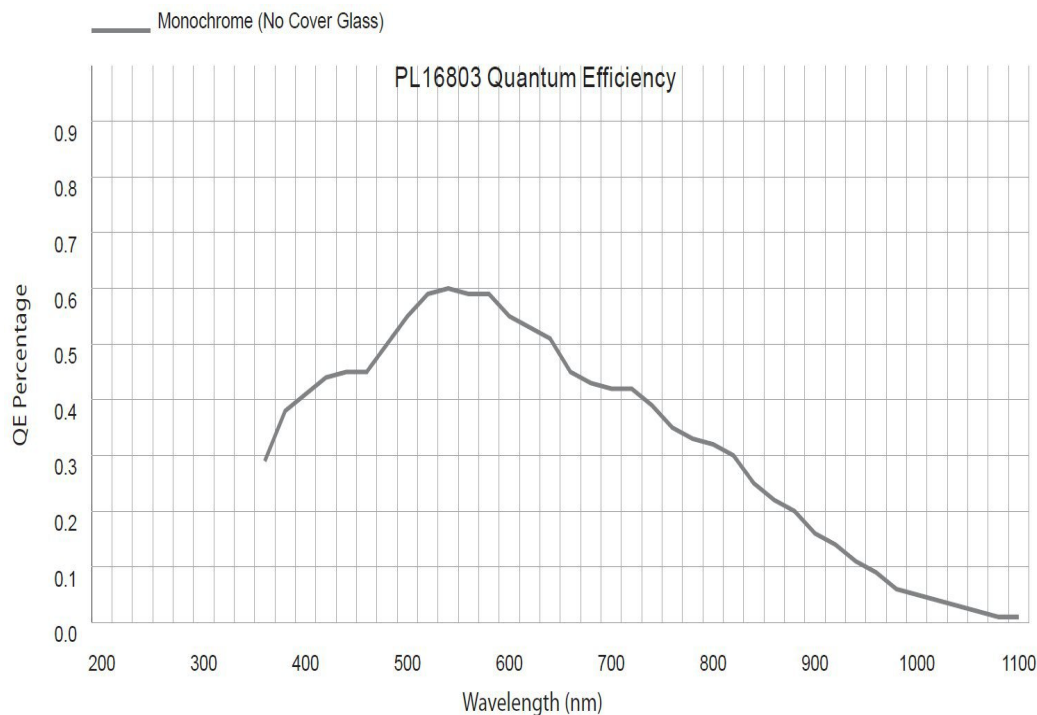
Figure 1.8: Quantum efficiency of the camera PL16803 (taken from [FLI])

1.2.3   Camera FLI ProLine PL16803

The same camera was used during the entire period of observations for this dissertation. The Pro-Line PL16803 was developed by Finger Lakes Instruments (FLI). The manufacturer of the sensor is Ko-dak, the CCD chip is the KAF-16803. The specifications are given in [FLI]. The dimension is 4096×4096 pixels with a pixel size of $9\,\mu m \times 9\,\mu m$.

The read-out speed is one factor, besides the velocity of the mount, which defines how many images can be taken within one night. High values of the read-out speed allow the acquisition of a larger number of images, but unfortunately the read-out noise also increases. The maximum read-out speed is $8\,MHz$. The read-out noise does not increase very much: from typical 10 electrons at $1\,MHz$ to 13 electrons at $8\,MHz$. The observations were taken with a read-out speed of $1\,MHz$.

Figure 1.8 shows the quantum efficiency as specified by FLI (see again [FLI]). The measurements were performed without optical filter systems.

1.2.4   Analysis of the Performance of the third Set-up of ZimSMART

From a set of 236 images in the routine observation of GEO surveys, measured values of the slew times of the telescope and the exposure an read-out times of the camera, respectively, were analysed. The images were obtained with the third set-up of ZimSMART as it was used for the longest time.

For this experiment, the exposure time was set to $10\,s$. From the header of the images, an average value of the true exposure time of $10.0647\,s \pm 0.0003\,s$ could be determined. The relative deviation to the defined value is approximately $0.65\,\%$.

The average read-out time of an image is about $7.12\,s \pm 0.02\,s$, which leads to a minimum cycle time between two images of a series of about $17.18\,s \pm 0.02\,s$. After completing a series of images, the telescope

Table 1.3: Slewing times of ZimSMART in its third set-up, colour-coded numbers related to Fig. 1.9

	Name	Average slewing time (s)
I	inter-field slew	7.7 ± 0.2
II	intra-stripe slew	21.3 ± 0.9
III	intra-pair slew	21.0 ± 0.7
IV	inter-pair slew	26.1 ± 0.7

has to be moved, either to new coordinates or to observe the same coordinates again.

Figure 1.9 shows the different slews the telescope control software allows to perform. This presentation is not related to any applied survey scenario, but gives options for the motion of the telescope in principle. The scenarios are presented in detail in Section 2.2.

The blue arrows represent slews within one pair. The arrow I is the motion between two fields, the so-called inter-field slew. In case of ZimSMART in its third set-up, this motion is $+4°$ in declination. Arrow II, the intra-stripe slew, is the motion of $-16°$ in declination at the end of the observation of a stripe back again to the beginning. When a pair of stripes is observed, at the end of one stripe the telescope moves to the second one (arrow III), the intra-pair slew. This motion is again $-16°$ in declination and also $\pm15°$ in right ascension.

If two pair of stripes are observed, there are also motions from one pair to the other, the so-called inter-pair slews (arrow IV). Depending on the separation D between both pairs, the time for the motions differ from the other ones mentioned above. Therefore the motion in right ascension is variable, but in declination it is $-16°$. Although the four possibilities lead to different inter-pair slewing times, the analysis did not take this into consideration, and only one slewing time is determined.

For the inter-field slew, an average of $7.7\,\text{s} \pm 0.2\,\text{s}$ was calculated. This means that the slewing time is only $0.6\,\text{s}$ larger than the read-out time. When changing the fields within on stripe, not much observation time is lost, because new observations cannot start when the telescope is not at its final position or the last image is not read out completely, respectively.

The intra-stripe slewing time was determined to be $21.3\,\text{s} \pm 0.9\,\text{s}$, while the intra-pair slewing time was $21.0\,\text{s} \pm 0.7\,\text{s}$. Both slewing times are equal within the uncertainties, the differences are due to the limited data set in the analysis.

When more than one pair of stripes are observed, the inter-pair slewing time plays also a role, shown in red in Fig. 1.9. It was calculated to be $26.1\,\text{s} \pm 0.7\,\text{s}$, which is about $5\,\text{s}$ larger than the slewing times within one pair of stripes. It has to be said again, that this is an average of the four possibilities, displayed in Fig. 1.9. The calculated values are summarised in Tab. 1.3.

1.2.5 Observations and Data Format

Observations are performed automatically, the observations are acquired according to an observation plan given to the telescope software. The observation plan consists of frames to observe, at least. Additionally, priorities and exposure times can be given, otherwise default values are taken. Within a night, several kinds of observations are performed: GEO and MEO survey observations as well as observations of GNSS satellites for calibration measurements.

With ZimSMART survey observations are performed in the GEO and MEO regions. The tracking methods, described below, differ between both orbital regions. In general, one has three possibilities for tracking modes during the exposures:
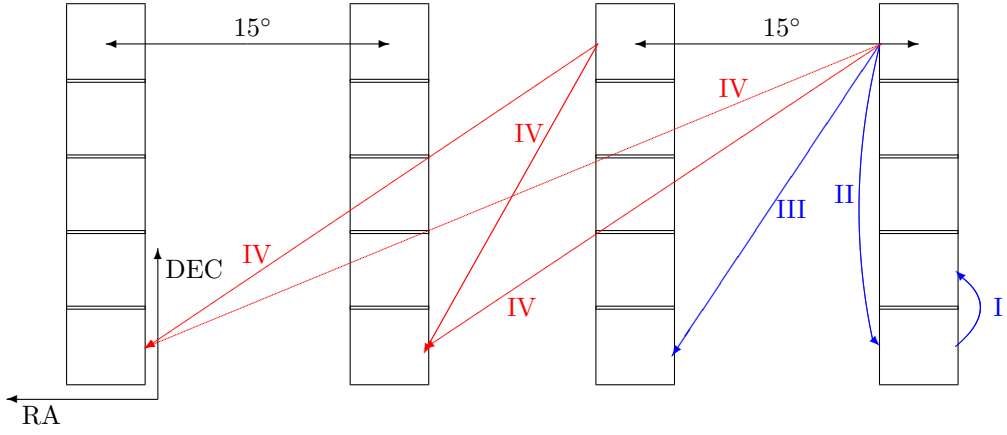
Figure 1.9: Slewing times of ZimSMART, exemplified by the GEO survey scenario (scheme)

1. sidereal tracking, where the telescope moves with the angular velocity of the celestial background, so stars appear point-shaped on the frames and all moving objects are elongated,

2. blind tracking, where the telescope moves with the assumed angular velocity of an object, so these objects appear point-shaped, objects with differing angular velocities and stars are elongated,

3. ephemeris tracking, where the telescope moves with the calculated angular velocities of an object based on ephemerides.

The information of the observed objects contained in the images are extracted to files. A set of consecutive epochs and measured positions is called a tracklet and for each observed object an individual tracklet is created, even if they were detected on the same image. In the observation process of ZimSMART, five images belong to a series and a maximum number of five observations belong to one tracklet, consequently.

With the exposure time and read-out time mentioned above, the length of a tracklet can be determined. It consists of five times the exposure time and four times the read-out time. The read-out time after the last exposure has no effect on the tracklet length, but defines only the temporal gap to the beginning of the next series:

$$
\begin{aligned}
t_{\mathrm{tracklet}} &= 4 \cdot \text{exposure time} + 4 \cdot \text{read-out time} \\
&= 4 \cdot 10\,\mathrm{s} + 4 \cdot 7.12\,\mathrm{s} \\
&= 68.48\,\mathrm{s}
\end{aligned}
$$

The exposure time of $10\,\mathrm{s}$ were mainly used for the prior analysis, the majority of observations were taken with an exposure time of $7\,\mathrm{s}$, the length of a tracklet is shorter, consequently: $t_{\mathrm{tracklet}} = 56.48\,\mathrm{s}$.

Either way, a tracklet has a length of about one minute, which is approximately $0.07\,\%$ of the orbital period of a geostationary object. With one tracklet, an orbit cannot be determined, the results would be ambiguous. With a second tracklet, and ideally a third one, in the same night, a non-ambiguous orbit determination is possible.

1.2.6 Limiting Magnitude of ZimSMART and observable Object Sizes

Analysing a large observation period of GEO surveys, one can estimate the limiting magnitude of the telescope for moving objects. For each observation a magnitude of the observed object was estimated. In Fig. 1.10, the distribution of the magnitudes is shown.
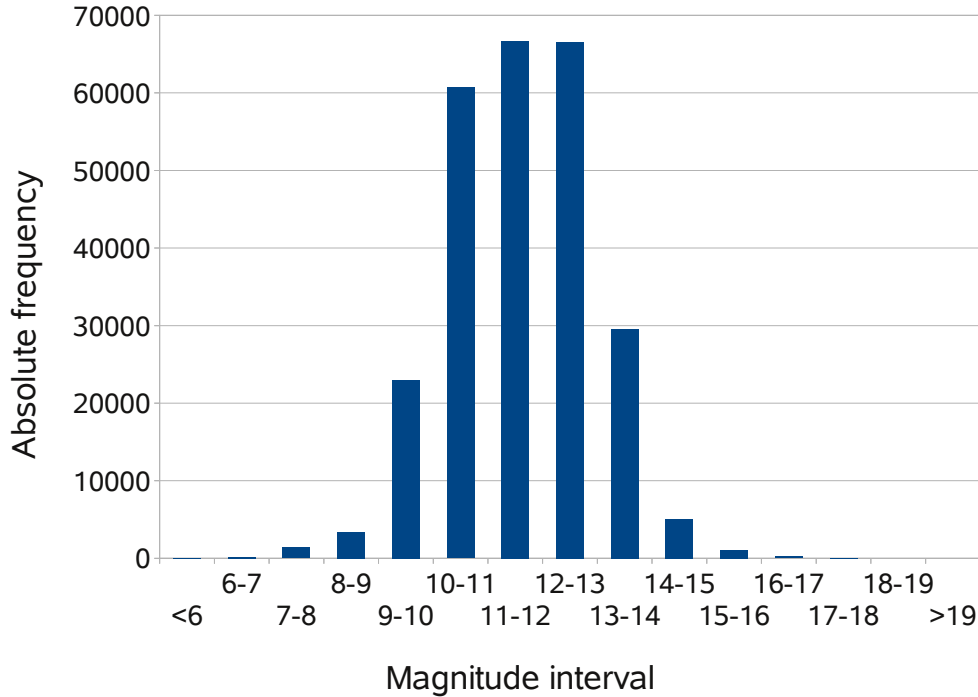
Figure 1.10: Magnitude distribution of the GEO surveys between April 2010 and December 2011

The limiting magnitude can be estimated using two different definitions. For both cases, an equal distribution of observable magnitudes must be assumed. Then, on the one hand the magnitude of the faintest object observed sets the limit of the possibilities of the telescope. On the other hand, where the distribution is at the half of the maximum, one can set a practical limit, because at higher magnitudes only less than half the objects might be detected.

The period used for the estimation is between April 2010 and December 2011, the period of ZimSMART in its third set-up. No major hardware changes were done and the system was running stable. The maximum magnitude observed was 17.85, but only a very small number of observations (24 in this period) were fainter than 17th magnitude. Regarding the practical limit mentioned above, where the detected magnitudes drop below 50 %, it lies at approximately 13th magnitude. This value confirms the given value of the manufacturer of the tube assembly (see [Takahashi]), who gives a visual limiting magnitude of 13.0 mag.

1.2.7 Observable Object Sizes

When the magnitude of an object is measured for a certain epoch, the corresponding size of that object can be estimated under certain assumptions, like shape, albedo and topocentric distance. While topocentric distances can be determined from the orbit, shape and albedo of an object remain unknown. In [Schi 03], we find a relationship between the measured magnitude and the estimated size of the object:

$$m_{\text{object}} = m_{\odot} - 2.5 \log \left(\frac{d^2}{4R^2} \alpha \cdot \rho_{\text{Bond}} \cdot p(\theta) \right), \tag{1.2}$$

where m_{object} is the apparent magnitude, d is the size of the object and R is the topocentric distance. The factor ρ_{Bond} represents the Bond albedo, which is the fraction of the total incident radiation reflected

Table 1.4: Estimated object size observable by ZimSMART, depending on apparent magnitude and orbital region. Topocentric distances: GEO about $38\,000\,\mathrm{km}$, MEO about $19\,500\,\mathrm{km}$

Magnitude (mag)	GEO region (m)	MEO region (m)
7	51.6	26.5
8	32.6	16.7
9	20.6	10.6
10	13.0	6.7
11	8.2	4.2
12	5.2	2.7
13	3.3	1.7
14	2.1	1.1
15	1.3	0.7
16	0.8	0.4

by the object. Mulrooney et al. concluded to use a value of 0.175 for the Bond albedo (see [Mulr 08]). The function $p(\theta)$ is the phase function, with the phase angle θ given in radians:

$$p(\theta) = \frac{1}{\pi}\Big(\sin(\theta) + (\pi - \theta) \cdot \cos(\theta)\Big)$$

The phase angle θ is the angle between the line from the object to the observer and that from the object to the Sun. The factor α represents the assumed structure of the object. For a Lambert sphere, α becomes 2/3, for a randomly tumbling plate it is 1/3. The complete derivation of Eq. (1.2) can be found in [Schi 03].

Besides a Bond albedo of 0.175, I assumed a tumbling plate at a phase angle of $\theta = 0°$. Objects in the geostationary ring have topocentric distances from the Zimmerwald Observatory between $38\,000\,\mathrm{km}$ and $42\,600\,\mathrm{km}$, while many objects in the MEO region have topocentric distances between $19\,500\,\mathrm{km}$ and $23\,300\,\mathrm{km}$. For the estimation I assumed a topocentric distance of $38\,000\,\mathrm{km}$ and $19\,500\,\mathrm{km}$, respectively, for an lower limit of possible object sizes. The results are presented in Tab. 1.4

1.3 Uncertainties of Orbits

1.3.1 Measurement Techniques

To observe objects revolving around the Earth, there are several methods to observe the different orbital regions. Not every method can be applied to every orbital region. Some techniques may be successful only for objects in low altitudes, because as two way measurements e. g. laser beams, radio or microwaves are damped on both ways. Some are only successful for high altitudes because the temporal resolution of the detector is not high enough and others detect light from the Sun which is reflected by objects.

1.3.1.1 Optical Observations

The observations with optical telescopes are a method to determine orbits. They are performed with CCD and CMOS sensors. These are read out and create an object image. Satellites do not shine by themselves, they only reflect light from the Sun. To achieve optimal conditions a satellite must not be in the shadow of the Earth, close to the Moon or at a small phase angle (the angle between the line

Earth-Sun and Earth-satellite). At small phase angles only little light is reflected in the direction of the telescope and in the shadow of the Earth the satellite is unlit. This method is only performable in the night but in principle every orbital region can be observed. For objects of the LEO region the accuracy of the positions of the reference stars as well as of the time measurement must be very high or an orbit determination will lead to results with high uncertainties. Also, the actual distance between the observer and the satellite cannot be measured.

The position of the satellite is then determined from the positions of reference stars on each image. With observations spread over a whole night it is possible to calculate a first orbit and with more observations in subsequent nights (called follow-up observations) the orbit becomes more accurate. This allows redetections of the object in further subsequent nights.

1.3.1.2 Satellite Laser Ranging (SLR)

The Satellite Laser Ranging is a method to measure directly the distance of a satellite from an observer. A laser beam is sent from a telescope and reflected by the satellite. The satellite has to be equipped with retroreflectors to reflect as much light as possible in the same direction. The reflected light is then detected by the same telescope again or another one nearby. This is called two-way measurements. The time span between sending the beam and receiving it is measured and, multiplied by the speed of light and divided by 2, gives the actual distance. With the apparent position on the sky and multiple observations one can determine an orbit of the satellite.

Because the laser beam is damped on the way to the satellite and back, in practice only satellites of the MEO and LEO are tracked. With one-way measurements one can go further but then the satellite needs an receiver to detect the laser beam itself and not reflect it. With this method the Lunar Reconnaissance Orbiter (LRO) in an orbit around the Moon is tracked.

1.3.1.3 RADAR Measurements

Radio Detection and Ranging (RADAR) uses electromagnetic waves which are reflected by a satellite and received by the ground station again. With this method position and distance of the satellite can be measured.

RADAR measurements can only be used for the LEO region, because the RADAR pulse is damped on the way to and back from the satellite.

1.3.1.4 Position Measurements with the Global Navigation Satellite System (GNSS)

The acronym GNSS stands for Global Navigation Satellite System and consists of he following individual subsystems: the completed systems GPS (USA) and GLONASS (RUS) as well as the systems in assembling Galileo (several countries in Europe) and Compass (CHN).

The position measurement with GNSS satellites requires a receiver at the satellite itself. Then the method is equivalent to navigation systems built in car, ship, aeroplanes and so on. With four GNSS satellites the position (e.g. longitude, latitude and altitude) and the time is measured. The more satellites are used the more accurate the results get.

The satellite must be in a lower orbit than the GNSS satellites, so the method is only applicable to the LEO and a fraction of the MEO region.

1.3.1.5 Microwave Position Measurements

The Doppler Orbitography and Radiopositioning Integrated by Satellite (DORIS) is a system for precise orbit determinations with the Doppler effect. It is a one way measurement technique where a ground

Table 1.5: Parallaxes depending on orbital range

Orbital range	Range of parallaxes
LEO	$54° - 74°$
MEO	$12° - 15°$
GEO	$\approx 9°$

station sends a signal with two frequencies two an orbiting satellite. The satellite receives the signals with different frequencies and from the differences the velocity of the satellite with respect to the rotation of the Earth and finally the true velocity can be calculated.

This method is only be applied to objects of the LEO region.

1.3.1.6   Two Line Element Set Analysis

Not an observation technique but a validation method is the analysis of Two Line Element sets (TLE). The TLEs are a possibility to display orbital parameters of objects orbiting around the Earth. Not only the orbital elements are included but also resistance parameters of the applied model. For satellites in the MEO and GEO region these resistance parameters can be neglected, but for the LEO region they play a significant role.

To estimate the accuracy of the TLEs they are validated with other measurements like optical or RADAR. This is only possible if the reference measurements are more accurate than the TLEs which is true for SLR, RADAR and optical observations.

For maintaining a catalogue of objects it is possible to correlate new observations via TLE. Therefore the TLEs can be propagated to present date. The orbital uncertainties then also are propagated and become larger.

1.3.1.7   Operator Data

The owner and operator of an satellite has to know exactly where the satellite is located, so the orbital uncertainties are very small. Therefore, the other methods can be validated by operator data, but it is again not a observation technique. Unfortunately, these data sets are mostly just available when the operators perform analyses by themselves.

1.3.2   Worst Case Scenarios

From the observer, a satellite is seen under an angle, the angle between the line of sight and the radius vector r of the satellite, called the parallax p (see also Fig. 1.11). It causes a displacement of the direction of the radial, along-track and cross-track uncertainty (σ_r, σ_a, σ_c, respectively).

In case of a rising or setting satellite the sine of the parallax p can be determined by the Radius of the Earth $R_{\oplus}$ divided through the radius vector r:

$$\sin(p) = \frac{6378\,\mathrm{km}}{r}$$

Also in the figure, there are shown the radial, along-track and cross-track uncertainties. Possible parallax ranges for the orbital regions are shown in Table 1.5.
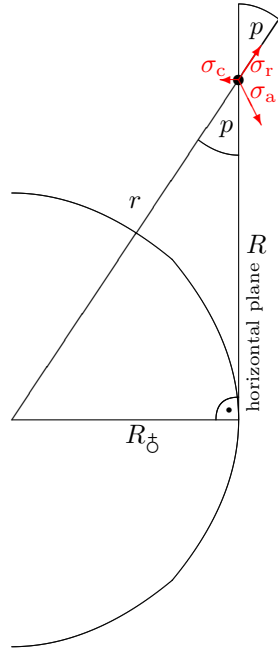
Figure 1.11: Orientation of the orbital uncertainties (sketch)

(a) Satellite rises perpendicular to the horizon

(b) Satellite crawls at the horizon
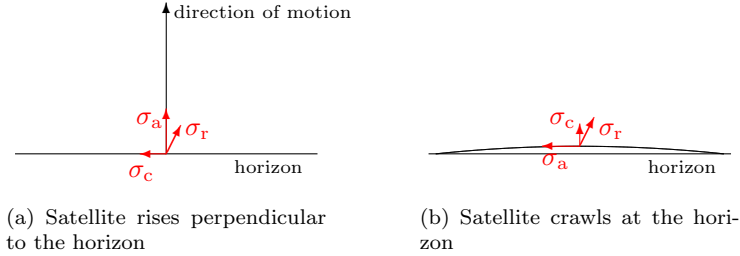
Figure 1.12: Situation of a rising or setting satellite at the horizon

Then, there are two worst cases to focus on: a satellite which rises (or sets) perpendicular to the horizon and one which crawls at the horizon, shown in Figure 1.12. Every other case of possible risings or settings will lie between these worst cases.

a) In the first case the projections of the uncertainties on a tangential plane at the celestial sphere are: $\sigma_{\mathrm{a}} \cdot \cos(p)$ contributing to the uncertainty in elevation and $\sigma_{\mathrm{c}} \cdot \cos(p)$ and $\sigma_{\mathrm{r}} \cdot \sin(p)$ contributing to the uncertainty in azimuth. The uncertainty in azimuth and elevation is then the maximum of the corresponding pair. The uncertainty in radial direction leads to an uncertainty in rising time. Then, the telescope has to move along the horizon, because the Earth is rotating under the orbital plane, until the satellite has risen.

b) The second case of a satellite close to the horizon the projection of the uncertainties on the celestial sphere are similar: σ_{a} contributing to the uncertainty in azimuth and $\sigma_{\mathrm{c}} \cdot \cos(p)$ and $\sigma_{\mathrm{r}} \cdot \sin(p)$ contributing to the uncertainty in elevation.

In the sense of worst scenarios, the choice is then between each of the possibilities, which is the larger

one.

$$\widetilde{\sigma}_{\mathrm{AZ}} = \begin{cases} \sigma_{\mathrm{c}} \cdot \cos(p) & \text{case a)} \\ \sigma_{\mathrm{r}} \cdot \sin(p) & \text{case a)} \\ \sigma_{\mathrm{a}} & \text{case b)} \end{cases}$$

$$\widetilde{\sigma}_{\mathrm{EL}} = \begin{cases} \sigma_{\mathrm{a}} \cdot \cos(p) & \text{case a)} \\ \sigma_{\mathrm{c}} \cdot \cos(p) & \text{case b)} \\ \sigma_{\mathrm{r}} \cdot \sin(p) & \text{case b)} \end{cases}$$

The uncertainties in azimuth and elevation have to be converted using the topocentric distance of the satellite to write them in degree, arcminutes or arcseconds. Referring to Figure 1.11, one can see that for a rising as well as setting satellite the problem is reduced to a right-angled triangle,

$$R = \sqrt{r^2 - R_{\oplus}^2}.$$

Again, in the sense of worst case scenarios we take the minimum radius vector possible of each orbital region to calculate the minimum topocentric distance. As to see from the formulas above this represents a maximum uncertainty in azimuth and elevation.

$r =$ 6650 km	for LEO	$\rightarrow$	$R =$ 1880 km
$r = 25\,500$ km	for MEO	$\rightarrow$	$R = 24\,700$ km
$r = 42\,000$ km	for GEO	$\rightarrow$	$R = 41\,600$ km

With the topocentric distance the uncertainties can be converted in radian measure.

$$\sigma_{\mathrm{AZ}} = \arctan\left(\frac{\widetilde{\sigma}_{\mathrm{AZ}}}{R}\right)$$

$$\sigma_{\mathrm{EL}} = \arctan\left(\frac{\widetilde{\sigma}_{\mathrm{EL}}}{R}\right)$$

The σ_{AZ} and σ_{EL} represents the uncertainty in azimuth and elevation, and defines the necessary field of view of a telescope or the search area where a telescope with a smaller field of view has to observe.

1.3.3 Orbit Accuracies

To observe a satellite in subsequent nights a sufficient orbit determination is required. Different measurement techniques will lead to different orbit uncertainties.

1.3.3.1 Two Line Element Catalogue Analysis

The TLE catalogue analysis by T. Flohrer et al. (see [Floh 09]) of LEO objects validated by RADAR measurements led to uncertainties in along-track direction of $\sigma_{\mathrm{a}} < 1.3$ km, $\sigma_{\mathrm{c}} < 0.6$ km in cross-track direction and $\sigma_{\mathrm{r}} < 0.5$ km in radial direction. Wang et al. (see [Wang 09]) propagated TLEs for objects with semi-major axes greater than 7100 km and they got for an interval of 1 d uncertainties of < 2.4 km in all directions. For objects which are about to re-enter the atmosphere of the Earth, the orbital uncertainties can raise to < 27 km in all directions.

A similar analysis for the GEO region where the TLEs were validated by optical observations (see again [Floh 09]) led to uncertainties in along-track direction of $\sigma_a < 1.3\,\mathrm{km}$, in cross-track direction radial direction of $\sigma_a < 23.0\,\mathrm{km}$, $\sigma_c < 1.7\,\mathrm{km}$ in cross-track direction and $\sigma_r < 11.4\,\mathrm{km}$ in radial direction.

The Japan Aerospace Exploration Agency (JAXA) claim in an analysis ([Hiro 10]) that their accuracy of the orbit of ALOS (LEO, $i = 98.2°$) is better than 30 cm. So, they validated TLE data sets and came to the result of uncertainties of 0.7 km in RMS during the analysis period and 0.2 km at epochs of the TLEs (no propagation). An uncertainty in RMS can be interpreted as an uncertainty in all directions, again with respect to the worst case scenario method.

1.3.3.2 GNSS Data

Analysing position measurements of satellites in the LEO region with GNSS data, C. Flohrer et al. (see [Floh 11]) concluded that the orbital uncertainties are about $6.0\,\mathrm{mm} \pm 0.4\,\mathrm{mm}$ in all directions.

1.3.3.3 Satellite Laser Ranging

The analysis of LEO region C. Flohrer et al. (see [Floh 11]) resulted in uncertainties of $22.7\,\mathrm{mm} \pm 7.2\,\mathrm{mm}$ in all directions.

In the MEO region an SLR only analysis led to uncertainties of about 20 cm (see [IGS ACC]) in all directions. Combined with GNSS measurements (from [Thal 11]) these uncertainties could be reduced to 1.5 mm, again in all directions.

1.3.3.4 Microwave Measurements

With analysing data of DORIS, C. Flohrer et al. (see [Floh 11]) concluded orbit uncertainties of satellites in the LEO region to be $3.9\,\mathrm{mm} \pm 0.1\,\mathrm{mm}$ in all directions.

1.3.4 Pointing Accuracies

The dtermination of the pointing accuracies were performed with the formulas given above by applying the worst case scenarios. The results are presented in tabular form, divided by the orbital regions. Each table consists of the measurement technique, the along-track, cross-track and radial uncertainty, the corresponding reference and the pointing accuracy in azimuth and elevation.

1.3.4.1 LEO

Measurement technique	along-track σ_a	cross-track σ_c	radial σ_r	Reference	azimuth σ_{AZ}	elevation σ_{EL}
TLE (RADAR validated)	$< 1.3\,\mathrm{km}$	$< 0.6\,\mathrm{km}$	$< 0.5\,\mathrm{km}$	[Floh 09]	$< 2.4'$	$< 53.4''$
TLE (operator data val.)		$0.7\,\mathrm{km}$		[Hiro 10]	$1.3'$	$1.0'$
TLE (1 d propagated)	$< 2.4\,\mathrm{km}$ in all directions $< 27\,\mathrm{km}$ in all directions			[Wang 09]	$< 4.4'$ $< 49.4'$	$< 4.3'$ $< 48.1'$
GNSS	$6.0\,\mathrm{mm} \pm 0.4\,\mathrm{mm}$ in all directions			[Floh 11]	$6.6 \times 10^{-4}{''}$	$6.4 \times 10^{-4}{''}$
DORIS	$3.9\,\mathrm{mm} \pm 0.1\,\mathrm{mm}$ in all directions			[Floh 11]	$4.3 \times 10^{-4}{''}$	$4.2 \times 10^{-4}{''}$
SLR	$22.7\,\mathrm{mm} \pm 7.2\,\mathrm{mm}$ in all directions			[Floh 11]	$2.5 \times 10^{-3}{''}$	$2.5 \times 10^{-3}{''}$

1.3.4.2 MEO

Measurement technique	along-track σ_a	cross-track σ_c	radial σ_r	Reference	azimuth σ_AZ	elevation σ_EL
SLR only	20 cm in all directions			[IGS ACC]	$1.7 \times 10^{-3\prime\prime}$	$1.6 \times 10^{-3\prime\prime}$
SLR & GNSS	1.5 mm in all directions			[Thal 11]	$1.3 \times 10^{-5\prime\prime}$	$1.2 \times 10^{-5\prime\prime}$

1.3.4.3 GEO

Measurement technique	along-track σ_a	cross-track σ_c	radial σ_r	Reference	azimuth σ_AZ	elevation σ_EL
TLE (optical validated)	< 23.0 km	< 1.7 km	< 11.4 km	[Floh 09]	$< 1.9'$	$< 1.9'$

1.4 Outline

In the scope of the dissertation, there is the built-up and maintenance of a catalogue of objects. The observations of these objects could not be associated to any object of already existing catalogues, like the USSTRATCOM catalogue of unclassified objects.

In Chapter 2, different survey scenarios are discussed and concluded, which is an efficient scenario for ZimSMART to achieve a catalogue as complete as possible down to the limiting magnitude of ZimSMART. First, survey scenarios for the geostationary ring are presented, and second, one for the MEO region.

The object identification process and catalogue built-up is presented in Chapter 3. There, the correlation methods are explained, as well as the development states the processing pipeline was going through, to demonstrate an increasing efficiency.

In a catalogue of objects, there might be active satellites, too, which perform manoeuvres once in a while. Without a manoeuvre detection routine, new observations might not be associated to these satellites. Chapter 4 presents a manoeuvre detection method and the results, which could be obtained by analysing known manoeuvres.

The orbit determination process also includes the possibility to estimate the area-to-mass ratio (AMR) of an object. It could be worked out, that an error in the software led to wrongly estimated AMR values. The solution and newly determined AMR values are presented in Chapter 5. Although debugging cannot be an essential part of a dissertation thesis, the change regarding AMR value variation, studied at AIUB for years, was fundamental.

In Chapter 6, the conclusions summarise the results of this thesis.

Chapter 2

Survey Strategies

All of old. Nothing else ever.
Ever tried. Ever failed. No
matter. Try again. Fail again.
Fail better.

Samuel Beckett

No! Try not. Do or do not. There
is no try.

Yoda

Astronomical surveys involve imaging the total sky or selected regions. The first historical surveys of stellar positions were the astrometric star surveys by Aristyllos (fl. ca. 280 BC), Hipparchus (ca. 190 − ca. 120 BC) and Claudius Ptolemy (ca. 90 − ca. 168 AD) to measure stellar positions. Stellar positions became known more and more accurately after the invention of the telescope.

Astronomers in ancient Greece classified stars by their apparent brightness. They sorted them, starting with 1st magnitude for the brightest ones to 6th for those, which can barely be seen with naked eyes. Later, this scale was expanded to brighter and fainter objects and also to fractions of integers for a more precise scale.

But stars were only a start, as time went by the objectives became more and more diverse: from stars to asteroids, nebulae and at last space debris. Nebulae were classified even before it was discovered that they are actually galaxies, a gravitational bound system with stars like the Milky Way.

Besides detecting new objects and obtaining enough observations per object, surveys also allow to collect statistical information. For example, by detecting asteroids down to a certain magnitude in a region of the sky, one can make an estimation about the whole population.

The same considerations are valid for artificial objects orbiting around the Earth, including space debris. On the one hand, surveys are made to acquire enough observations of these objects to determine their orbits and maintain them in a catalogue, on the other hand they may be designed to collect statistical information. First of all, one has to think about, where such objects might be best found. As mentioned before, satellites are revolving around the Earth in three different regions and are roughly classified by the semi-major axis of their orbits: in Low Earth Orbits (LEO), Medium Earth Orbits (MEO) and the geostationary ring (GEO). A reasonable conclusion is that space debris is located in the same orbital regions as active satellites.

For the applied survey scenario the following optimisation criteria are chosen: The coverage of the observed region must be large enough or ideally leak-proof, in order to estimate the space debris population

down to the limiting magnitude of ZimSMART. Observing the visible part of the geostationary ring, one can state how many objects, which are brighter than the limiting magnitude of ZimSMART, are in the region. For the MEO region the conclusion is, that if the space close to an orbital plane is observed completely, one can state how many objects, again brighter than the limiting magnitude, populate that plane.

2.1 Apparent Motion of Objects

The position and velocity vector $(\vec{r}, \vec{v})$ at a certain epoch, so-called state vector, are equivalent to the six parameters $(a, \varepsilon, i, \Omega, \Pi, T_\Pi$, "classical" or Keplerian elements) of an orbit at a certain epoch, called osculating elements. Both sets can be converted into each other.

Starting with the classical elements, first the state vectors in the orbital plane are derived, denoted by the index Π (notation taken from [Beut 05]).

$$\vec{r}_\Pi = \begin{pmatrix} a\left(\cos(E) - \varepsilon\right) \\ a\sqrt{1 - \varepsilon^2}\sin(E) \\ 0 \end{pmatrix} \tag{2.1a}$$

$$\dot{\vec{r}}_\Pi = \dot{E} \begin{pmatrix} -a\sin(E) \\ a\sqrt{1 - \varepsilon^2}\cos(E) \\ 0 \end{pmatrix} \tag{2.1b}$$

The angle E is called eccentric anomaly, because it takes the eccentricity of the orbit into account. It is measured from the centre of the ellipse and is the angle between the perigee of the orbit and the position of an object projected onto the auxiliary circle with a radius equal to the semi-major axis a. Consequently, the value $E = 0\,(\widehat{=}0°)$ represents the direction of an object's perigee, $E = \pi\,(\widehat{=}180°)$ the apogee. The mean anomaly M is defined for the position of an hypothetical object, assuming this object moves on a circular orbit with the same mean motion n of the TLE object. The zero point is at the perigee of the corresponding TLE object, a necessary convention as there is no perigee defined for circular orbits. The mean anomaly is measured from the centre of the circle.

The algebraic connection between mean anomaly M, eccentric anomaly E and epoch of the passage through the perigee T_Π is done by Kepler's equation:

$$M = E - \varepsilon\sin(E) = 2\pi \cdot n\,(t - T_\Pi)\,, \tag{2.2}$$

and consequentially

$$\dot{E} = \frac{2\pi \cdot n}{1 - \varepsilon\cos(E)}. \tag{2.3}$$

For Eq. (2.2) there is no analytical solution for E, it has to be solved with iterative procedures, e. g. the Newton method or the Banach fixed-point theorem. The mean motion n can be calculated via 3rd Kepler's law of planetary motion:

$$n\,[\text{rad/s}] = \sqrt{\frac{G\left(M_\oplus + m\right)}{a^3}}$$

$$\approx \sqrt{\frac{GM_\oplus}{a^3}}\,, \tag{2.4}$$

whereas G is the gravitational constant, $M_\oplus$ the Earth's mass and a the semi-major axis of the orbit of the object. Every satellite and space debris object has negligible mass with respect to the Earth, therefore it is $M_\oplus + m \approx M_\oplus$.

Using the absolute value of the state vector, one can calculate the geocentric distance of an object and its velocity:

$$r_\Pi = a\left(1 - \varepsilon\cos\left(E\right)\right), \tag{2.5a}$$

$$\dot{r}_\Pi = an\sqrt{\frac{1 + \varepsilon\cos\left(E\right)}{1 - \varepsilon\cos\left(E\right)}}. \tag{2.5b}$$

The highest velocity is achieved, when passing the perigee ($E = 0$), the lowest one, when passing the apogee ($E = \pi$):

$$\dot{r}_\Pi(E = 0) = an\sqrt{\frac{1 + \varepsilon}{1 - \varepsilon}},$$

$$\dot{r}_\Pi(E = \pi) = an\sqrt{\frac{1 - \varepsilon}{1 + \varepsilon}}.$$

For earthbound observations, the angular velocity triggers the tracking velocity. From the theory of circular motion there is a relation between the geocentric angular velocity ω, the true velocity $\dot{r}$ and current geocentric distance r:

$$\omega = \frac{\dot{r}}{r}. \tag{2.7}$$

Using r from Eq. (2.5a) and $\dot{r}$ from (2.5b) this becomes

$$\omega = n\sqrt{\frac{1 + \varepsilon\cos\left(E\right)}{\left(1 - \varepsilon\cos\left(E\right)\right)^3}} \tag{2.8}$$

$$= n \qquad\qquad\qquad \text{for circular orbits}\,(\varepsilon = 0)$$

As mentioned before, the Earth rotates around its axis with a period of $23\,\text{h}\,56\,\text{min}\,4.099\,\text{s}$. Table 2.1 shows a list of angular velocities of the different investigated orbit regions. The last column gives the approximate apparent angular velocities as seen from the Earth's surface; circular orbits ($\varepsilon = 0$) are assumed.

Table 2.1: Angular velocities of objects in the investigated orbital regions

Orbital region	Period (h:min)	angular velocity ω ($^\circ\,\text{h}^{-1}$)	apparent angular velocity ω' ($^\circ\,\text{h}^{-1}$)
Geostationary ring	23:56	15.04	0.0
GPS	11:58	30.08	15.04
GLONASS	11:15	32.0	16.96

In the following, observation scenarios for the geostationary ring as well as for the MEO region are presented. As a simplification, only one type of survey (either GEO or MEO) is assumed to be performed at a time, especially for the determination of the coverage of the sky. Otherwise, it would not be possible to justify the decision in favour of one line up.

2.2 Geostationary Ring

In this section, survey scenarios for the geostationary ring are presented. Any applied scenario should be leak-proof, i.e. the visible part of the geostationary ring should be observed completely within one
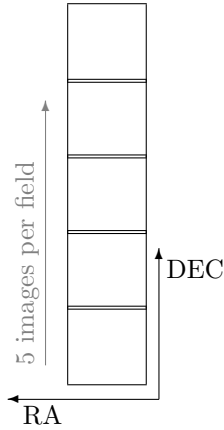
Figure 2.1: Scheme of a single stripe, true to scale

night. Only operating this way, a catalogue of objects down to the limiting magnitude of the ZimSMART set-ups can be complete. Otherwise, drifting objects might not be observed often enough to maintain their orbits.

Regarding the orbit determination it might be sensible to have several tracklets of an object within one night. Depending on the applied survey scenario this can contradict the leak-proof approach. In this case a compromise must be found.

Due to the limiting magnitude of the ZimSMART set-ups, an object catalogue will contain only bright objects.

2.2.1 Survey Scenarios

T. Payne presented a survey scenario for the geostationary ring and the nearby graveyard orbits, which he called "Vertical Graveyard Opposition Search" (see [Payn 03]). Basically, the observations are taken in a declination stripe at fixed right ascension. The orbital plane of an uncontrolled object, which starts at an inclination of $0°$ will acquire a larger inclination over time due to the perturbations of the Sun, Moon and the gravitational potential of the Earth. The inclination reaches a maximum value of about $15°$. Consequently, one stripe has to cover at least $15°$ in declination, if the entire visible area of the geostationary ring should be observed. The number of fields for each declination stripe has to be adapted to the field of view (FoV) of the telescope. For ZimSMART in the third set-up, one stripe consists of five fields, separated by $4°$ in declination, which is nearly the size of the FoV. The FoV is slightly larger, so there is a small overlap between two fields. For example, if the centre of the lowermost field points towards $\alpha = 0^h, \delta = 0°$, all other fields will point towards $\alpha = 0^h$ and $\delta = 4°$, $\delta = 8°$, $\delta = 12°$ and $\delta = 16°$ (see Fig. 2.1).

T. Payne (see again [Payn 03]) states that it is optimal to place the declination stripes at fixed right ascensions both sides right next to the shadow cone of the Earth to take advantage of the optimal illumination of the objects. These stripes have to be adjusted regularly to avoid a stripe moving into the shadow cone. However, with ZimSMART another scenario, using four stripes at fixed right acsensions, is used. The procedure is described in detail in Section 2.2.1.3. First, the components of the used scenario are presented: the single stripe and the pair of stripes. Each of them can also be used as a single scenario, but it is less efficient than the final scenario.

2.2.1.1   One single Stripe

The size of the FoV defines the time which an object stays within the FoV when sidereal tracking is used, the so-called FoV crossing time, measured from one edge of the FoV to the opposite. For the first and third set-up of ZimSMART the FoV is 4.1°. The angular velocity ω of an object in the GEO region is about $15.04° \, \mathrm{h}^{-1}$ with respect to the celestial background and the crossing time is:

$$t_{\mathrm{cross}} = \frac{\mathrm{FoV}}{\omega}$$
$$\approx 981.3 \, \mathrm{s}$$

Observing a field in the geostationary ring with fixed right ascension and declination and assuming an equal distribution of objects in average, there will be an average time interval, after which an object leaves the FoV of about 491 s. Multiple observations might also be possible when working with only one stripe, if after 491 min the observation of the stripe is finished and can be started from the beginning.

From the values presented in Section 1.2, the time to observe one complete stripe may be determined. This time is called cycle time for one stripe, t_{cycle1}. The cycle time for one stripe with five fields and five images per field is given by:

$$t_{\mathrm{cycle1}} = \sum_{i=1}^{5} \Big(5 \cdot \text{exposure time field } i + 5 \cdot \text{read-out time field } i \Big)$$
$$+ \, 4 \cdot \text{inter-field slewing time} + 1 \cdot \text{intra-stripe slewing time}$$
$$= 5 \cdot (5 \cdot 7\,\mathrm{s} + 5 \cdot 7.12\,\mathrm{s}) + 4 \cdot 7.7\,\mathrm{s} + 1 \cdot 21.3\,\mathrm{s}$$
$$\approx 405.1\,\mathrm{s}$$

The intra-stripe slewing time represents the motion of the telescope back to the first field. In principle, it is possible to obtain a second tracklet of an object within one night with only stripe, because the cycle time is lower than the FoV crossing time.

Coverage of the Geostationary Ring

With ZimSMART in the first and third set-up the covered area of the sky by one stripe is $6.1° \times 20.1° = 82.41 \, \mathrm{deg}^2$. After the FoV crossing time t_{cross} derived above, an area of the sky is observed which was not observed before. If the cycle time of the observations is larger than the crossing time a complete new area of the sky will be observed, but between those two areas there would be a gap. A cycle time smaller than t_{cross} leads to a coverage without gaps. On the other hand, then only a fraction of the stripe covers a new area of the sky. For the determined cycle time t_{cycle1} this fraction is:

$$A_{\mathrm{new}} = 82.41 \, \mathrm{deg}^2 \cdot \frac{t_{\mathrm{cycle1}}}{t_{\mathrm{cross}}}$$
$$\approx 34.02 \, \mathrm{deg}^2$$

Assuming continuous observations during the night, the total area of the sky, which can be observed, is determined as follows: The first stripe is completely new, from the second cycle then only a fraction thereof.

$$A_{\mathrm{tot}} = 82.41 \, \mathrm{deg}^2 + 82.41 \, \mathrm{deg}^2 \cdot \frac{t_{\mathrm{cycle1}}}{t_{\mathrm{cross}}} + 82.41 \, \mathrm{deg}^2 \cdot \frac{t_{\mathrm{cycle1}}}{t_{\mathrm{cross}}} + \ldots$$

This procedure continues as long as it is dark enough, so one can set up the number of cycles that are performed. The number of cycles is in first order approximation the length of the night divided by the

cycle time:

$$n_{\text{cycle}} = \frac{t_{\text{night}}}{t_{\text{cycle1}}}$$

Then A_{tot} can be expressed by the cycle time, the number of cycles and the crossing time, Eq. (2.9), or by the cycle time, the length of the night and the crossing time, Eq. (2.10), respectively:

$$
\begin{aligned}
A_{\text{tot}} &= 82.41\,\text{deg}^2 + 82.41\,\text{deg}^2 \cdot \frac{t_{\text{cycle1}}}{t_{\text{cross}}} + 82.41\,\text{deg}^2 \cdot \frac{t_{\text{cycle1}}}{t_{\text{cross}}} + \dots \\
&= 82.41\,\text{deg}^2 + (n_{\text{cycle}} - 1) \cdot \frac{t_{\text{cycle1}}}{t_{\text{cross}}} \cdot 82.41\,\text{deg}^2 \\
&= 82.41\,\text{deg}^2 \left(1 + \frac{t_{\text{cycle1}}}{t_{\text{cross}}} \cdot (n_{\text{cycle}} - 1)\right) & (2.9) \\
&= 82.41\,\text{deg}^2 \left(1 + \frac{t_{\text{cycle1}}}{t_{\text{cross}}} \cdot \left(\frac{t_{\text{night}}}{t_{\text{cycle1}}} - 1\right)\right) \\
&= 82.41\,\text{deg}^2 \left(1 + \frac{t_{\text{cycle1}}}{t_{\text{cross}}} \cdot \frac{t_{\text{night}} - t_{\text{cycle1}}}{t_{\text{cycle1}}}\right) \\
&= 82.41\,\text{deg}^2 \left(1 + \frac{t_{\text{night}} - t_{\text{cycle1}}}{t_{\text{cross}}}\right) & (2.10)
\end{aligned}
$$

In Central Europe the length of the night varies with the seasons and there is not a general value for A_{tot}. The longest night of the year, corresponding to the winter solstice, is in December, the shortest night (summer solstice) is in June. Table 2.2 shows the lengths of the night and the coverage of the geostationary ring in the solstices, according to Eq. (2.10).

Table 2.2: Coverage of the geostationary ring with a single stripe

	Length of the night (hh:mm)	Coverage of the geostationary ring (deg^2)
Summer solstice	5:52.7	1825.6
Winter solstice	13:39.7	4178.7

The fraction of the geostationary ring, which can be observed from Zimmerwald, is about 120° in longitude. With the extension of the GEO population of about 15° in declination, the observable area becomes 1800 deg^2. In short summer nights already, the complete visible part of the geostationary ring can be observed. In longer winter nights, the observed stripe will set during the night, and if no other stripe is defined, one will loose observation time. This can be compensated by defining a new stripe, which rises, when the other one sets.

2.2.1.2 One Pair of Stripes

As shown in the previous section, the crossing time through the field of view is only a little bit larger than the cycle time, t_{cycle1}. That means, there would only one tracklet be obtained for many objects would within one night. For orbits as exact as possible, objects should be observed multiply. This is important when an orbit has to be propagated for a longer time span without new observations (e.g. for a drifting object). Less accurate orbital elements will lead eventually to an orbit which does not represent the true orbit anymore, and the object will not be observed, consequently.

Therefore, the declination stripes can also be grouped in pairs. When the separation is set to 1^{h} in right ascension ($\widehat{=}15°$), objects in nearly geostationary orbits are visible in a field of the second stripe 1 h after

being detected in a field of the first stripe. In Fig. 2.2 there is a scheme of this survey scenario. Again, each square represents one FoV of the telescope. Figure 2.2 a) shows a single stripe, while Fig. 2.2 b) shows the alignment of a pair of stripes.
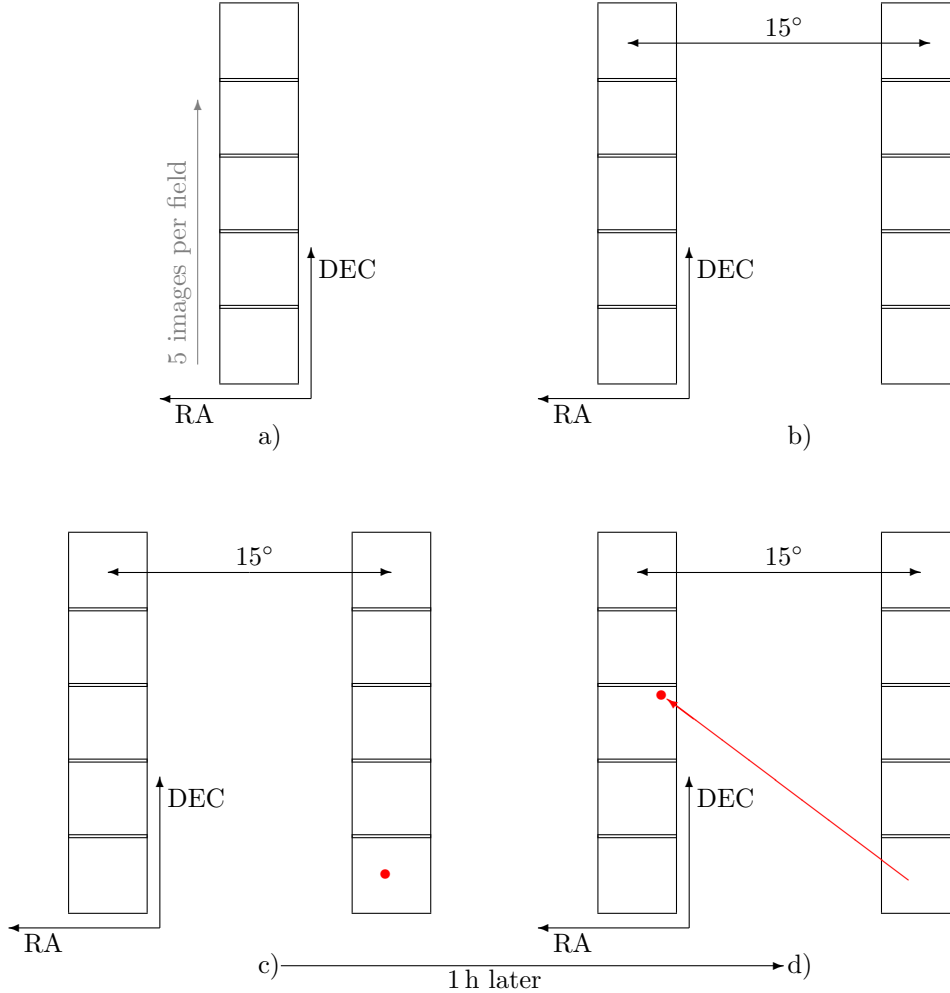
Figure 2.2: Survey scenario for the geostationary ring (scheme)

The lower panels of Fig. 2.2 show exemplarily the detections of an object (red dot) within one night: First, it was detected in the lowermost field of the stripe, Fig. 2.2c. After one hour the object was observed in the second stripe and was found in the middle field, Fig. 2.2 d); the position within the field is shifted to the right. This implies that the object moved less than 15° in right ascension within an hour, but along-track it moved approximately 15°.

There are three critical cases, where an object cannot be found in the second stripe:

1. The object is not yet in the FoV of the second stripe or is currently moving out of one. This corresponds to a semi-major axis larger than 42 164 km or an object with an eccentric orbit near its apogee.

2. The object is not anymore in the FoV of the second stripe or again moving out. This corresponds to a semi-major axis smaller than 42 164 km or an object with an eccentric orbit near its perigee.

3. The object has moved out of the stripe in Northern or Southern direction. This corresponds to an

object with an inclined orbit.

The observations of one pair consist of 2×5 fields with 50 images (2×5×5), eight inter-field changes and two intra-pair changes. So the cycle time results in:

$$
\begin{aligned}
t_{\text{cycle2}} = \sum_{i=1}^{10} \Big(& 5 \cdot \text{exposure time field } i + 5 \cdot \text{read-out time field } i \Big) \\
& + 8 \cdot \text{inter-field slewing time} + 2 \cdot \text{intra-pair slewing time} \\
& = 10 \cdot (5 \cdot 7\,\text{s} + 5 \cdot 7.12\,\text{s}) + 8 \cdot 7.7\,\text{s} + 2 \cdot 21.0\,\text{s} \\
& = 809.6\,\text{s}
\end{aligned}
$$

Comparing this cycle time to the FoV crossing time, one sees that it is smaller than the crossing time. This scenario is therefore leak-proof.

Coverage of the Geostationary Ring

Let us assume that at the beginning of the observations only the first declination stripe has fully risen. Then, one hour later when the second stripe rises, the same part of the geostationary ring is observed again. But this is only relevant, if the observed area of the sky has to be calculated. Thus, Eq. (2.10) can be used again, with only the value of the cycle time to be modified.

$$
A_{\text{tot}} = 82.41 \deg^2 \left(1 + \frac{t_{\text{night}} - t_{\text{cycle2}}}{t_{\text{cross}}} \right)
$$

Table 2.3 shows the calculated values for a pair of stripes. As one can see they are smaller, but still large enough to cover the complete visible part of the geostationary ring within most nights. Only in the shortest summer nights a small fraction stays unobserved.

Table 2.3: Coverage of the geostationary ring with a pair of stripes

	Length of the night (hh:mm)	Coverage of the geostationary ring ($\deg^2$)
Summer solstice	5:52.7	1791.6
Winter solstice	13:39.7	4144.7

Here again, in winter nights the observed pair of stripes will set during the night and to avoid a loss of observation time another pair has to be defined, which rises while the other one sets.

2.2.1.3 Two Pairs of Stripes

A second pair of stripes can be defined in order to compensate a possible reduction of the coverage of the geostationary ring. This is the case when other regular tasks are scheduled or at times when system failures occur. The probability to observe an object multiple times is increased, because it can be observed in both pairs and not only in the second stripe of the first pair. Consequently, for each object up to four tracklets can be achieved with in one night. Figure 2.3 shows a possible line-up of two pairs of stripes. The separation between two stripes of a pair is 15°, the separation D between the two pairs depends on the requirements: it can be in such a way to ensure one pair rises around sunset and the other pair set around dawn, or in can be about 20° to the East and to the West of the shadow cone of the Earth.

When determining of the cycle time it has to be taken into account that there are more inter-field slews, several inter-stripe slews and, of course, more exposures than with one pair of stripes. Both pairs of
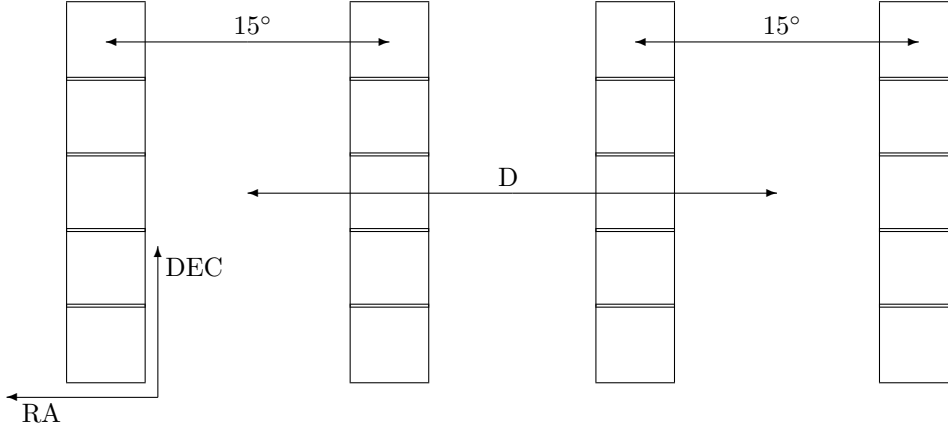
Figure 2.3: Possible line-up of two pair of stripes (scheme); within one pair, the stripes are separated by 15°, the separation of the two pairs, D, is arbitrary

stripes have to be observed completely, as well as one single stripe of the first pair. Four stripes are observed completely, which corresponds to 4×5 fields. In each cycle 100 images (4×5×5) are taken. For every stripe, each consisting of five fields, there are again four inter-field changes, which results in a total of 16 per cycle. There are also two intra-pair slews and two inter-pair slews.

$$
\begin{aligned}
t_{\text{cycle4}} = \sum_{i=1}^{20} & \Big(5 \cdot \text{exposure time field } i + 5 \cdot \text{read-out time field } i\Big) \\
& + 16 \cdot \text{inter-field slewing time} + 2 \cdot \text{intra-pair slewing time} \\
& + 2 \cdot \text{inter-pair slewing time} \\
& = 20 \cdot (5 \cdot 7\,\text{s} + 5 \cdot 7.12\,\text{s}) + 16 \cdot 7.7\,\text{s} + 2 \cdot 21\,\text{s} + 2 \cdot 26.1\,\text{s} \\
& \approx 1629.4\,\text{s}
\end{aligned}
$$

The cycle time t_{cycle4} is only valid when first both stripes of one pair and then the other pair is observed. Otherwise more inter-pair slews would happen and t_{cycle4} would increase. This scneario is not leak-proof anymore, as the cycle time is larger than the FoV crossing time.

A natural number of cycles and one additional stripe have to be performed within an hour to redetect an object. It is easy to see that an object may be detected again after two cycles:

$$
\begin{aligned}
t_{\text{redetect}} &= 2 \cdot t_{\text{cycle4}} + t_{\text{cycle1}} \\
&= 61.1\,\text{min}
\end{aligned}
$$

This is again only correct when first one pair is observed completely and thereafter the second one. Then, most objects, which were found in the first stripe of one pair, will be observed again in the corresponding second stripe; only those, which were close to one edge will have moved out already. Therefore, the quality of the subsequent orbit determination is improved.

One possible scenario is to define one pair such that it rises when the observations begin, and the other one that it sets when observations end. This ensures that always at least one pair is visible and no observation time is lost.

2.2.1.4 Other possible Line-ups

The arrangement of the declination stripes can be generalised. It is in principle not necessary to limit the number of stripes to four, but one has to be aware that more visible stripes imply higher cycle times and possibly not a complete coverage of the visible part of the geostationary ring.

The Fence

In this line up stripes are defined which are separated equidistantly from each other along the geostationary ring, as presented in [Payn 03]. A separation of e. g. 1^h in right ascension implies that 24 stripes are defined, with a 30^m separation 48 stripes are defined.

Four to five stripes are observable simultaneously at Zimmerwald, depending on the declination of the lowermost field. During the night, some stripes will rise, others will set (also depending on the length of the night). The coverage of the visible part of the geostationary ring might be complete, only in a sequence of nights. The total number of stripes, which are observed within one night, will change with the seasons; more stripes will rise in longer nights.

The cycle time is larger compared to the scenario with two pairs of stripes when five stripes are observed simultaneously. On the other side, the probability is higher to detect an object multiple times due to the equidistant separation: with 12 equidistant stripes, objects cross one stripe every hour. An object can be redetected in the second next or third stripe that is observed in that night, whereas with pairs of stripes observations are only possible in the next stripe and possibly in the second pair. The time difference and number of observations is large enough to achieve a good quality orbit, such that follow-up observations in subsequent nights are possible, too. Furthermore, with the survey-only approach of ZimSMART, having good quality orbits allows the association of tracklets to catalogued objects more efficiently. With less accurate orbits, either tracklets are not associated at all or some tracklets are associated wrongly to objects.

From a geocentric point of view, it appears as if the Earth was surrounded by a fence and the declination stripe are the posts. Figure 2.4 shows a possible alignment of the stripes. The left declination axis refers to a geocentric system, while the right one refers to a topocentre located at the observatory in Zimmerwald. Some stripes must be removed or at least moved out of the belt, to avoid observations of the galactic plane: There are too many stars and the identification of catalogue stars and the extraction of their positions is very time consuming. The borders of the galactic latitude are set to $\pm 15°$, in between this interval no stripes are defined and the stripe at 17^h in right ascension, close to the galactic plane, is shifted until it is outside of the densest part of the Milky Way.

The Grid

If the separation between two declination stripes is as large as the FoV of the telescope, there is no gap between the stripes. By defining several stripes in this manner one gets a grid, which scans the sky. If the cycle time is small enough, it is ensured that objects are observed multiple times. The disadvantage is that the coverage of the visible part of the geostationary ring might not be completed within one single night and the achieved tracklets of one night are spaced by small time intervals.

This scenario can be used, when a single objects is searched. If the ephemerides are roughly known, then one can build a grid around a the ephemerides for a certain epoch. The searched objects might then be found in one of the fields.

2.2.2 ZimSMART GEO Surveys

With ZimSMART the stripes were defined as follows: one pair raised, when the evening twilight ended, and the other pair set, when the morning twilight started. Therefore it was ensured that always at least
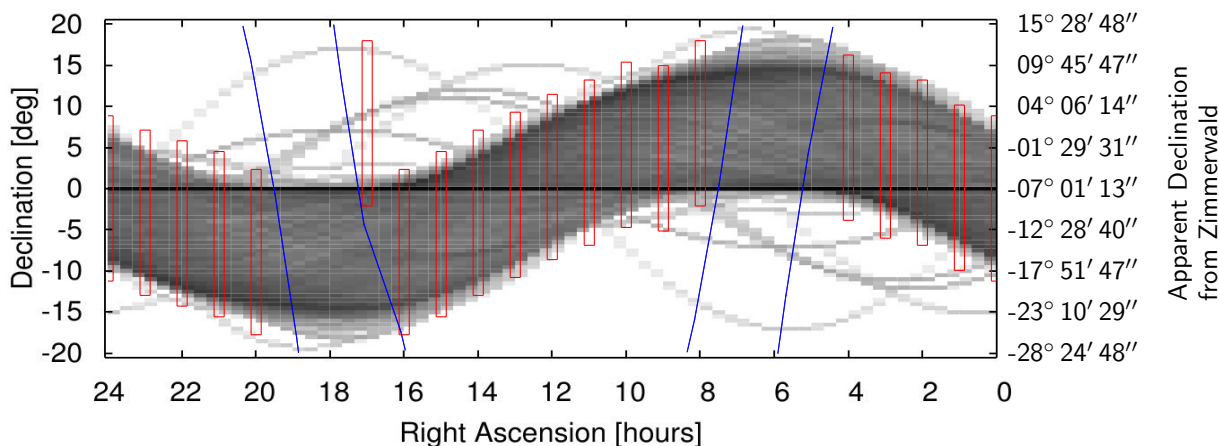
Figure 2.4: Object density and extent of the geostationary ring (as of March 8th, 2012), possible locations of the stripes in red (to scale) and the galactic latitudes $\pm 15°$ in blue; the left axis represents geocentric coordinates, the right axis represents the coordinates as seen from Zimmerwald

one pair of stripes was visible.

In principle, there is no limitation how many stripes or how many fields per stripe can be observed per night. But as pointed out in the previous section, if more pairs are defined, it will become more unlikely to observe an object twice a night. Furthermore, the scenario is not leak-proof anymore.

Ideal geostationary objects are standing above one fixed point on the Earth's equator seen from a given topocentre during their revolutions; their apparent angular velocity in an Earth-fixed system is $0° \, h^{-1}$. The angular velocities of real objects in the geostationary ring will deviate from this value, because real geostationary orbits are perturbed by the gravitational potentials of the Earth, the Moon and the Sun, respectively. This deviations are small enough that they can be neglected during one observation series.

Therefore, a so-called blind tracking observation mode was used: The telescope moved with $15.041° \, h^{-1}$ with respect to the celestial background during one series of five exposures, i. e. was fixed in the horizon system. All observed objects appeared point-like and stayed approximately at the same positions on each frame which simplified the object recognition step. The more the angular velocity deviated from $15.041° \, h^{-1}$ the more elongated the objects appeared, and they moved between two images.

This is different to the observation mode of the ESASDT (see [Schi 07]). After each exposure the telescope is moved back to the first position. With this method observations are taken with the same background stars. As a disadvantage the objects move on the frame and finally move out of the frame. Objects with an angular velocity higher than $15.041° \, h^{-1}$ will move out of the frame even faster, especially when they are close to the edge.

Due to the large FoV of ZimSMART in all set-ups, many stars of the first image were also on the last image, so the conditions for the astrometry were similar to the ESASDT.

2.2.3 GEO Survey Results

Observations started in June 2008. Until December 2011, the observation period consisted of 387 nights, divided into the periods of the three set-ups of ZimSMART:

Firstly, between June 2008 and August 2009 the optical tube assembly of Takahasiwith a FoV of $4.1° \times 4.1°$ was used to observe within 93 nights. After the telescope exchange, between September 2009 and February

2010 the ASA Astrograph with a FoV of $2° \times 2°$, observations were taken within 35 nights. Finally, the optical tube assembly of Takahashi was used again from April 2010 to December 2011 within 259 nights. The third set-up was used for the longest time.

Until January 2011, ZimSMART observed in GEO survey-only mode, so most observations were GEO survey images. Between GEO surveys, GPS satellites were observed for calibration measurements. From January 2011, the telescope observed in GEO/MEO survey-shared mode, where between the GEO surveys not only calibration measurements were performed but also images of the MEO surveys were taken. The exact sequence of GEO survey observations, MEO survey observations and calibration measurements was chosen by the telescope software, depending on the individual visibilities and predefined priorities.

2.2.3.1 Images taken

Figure 2.5 shows the repartition of the observations with respect to observation type, first in the GEO survey-only mode until January 19th, 2011 and then in the GEO/MEO survey-shared mode from January 22nd, 2011 on. The last panel shows the composition over the entire analysed interval.

(a) From June 9th, 2008 till January 19th, 2011

(b) From January 22nd, 2011 till December 13th, 2011

(c) Entire interval (June 2008 till December 2011
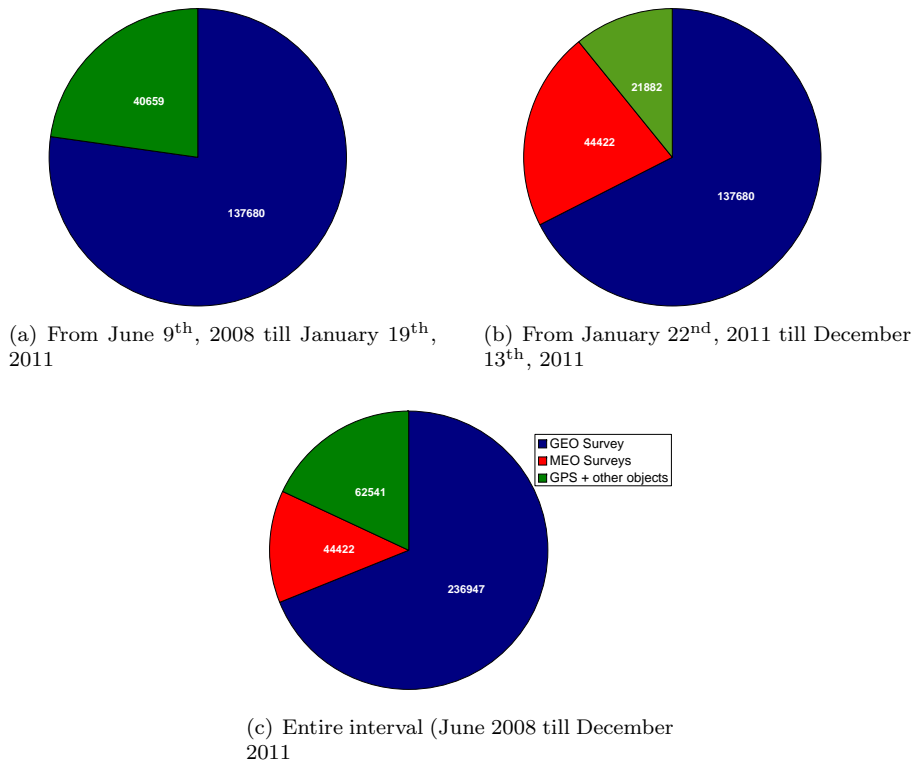
Figure 2.5: Composition of images taken with ZimSMART subdivided into the individual campaigns

More than 178000 images were taken during the first period. Thereof, more than 137000 images ($\hat{\approx} 77\%$) of all images taken belong to GEO surveys, the other almost 41000 images ($\hat{\approx} 23\%$) are calibration measurements of GNSS satellites.

In the second period, more than 165000 images were taken, the numbers are therefore comparable. With more than 99000 images ($\hat{\approx} 60\%$) of GEO surveys and almost 22000 calibration images ($\hat{\approx} 13\%$), both fractions were reduced. They were not lowered equally as the fraction of GEO survey images went from 77% to 60% (-17%), but the calibration images were reduced from 23% to 13% (-10%). The other

44000 images ($\widehat{\approx} 27\,\%$) belong to the MEO surveys.

The number of observed calibration objects could be controlled in the planning phase.

Figure 2.6 shows the distribution of the images taken per month, divided into the same observation types as above. A seasonal variation in the number of observations can be observed. Unfortunately, the data between October 2009 and April 2010 is missing. In that time interval, the set-ups of ZimSMART changed. The green lines mark the changes of the set-ups of ZimSMART, which are denoted above the graph.
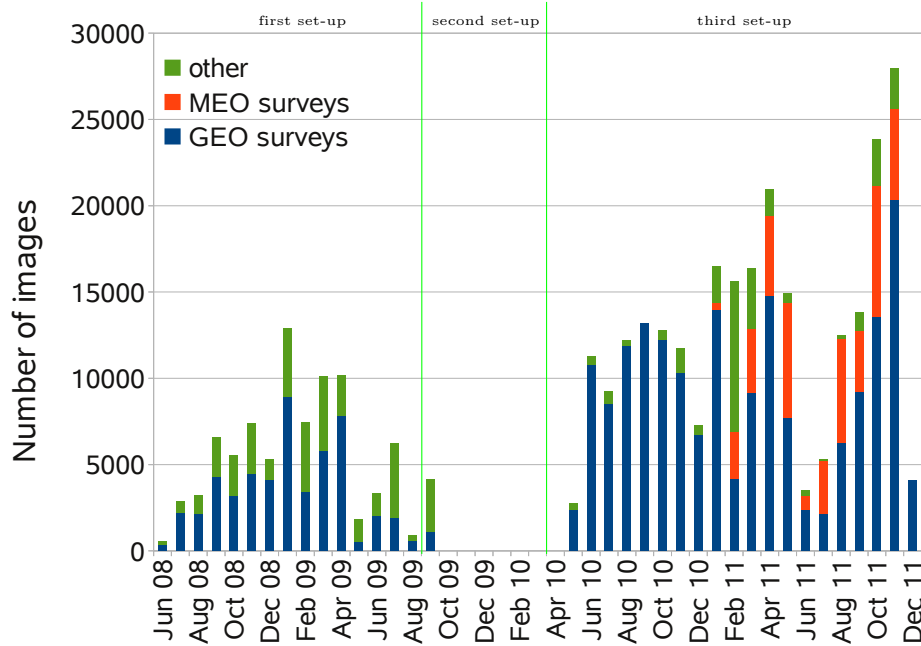
Figure 2.6: Images per month and by observation type

2.2.3.2 True Coverage of the Geostationary Ring

To show how the survey scenario is applied in reality, the pointing of the telescope for each observation should be shown. This information was only available when analysing the exposures themselves, but only if an object was observed a tracklet was created. Without an observed object in a field, and therefore without tracklets, the pointing direction was not available, so the positions of each observed object are shown instead. The coverage of the part of the geostationary ring observable from Zimmerwald within the night June 23$^{\text{rd}}$ to 24$^{\text{th}}$, 2010 is shown in Fig. 2.7a). This night was close to the summer solstice and therefore one of the shortest nights during the year. The controlled geostationary satellites form an arc in Fig. 2.7a).

This graph does not show all the observed frames but only those frames where at least one object could be detected. The coverage of the observed frames will be complete as long as the coverage of the detections already is.

The coverage of the geostationary ring in Fig. 2.7a) is nearly complete, even in the presented summer night. A large coverage can be achieved within a few consecutive nights as shown in Fig. 2.7b), where

observations of eight subsequent nights between June 23$^{\text{rd}}$ and June 30$^{\text{th}}$ are plotted. Going to even longer time intervals, e. g. one year (Fig. 2.7c) with all nights in 2011), the coverage is complete.

The year 2011 was chosen, because the observation were alternating between GEO and MEO surveys, and calibrations measurements as well. When the coverage is complete with both surveys modes, it must have been complete with GEO surveys only, too.
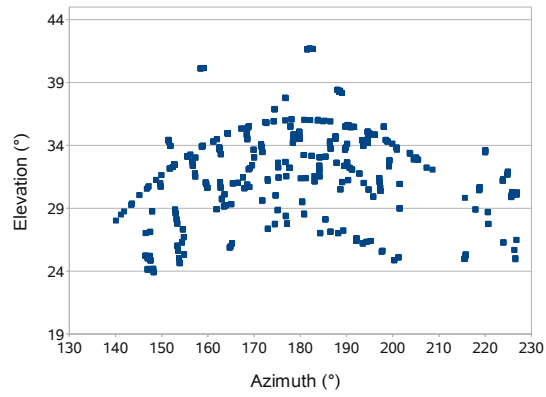
(a) On June 23rd, 2010
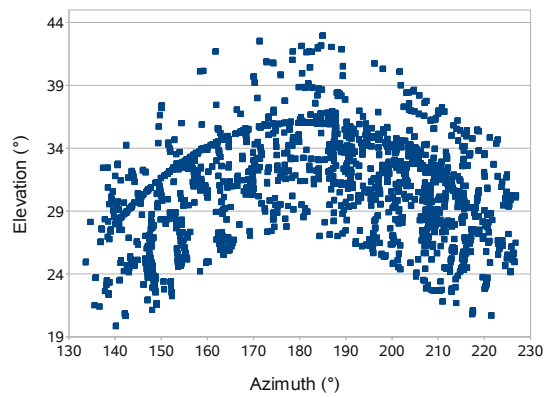
(b) Between June 23rd and June 30th, 2010
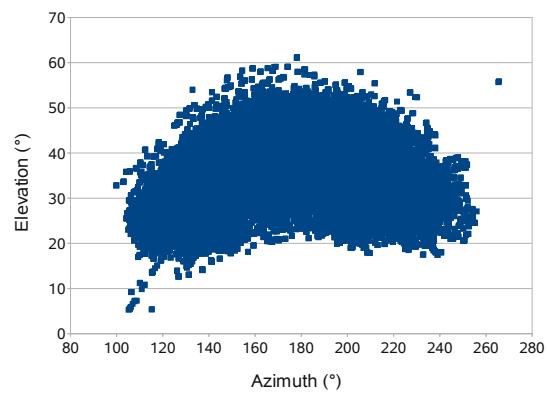
(c) All nights in 2011

Figure 2.7: Coverage of the geostationary ring within different time intervals

2.3 GNSS Orbit Region

The satellite population in the MEO region consists mostly of GNSS satellites. In the future, more satellites, namely those of the currently deployed new GNSS, like "Galileo" and "Compass", will be located in this region. Thus, the probability of space debris being created will increase.

In this section, the survey scenario and underlying theoretical concepts will be discussed. Thereafter, the achieved results will be presented for different orbital planes. The aims are to test the completeness of existing catalogues for objects in this region; or otherwise, include newly detected objects. The cataloguing of objects and detecting new ones only play a minor role.

2.3.1 Explosion Scenario Analysis

Simulations of explosion populations in the MEO region (see e.g. [Schi 09]) showed, that fragments of these explosions stay approximately in the same orbital plane as the satellites they stem from. The term "explosion" stands for fragmentation as well as for collision. A collision can be approximated in first order as a simultaneous explosion of two objects at the same location at the same time.

Two explosion scenarios were studied by T. Schildknecht (see again [Schi 09]): an explosion at the passage of the ascending node and an explosion when the argument of latitude u is equal to $90°$. An explosion in one of these points in the orbit causes the biggest changes of the orbital plane of the fragments, defined by Ω and i.

An explosion at the passage of the ascending node (and so of the descending node) leads to orbits of fragments with similar values of Ω of the parent object's orbit, but the values of the inclination will be broadly distributed, with a standard deviation of $\sigma_i = 1.58°$ (from [Schi 09]).

An explosion at $u = 90°$ (and so at $u = 270°$) leads to a Gaussian distribution of Ω around the value of the parent object. In this case the values of the inclination will be similar to the inclination of the parent object's orbits. The standard deviation of the distribution of values for Ω, which was calculated, was $\sigma_\Omega = 7°$ (see again [Schi 09]).

Explosions at any other point in the orbit lead to a combination of both, i.e. the values of i and Ω will be Gaussian distributed around the values of the parent object.

The apparent motion of the objects with respect to the celestial background is very different compared to GEO objects. The objects complete between 1.70 and 2.13 revolutions per sidereal day, their orbits have semi-major axes between $25\,500\,\mathrm{km}$ to $29\,600\,\mathrm{km}$. This corresponds to orbital periods between $11\,\mathrm{h}\,16\,\mathrm{min}$ and $14\,\mathrm{h}\,7\,\mathrm{min}$. While an object is revolving, the Earth also rotates. The projection of the orbital plane on the sky changes and the tracks on the sky are more complicated than for geostationary objects. Figure 2.8 shows the track of the GLONASS satellite COSMOS 2471 (International Launch Designator: 11009A) in the horizon system in the night of July 12th to 13th, 2011. The points on the curve denote the positions at 21:00, 22:00, 23:00 and 24:00 UTC, respectively. For comparison, the track of the geostationary satellite MSG−2 (05049B) is also plotted for the same time interval. As one would expect, the complete track is represented by a point.

It is evident from Fig. 2.8 that it will be hardly possible to use the same observation scenarios for surveying the MEO region and the geostationary ring.

2.3.2 Observation Scenario

In accordance with the explosion scenario mentioned in Section 2.3.1, space debris stays in or at least near the orbital plane of the parent object. Many objects may stay in the orbital plane of the parent object
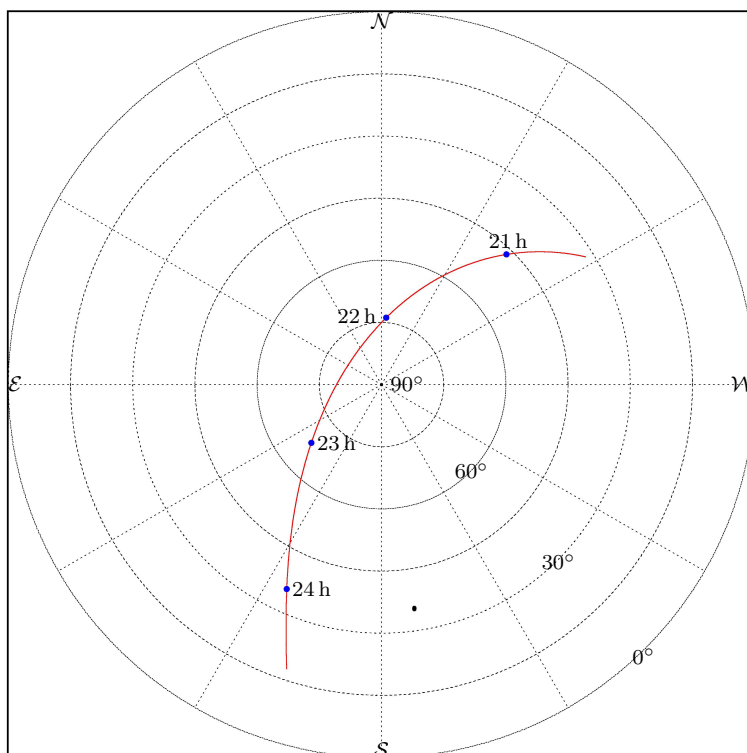
Figure 2.8: Track of the GLONASS satellite COSMOS 2471 (red line and blue dots) and of the geo-
stationary satellite MSG−2 (black dot) in the horizon system as seen from Zimmerwald in
the night July 12th/13th, 2011

and thus also within the FoV of 4.1° (ZimSMART, third set-up) for a certain time span. A reasonable
approach for surveying the MEO region was to investigate the orbital planes of the GNSS satellites.

For the following investigations, the orbital parameters of one particular satellite (the so-called base
object, e.g. GLONASS satellite COSMOS 2471 (11009A)) in the Two Line Element set format (TLE
format) were selected. For details concerning the entries of a TLE, see Appendix A.

Definition of Pseudo-objects

The developed survey senario used pseudo-objects, which are hypothetical objects in the same orbit as a
selected base object. Then, the eccentric anomaly E was varied to get an equal distribution of pseudo-
objects along the orbit and therefore a complete coverage. The variation of the mean anomaly M is
achieved by a variation of E.

Start from a fixed angle, the eccentric anomaly was increased by constant increment (see Fig. 2.9).
Referring to Eq. (2.2), it is $E \approx M$ for orbits with small eccentricities, but the analysis of elliptical orbits
is also possible with this approach.

For a homogeneous coverage of the orbit, the angular separation between to pseudo-objects must not
exceed the FoV of the telescope. It might be smaller than the FoV, then there will be overlaps between
the fields. The angular difference was chosen to be 4°, which is approximately the size of the FoV of
ZimSMART in its third set-up (4.1°). In general, the number of pseudo-objects can be defined as 360°
divided by the size of the FoV. The eccentric anomaly is varied from 4° to 360° in steps of 4°, calculated
the mean anomaly and replaced the original number for each pseudo-object; the other orbital elements
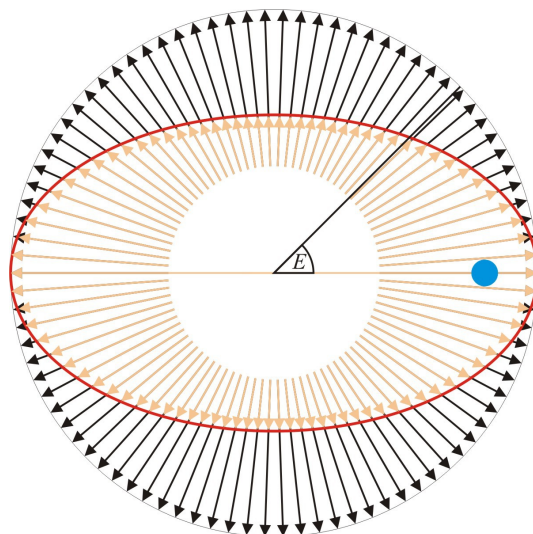
Figure 2.9: Set-up of the pseudo-objects for the MEO surveys (sketch), the light arrows give the pointing directions to the orbit, the black arrows the pointing directions to the auxiliary circle

were taken from the reference object.

```
COSMOS 2471 (GLONASS)
1 37372U 11009A   11185.85021556   00000059  00000-0  10000-3 0  1160
2 37372 064.7823 138.0813 0006739 250.3400 302.6469 02.13109839  2713
Test object 1
1 T-001U MEO001   11185.58021556  .00000059  00000-0  10000-3 0  1160
2 T-001 064.7823 138.0813 0006739 250.3400 003.9973 02.13109839  2713
Test object 2
1 T-002U MEO002   11185.58021556  .00000059  00000-0  10000-3 0  1160
2 T-002 064.7823 138.0813 0006739 250.3400 007.9946 02.13109839  2713
...
Test object 75
1 T-075U MEO075   11185.58021556  .00000059  00000-0  10000-3 0  1160
2 T-075 064.7823 138.0813 0006739 250.3400 300.0334 02.13109839  2713
Test object 76
1 T-076U MEO076   11185.58021556  .00000059  00000-0  10000-3 0  1160
2 T-076 064.7823 138.0813 0006739 250.3400 304.0320 02.13109839  2713
```

Figure 2.10: Excerpt of a TLE catalogue of pseudo-objects with COSMOS 2471 (11009A) as base object

By the definition of the pseudo-objects, they are always in the centre of observed field and in one field there must be the base object. Because the mean anomaly of this object is known also the field of the corresponding pseudo-object is known. This fact was used to check the survey method. In the example shown in Fig. 2.10, the GLONASS satellite had a mean anomaly of 302.6469° (uppermost red box), so it was on the field of pseudo-object MEO076 (302.6469 is closer to 304.0320 than to 300.0334), but close to the edge to the frame of pseudo-object MEO075.

Figure 2.9 shows the set-up of the MEO surveys using pseudo-objects. The blue filled circle is the Earth

in one focal point of the orbit (red curve). The light coloured arrows represent the calculated directions of the pseudo-objects. The angular separation between two arrows is 4° as defined before.

Within a night all visible fields were scheduled for observing, if possible each was observed several times. After observing each field several nights the orbital plane was changed, i. e., a new base object was selected. The total number of images taken of each pseudo-object did not play a major role, but if an object was on several frames, more observations resulted in a more accurate orbit determination.

This scenario is optimised for objects close to the orbital plane of the base object. There are critical cases where an object is not found when the field is observed a second time within one night:

1. The object has moved out of the field. This corresponds to a semi-major axis much different than the one of the base object or an object in an eccentric orbit. If the inclination does not differ more than 2.05° (half the FoV of ZimSMART) from the inclination of the base object the observed object may be found in a neighbouring field.

2. The object has moved out of the field in Northern or Southern direction. This corresponds to an object with an inclination, which differs more than 2.05° from the inclination of the base object. This case is more crucial than for GEO surveys, because only surveys with one field are performed. A possibility for compensation is the installation of declination offsets for each field, resulting in declination stripes comparable to the GEO surveys.

2.3.3 Observation Mode

The observation mode was a mixture between ephemeris tracking and blind tracking. Ephemeris tracking is defined as follows: Ephemerides of the pseudo-objects were generated and used to set the telescope tracking velocity. But the angular velocities were based on the orbit of the base object; therefore, it was also blind tracking.

An equal distribution of images per pseudo-object field and observed nights might not be achieved, i. e. some pseudo-object fields were observed more often than others. The observation software of ZimSMART tried to observe each pseudo-object field, which was visible. When observations were ended prematurely, the software did not keep the information, which pseudo-object was observed and how often. The next night, observations started again, but if it is also ended prematurely, it was possible, that some pseudo-object fields were observed multiple times and others not even once. This can be avoided: those pseudo-object fields with most observations may be excluded in the planning phase. I used this procedure at the end of many observation periods to achieve observations of every pseudo-object field in at least one night.

2.3.4 Correlation between Number of observed Fields and Images taken

If each field of a selected orbital plane was observed regularly and equally, one would have an equal number of images per field and therefore a homogeneous coverage of the orbital plane. In practice this might not be achieved as mentioned before. Nevertheless, one would assume that both distribution are correlated: the more nights one field was observed, the more images were taken.

This correlation may be expressed by the Pearson correlation coefficient between both distributions:

$$\varrho_{I,N} = \frac{\text{cov}\,(X_I, X_N)}{\sigma_I \cdot \sigma_N}, \tag{2.11}$$

where X_I represents the distribution of images per field with its standard deviation σ_I and X_N represents the distribution of nights per field and σ_N its standard deviation. In ideal case, each field was observed an equal number of nights with an equal number of images, the Pearson correlation coefficient is not

defined, because the covariance and both standard deviations are exactly zero. But to give an overview of the success of the scenario, the estimation is sufficient.

The value of $\varrho_{I,N}$ lies between -1 and $+1$, and describes the linear correlation between both data sets. Correlation coefficient values close to $+1$ represent a good linear correlation with a positive slope, while values close to -1 show a good linear correlation with a negative slope. In an $X_I - X_N$-diagram, where the number of nights is plotted with respect to the number of taken images, the points will form a line. The Pearson correlation coefficient does not give any information about the slope of that line and the latter is therefore unknown. For values of $\varrho_{I,N}$ around zero the correlation coefficient does not give clear information: either there is just no linear correlation or no correlation at all.

The purpose of the correlation coefficient is to display the homogeneity of the surveys. Values above 0.7 already represent a very good correlation.

2.3.5 Detected Catalogue Objects

Another indicator how successful the investigation of an orbital plane might have been, besides the correlation coefficient, is the comparison between the objects of the USSTRATCOM catalogue in the surrounding of that orbital plane and the detected objects therein.

When an orbital plane was observed, various objects could be detected, not all of them belonging to the orbital plane of the base object. Firstly, there were those objects of the MEO region with an orbital plane almost coinciding with this of the base object. When scanning the orbit of the base object, those objects should also be detected, if the individual inclinations did not deviate by more than $5°$ and the RAAN did not deviate by more than $4°$ from the values of the base object.

Secondly, objects with different semi-major axes, e.g. LEO objects, with orbital planes almost coinciding with that of the base object by chance. The appearance of those objects were different from the MEO objects as they moved faster. On the images their traces appeared elongated and not point-like anymore. Thirdly, any other object might be detected on frames where the orbital planes of both objects cross each other. Especially some GEO objects were observed this way besides being observed in GEO surveys.

The limits for the semi-major axis were set to exclude any object outside the MEO region. Due to these limits, only objects of the first class mentioned above were included. The data base of observations was investigated, if the selected catalogue objects of each orbital plane were observed.

2.3.6 Estimated Number of populated Fields in an orbital Plane

After analysing an orbital plane one can estimate the number of fields, in which uncatalogued objects are expected to be detected. It can be determined with a statistical approach, e.g. a binomial distribution:

$$B_{n,p}(k) = \binom{n}{k} \cdot p^k \cdot (1-p)^{n-k} \tag{2.12}$$

Let n be the total number of observed fields, k the number of fields containing at least one object and p the probability for a detection. The interpretation is as follows: each field has the same probability p that at least one detectable object is inside and the detection probability of one field is independent from any other field. The unassociated tracklets were analysed with a simple orbit determination, performed with *ORBDET* (see Section 3.1.3.1 for details), whether they were in the same orbital plane like the base object or if they were observed by chance when they crossed the orbital plane of the base object.

The probability p will be unknown but when the values n and k are given, an interval for p, $[p_l, p_u]$, can be calculated. The confidence level α is arbitrary. In the following, the "exact Clopper-Pearson interval"

(proposed by [Clop 34]) with a confidence level $\alpha = 99.73\,\%$ is used.

$$p_l = \left(1 + \frac{n - k + 1}{k \cdot F\left(1 - \frac{\alpha}{2}, 2k, 2\left(n - k + 1\right)\right)}\right)^{-1} \tag{2.13a}$$

$$p_u = \left(1 + \frac{n - k}{(k + 1) \cdot F\left(\frac{\alpha}{2}, 2\left(k + 1\right), 2\left(n - k\right)\right)}\right)^{-1}, \tag{2.13b}$$

where $F(a, b, c)$ is F-distribution.

The probability limits $p_{l,u}$ and the total number of fields in an orbital plane, equal to 90 for ZimSMART in its third set-up, also define an interval of numbers of fields $\mathcal{N}_{l,u}$ within the confidence level, where uncatalogued objects can probably be detected:

$$\mathcal{N}_l = 90 \cdot p_l \tag{2.14a}$$
$$\mathcal{N}_u = 90 \cdot p_u \tag{2.14b}$$

This does not allow any statements how many objects one may detect, but only in how many fields one expects to find at least one object.

2.3.7 Results

In January 2011, MEO surveys with ZimSMART started. First, the orbital plane of the test satellite GIOVE-A (05051A) of the European GNSS Galileo was investigated. Thereafter, two of the orbital planes of the GLONASS system and two NAVSTAR GPS orbital planes were investigated.

To test the performance of ZimSMART concerning highly eccentric orbits with low perigees, the orbit of the Molniya satellite MOLNIYA $1 - 93$ (04005A) was investigated as well.

Under the assumption that no space debris exists within an orbital plane, detections should be only made in fields where known satellites are placed. When an observed field was crossing orbital planes of other objects (GEO or other MEO objects), some of those objects may also be detected.

For the investigated orbital planes, the number of nights with observations as well as the number of images of each pseudo-object field are shown. The number of known objects with orbits near the orbital plane of the base objects are presented, together with the number of actually detected objects. The limits for the selection of known objects were set to $\Delta i = 5°$ and $\Delta \Omega = 4°$. Although the limits are larger than the half of the FoV of ZimSMART, objects on orbits with inclinations and RAAN much different than that of the base object have might also be observed. If the RAAN of two orbits are alike, they may be observed near the RAAN. If the inclinations are similar and the RAAN do not differ much, they may be observed near their upper culmination.

If an object could not be observed, although its orbital elements are similar to those of the base object, it is categorised as "no-show". In general, it should be figured out, why an object could not be observed, it can be a faint object or the phase angle was large at the observation epochs. In the scope of this work, only the number of "no-show" objects is given.

Finally, an estimation about the number of fields, where uncorrelated objects may be found, is made using the Eq. (2.14a) and (2.14b).

2.3.7.1 GIOVE-A orbital Plane

In the orbital plane of GIOVE-A (05051A) no other known object is placed and therefore well suited to test the survey scenario. Observations were acquired in 17 nights on February 4, March 2, April 2 and each

subsequent night with suitable weather conditions between April 18 and May 9, 2011. Figure 2.11(a) shows the distribution of nights each pseudo-object was observed. This is not an equal distribution, which is explained by the observation strategy in the test phase. First, not every visible pseudo-object was scheduled, but only a few. Therefore the acquired number of images of some pseudo-objects is much higher than for others (see Fig. 2.11(b)). While for most pseudo-object fields between 50 and 150 images were taken, the number of images for the pseudo-object fields 5, 15, 23, 25 and 35 is 250 and higher. The number of images of the pseudo-object fields 80 and 85 is higher than 200.

The correlation coefficient $\varrho_{I,N}$ between the number of nights and number of images was about 0.403, due to the test phase at the beginning. The correlation coefficients of the other orbital planes were higher when all visible pseudo-objects of a night were planned and finally observed.

A total of 74 tracklets were extracted, which could not be correlated to catalogued objects. From those, 14 tracklets could be associated in an orbit determination to seven different objects, two tracklets per object. The arc length of each object was only one night.

On closer examination, some observations were not associated to the corresponding object, due to problems in the association process. After solving the latter problem, the tracklets were analysed again and could be associated to the catalogue objects. Table 2.4 shows the object names in the AIUB internal ZimSMART catalogue, the International Launch Designator of the corresponding catalogue objects and the reason, why these were not associated before.

Table 2.4: MEO objects of the AIUB internal ZimSMART catalogue from surveys of the GIOVE-A orbital plane in the observation period between 18/4/2011 and 9/5/2011

Object	Corresponding catalogue object	Reason why not correlated
Z11035G	preliminary uncatalogued	
Z11061B	COSMOS 2459 (10007A)	quality class too low
Z11061C	COSMOS 2444 (08046C)	quality class too low
Z11061D	COSMOS 2461 (10007B)	quality class too low
Z11092N	SL-12 Rocket Body (91025E)	too many candidates
Z11110C	COSMOS 2460 (10007C)	too many candidates
Z11116N	COSMOS 2443 (08046B)	too many candidates

Low quality class means that the deviation of the observations in the tracklets compared to the predicted positions and velocities was too large. This can be a result of one or more outliers in the tracklet. It could be confirmed that those observations belonged to the denoted objects using observations of subsequent nights. All of these objects have a RAAN similar to the base object and were observed close to the position where their orbital planes crossed the orbital plane of the base object.

The orbits of four catalogue objects were within the limits, all of them circular. Each object was observed during the survey.

Another 60 tracklets could not be associated with any other tracklet and remained single. Those tracklets stemmed from 39 fields. Only tracklets from 14 fields contained observations of uncorrelated MEO objects and from those the observations from five different fields were close to the orbital plane of the base object. The other nine fields contained tracklets of objects in other orbital planes.

Using Eq. (2.13a) and (2.13b), the following numbers were derived: $n = 90$ as each field was investigated and $k = 5$, where objects could be found. The Eq. (2.14a) and (2.14b) gave $\mathcal{N}_l = 4.6606 \approx 5$ and $\mathcal{N}_u = 5.6414 \approx 6$, respectively.

Because all known objects near the orbital plane were found, the survey scenario was declared successful and applied to other orbital planes of the GNSS.
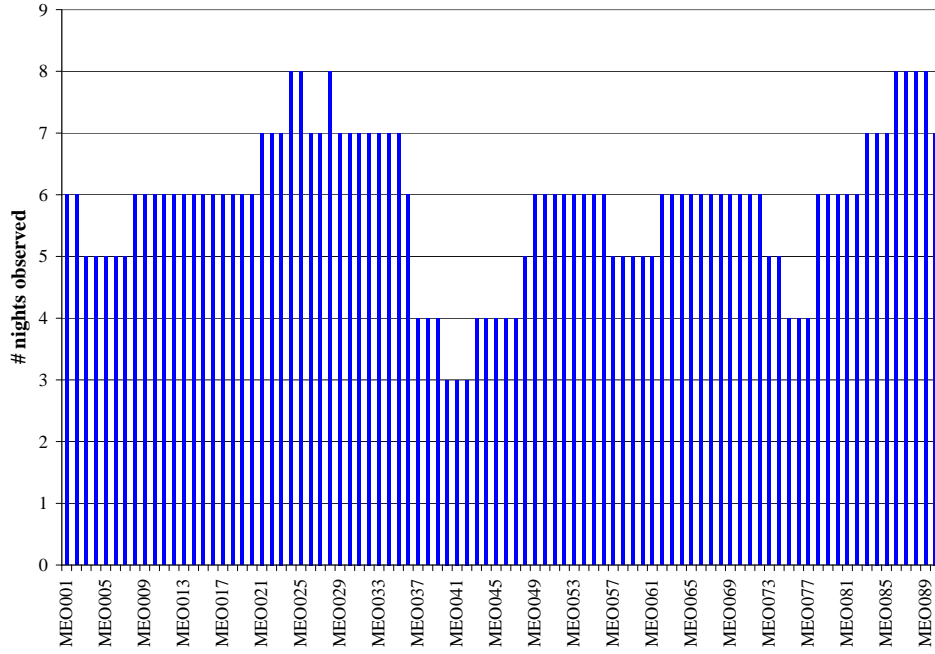
(a) Number of observed nights per pseudo-object
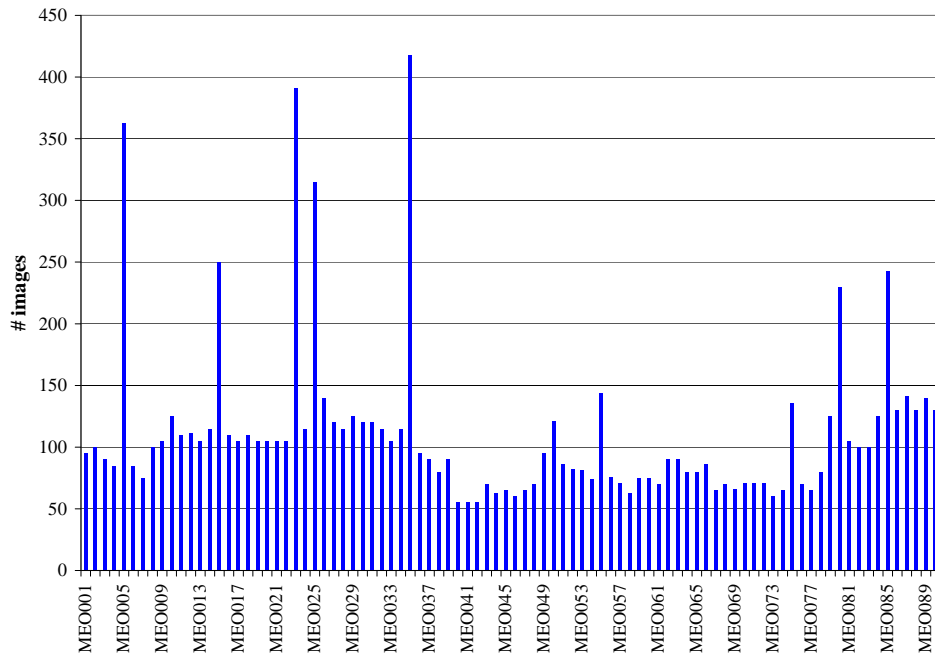
(b) Number of observed images per pseudo-object

Figure 2.11: Distribution of observed nights and images in the orbital plane of 05051A

2.3.7.2   GLONASS orbital Plane 2

In this plane the base object was chosen to be COSMOS 2466 (10041A), a satellite commissioned on October 12th, 2010. The orbital plane was observed irregularly in 10 nights between May 16 and July 4, 2011.

The distribution of nights, where each pseudo-object field was observed, is again not equally distributed, some pseudo-objects were only observed in one night, while others were observed in up to six nights (see Fig. 2.12(a)). The number of observed images also varies from 10 to 70 images in total. This is due to the full automatic observation, where no information is provided which fields were observed in preceding nights and which were not. Then, especially in short summer nights and nights with changing weather conditions, it is very likely that only a small number of fields are observed instead of all scheduled ones.

The Pearson correlation coefficient was about 0.838, which is more than twice as much as for the GIOVE−A orbital plane. As one can see, in routine operation the number of images and nights are well correlated.

Around this orbital plane, there were 32 catalogue objects which could have been detected, 24 of them with circular orbits and the other eight objects with highly eccentric orbits. Within the observation period, two of the objects with highly eccentric orbits could be observed and 17 objects with circular orbits.

The 13 objects, which could not be detected, consist 6 objects with highly eccentric orbits and much different orbital periods. A detection would have happened only by chance. The other seven objects have orbits with inclinations and RAAN close to the base object, therefore they are real "no-shows".

Apart from catalogued objects, 16 tracklets could be extracted, which could not be connected to each other and remained single. Six different fields contained tracklets of objects with orbits within the limits given above around the oribtal plane of the base object, as determined by a determination of a circular orbit. These tracklets could not be associated to catalogued objects. All 90 fields of this orbital plane could be observed and in this case, it was $n = 90$ and $k = 6$. The limits were $\mathcal{N}_l = 5.6568 \approx 6$ and $\mathcal{N}_u = 6.6365 \approx 7$, respectively.
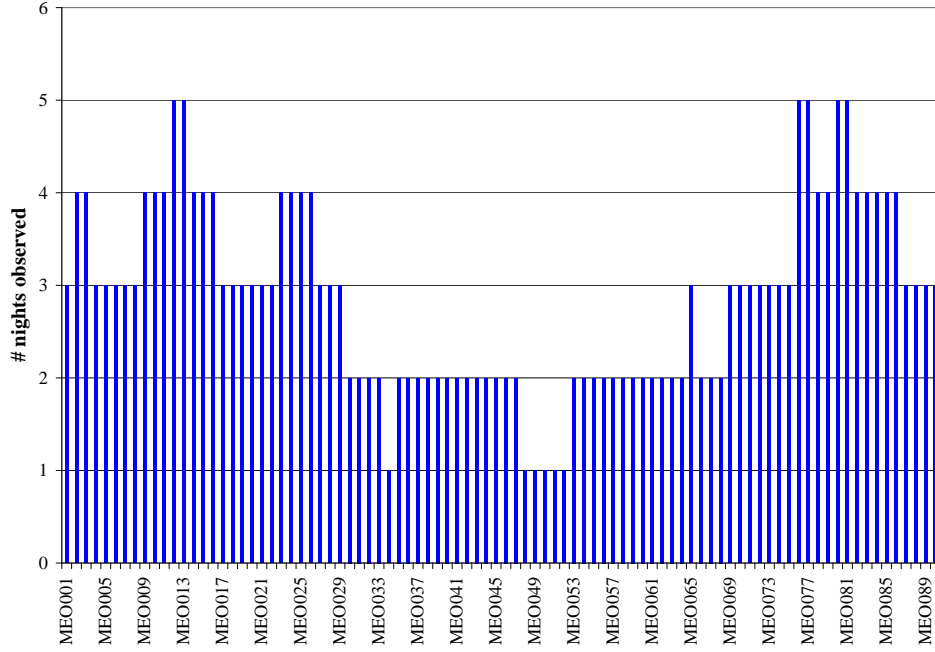
(a) Number of observed nights per pseudo-object
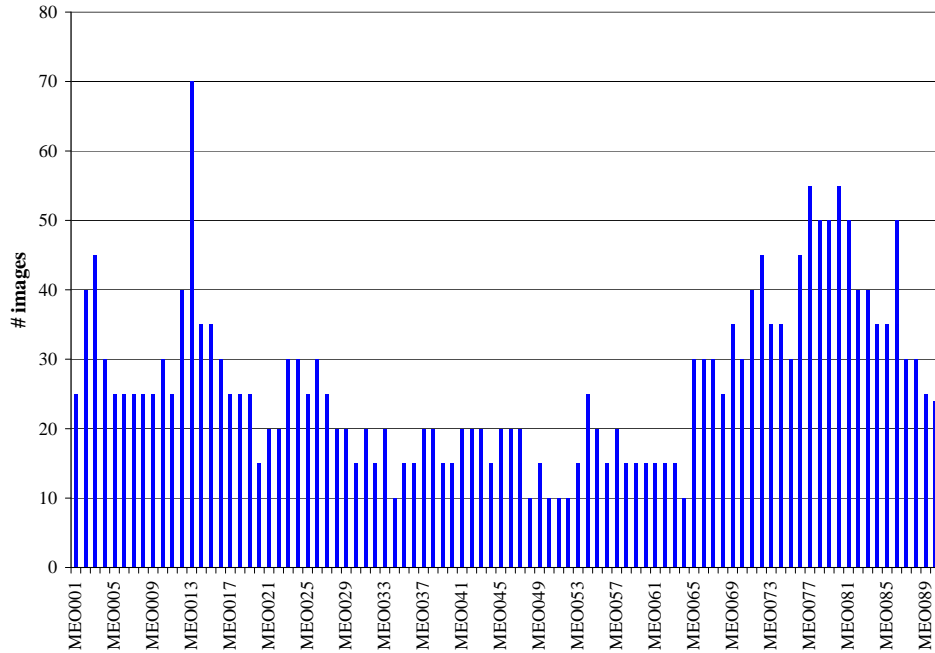
(b) Number of observed images per pseudo-object

Figure 2.12: Distribution of observed nights and images in the orbital plane of 10041A

2.3.7.3   GLONASS orbital Plane 1

For the investigation of this orbital plane the base object was chosen to be COSMOS 2442 (08046A). Observations were performed between August 9 and September 2, 2011.

The correlation coefficient between the number of nights and images is smaller for this orbital plane, 0.771, but still in the same order of magnitude as the other orbital planes.

73 tracklets could not be associated to any catalogued object. Nine of these tracklets could be connected to each other, sometimes from subsequent nights (objects Z11240A to Z11240C in Tab. 2.5); other 64 tracklets remained single. Table 2.5 shows these three objects of the AIUB internal ZimSMART catalogue with their number of tracklets, the associated catalogue object and the reason why the filtering method failed at first.

Table 2.5: MEO objects of the AIUB internal ZimSMART catalogue from surveys of the COSMOS 2442 orbital plane in the observation period between 9/8/2011 and 2/9/2011

Object	Number of tracklets	Corresponding catalogue object	Reason why not correlated
Z11240A	3	COSMOS 2417 (05050C)	too many candidates
Z11240C	2	COSMOS 2418 (05050B)	too many candidates
Z11240D	4	COSMOS 2459 (10007A)	too many candidates

The orbital planes of the objects presented in Tab. 2.5 are not parallel to the orbital plane of the base object, the inclination is within the limits presented in Section 2.3.5, but the RAAN differs from the orbital plane of the base object by around 10°. Therefore they are not taken into account for those objects near the orbital plane of the base object. The were observed by chance when they crossed the orbital plane of the base object.

There were 50 objects with orbits within the limits, including the base object. Of all objects, 43 of them had circular orbits and seven had highly eccentric orbits. During the observation period, 34 of the objects with circular orbits were detected, including the base object, but none of those in highly eccentric orbits. Additionally to the seven object on highly eccentric orbits, nine objects on circular orbits are not detected. The orbital elements of five of them differed too much, but the other four are "no-shows".

The 64 single tracklets remained unassociated. 28 fields contained observations of MEO objects, based on a simple orbit determination, which were nine different fields and according to the Eq. (2.14a) and (2.14b) it was $n = 90$ and $k = 9$, which led then to $\mathcal{N}_l = 8.6462 \approx 9$ and $\mathcal{N}_u = 9.6230 \approx 10$.
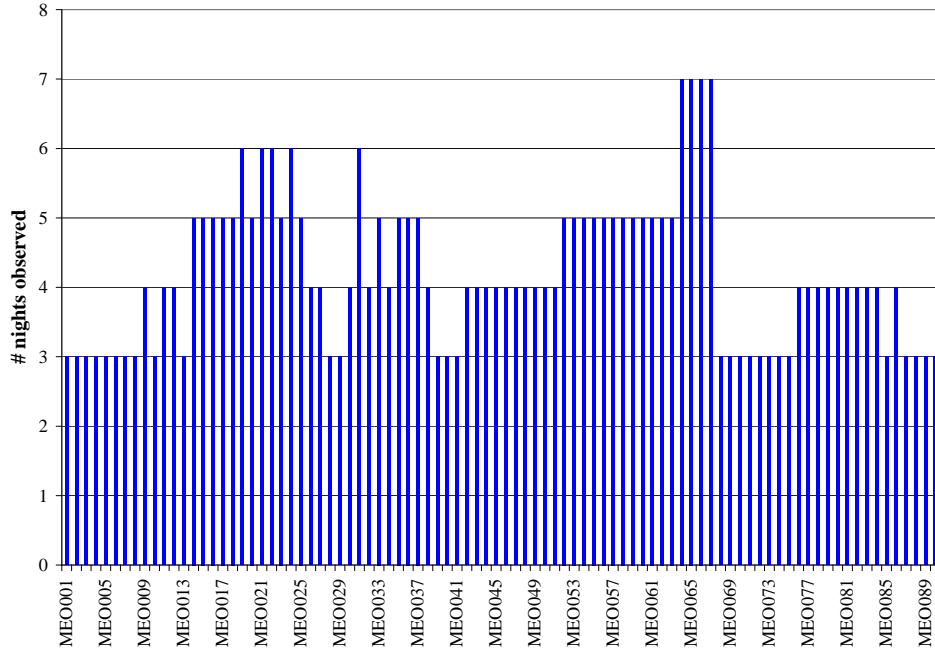
(a) Number of observed nights per pseudo-object
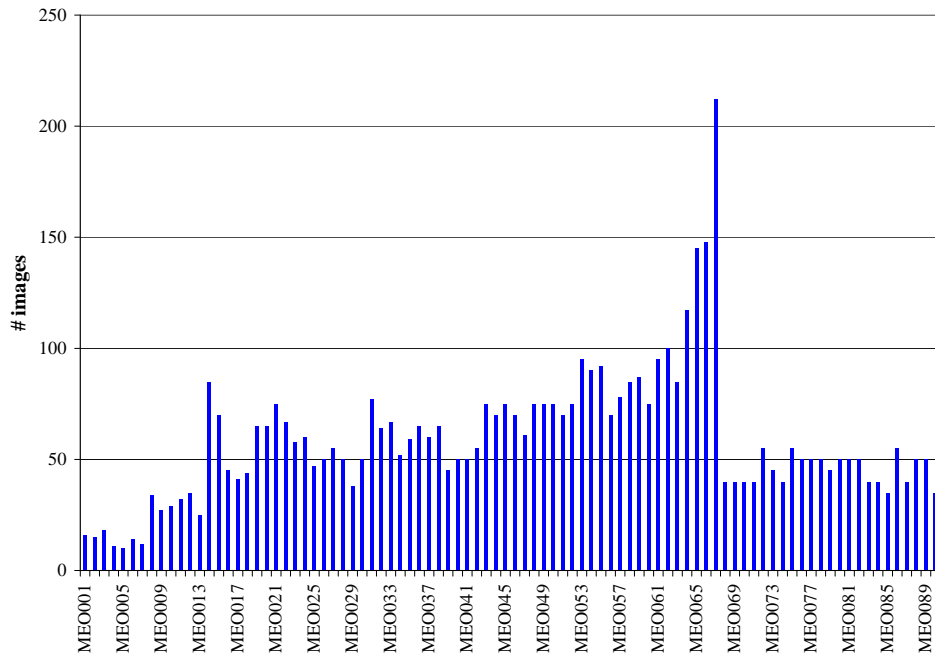
(b) Number of observed images per pseudo-object

Figure 2.13: Distribution of observed nights and images in the orbital plane of 08046A

2.3.7.4   NAVSTAR GPS orbital Plane E

In this plane, the base object was chosen to be NAVSTAR 22 (USA 66, 90103A). There were 8 nights with observations, between September 9 and October 11, 2011.

The coverage of the orbit is not complete, because the study of this plane was aborted to start a second test plane. Afterwards it was not continued in favour of a new NAVSTAR GPS orbital plane. So, this plane still has to be investigated further for completion.

The Pearson correlation coefficient is about 0.873 and a little higher than for the other orbital planes.

Near the orbital plane there were four objects in circular orbits, including the base object. One object was not visible the entire observation period, but also the others were not observed. The RAAN of three objects differed very much, which might be a reason not to be detected, but the base object is a "no-show". A possible reason is that the elements were not updated recently and the observed orbital plane did not represent the true orbital plane of the base object.

Apart from the observations of catalogued objects there were 10 tracklets left over, which could not be associated to another tracklet and remained single. These tracklets belong to two different fields. For the Eq. (2.14a) and (2.14b) the number of analysed fields became $n = 78$ and the number of fields with unassociated tracklets became $k = 2$. The the limits became $\mathcal{N}_l = 1.9331 \approx 2$ and $\mathcal{N}_u = 3.0660 \approx 3$.
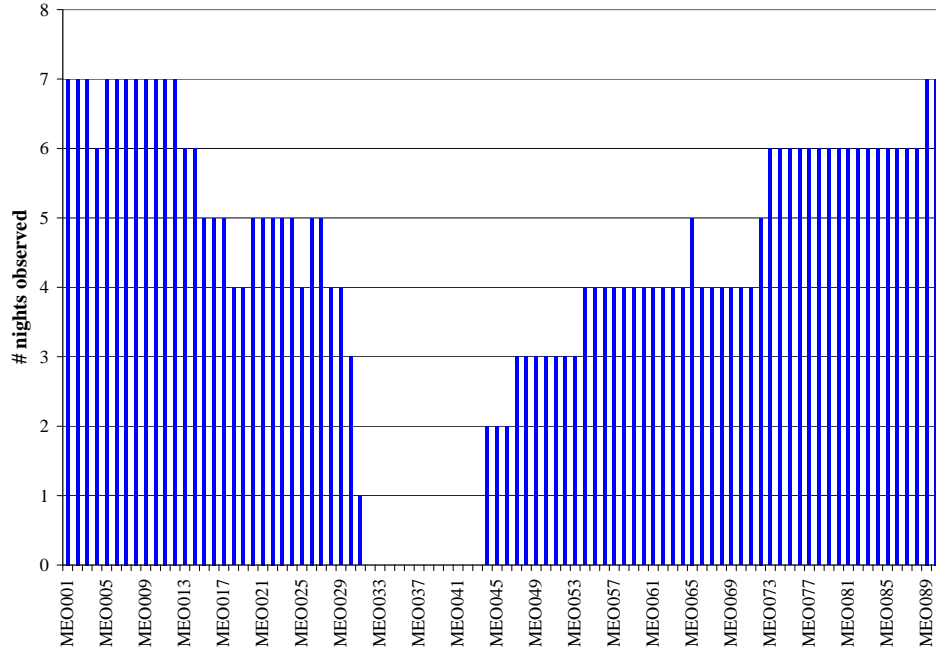
(a) Number of observed nights per pseudo-object
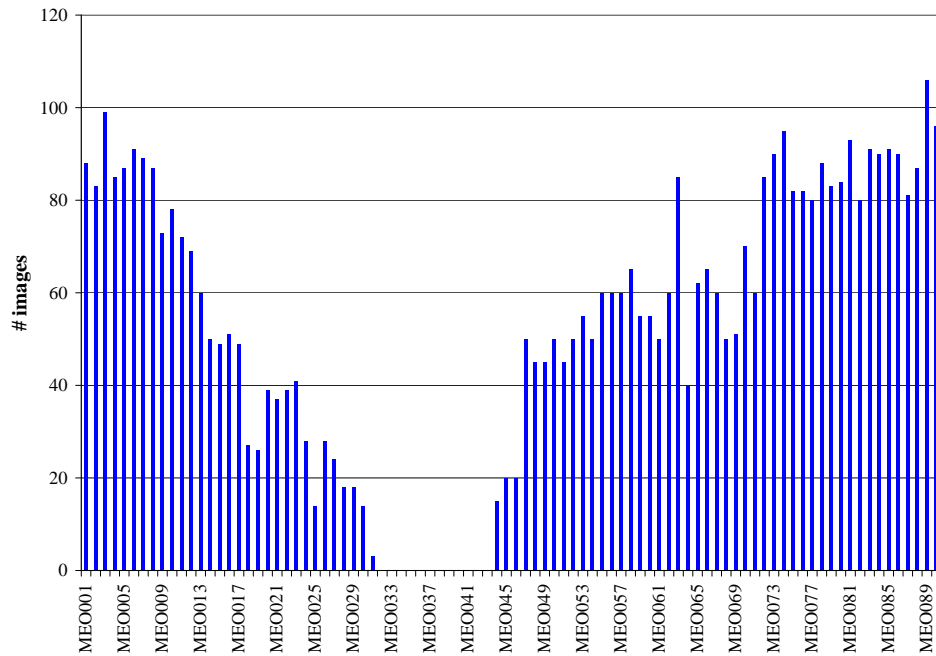
(b) Number of observed images per pseudo-object

Figure 2.14: Distribution of observed nights and images in the orbital plane of 90103A

2.3.7.5 MOLNIYA 1-93 orbital Plane

The investigation of the first NAVSTAR GPS orbital plane was followed by a second test plane. I chose MOLNIYA $1-93$ (04005A). The orbits of the Molniya satellites are optimised to cover the region around the North pole. Geostationary satellites are not visible at geographic latitudes higher than approximately $82°$ and the Molniya satellites solve this problem as they have high eccentric orbits with high inclinations. Their apogee is above the northern hemisphere, so they stay a long time at high altitudes above the Northern polar region.

The angular velocities vary in a large interval, so the circular approximation presented in Tab. 2.1 is not sufficient anymore and Eq. (2.8) must be applied. MOLNIYA $1-93$ had a mean motion n of $2.006\,143\,45\,\mathrm{d}^{-1}$ and an eccentricity of $0.688\,231\,9$ at the observation epochs. This leads to an apparent angular velocity in the perigee of about $209.565°\,\mathrm{h}^{-1}$. At apogee the apparent angular velocity becomes approximately $7.660°\,\mathrm{h}^{-1}$. Tests showed that these velocities are still within the technical limits of ZimSMART.

The surveys were not optimised for complete coverage but proof of concept of being able to gain observations at all. Therefore the observation period was short, with six nights between October 15 and October 22, 2011.

Even though several fields were not observed the correlation coefficient is about 0.804. This means that images of the pseudo-object fields were taken according to the nights they were observed.

Within the limits around the orbital plane of the base objects there were seven catalogue objects to observe, including the base object. All objects have highly eccentric objects. The base object was only visible a short time at the beginning of each night, so it was not observed. Within the observation period, only one object was observed. This object was the only one which was long enough visible each night to acquire observations. Therefore, no object is a "no-show".

Within this period there were 10 tracklets, which could not be associated to any catalogued object. Also, they could not be connected to any other tracklet and remained single. Three of these tracklets were from MEO objects based on a simple orbit determination and were found in three different fields. To calculate the limits, the parameters became $n = 80$ and $k = 3$ and finally $\mathcal{N}_l = 3.0017 \approx 3$ and $\mathcal{N}_u = 4.1067 \approx 4$.
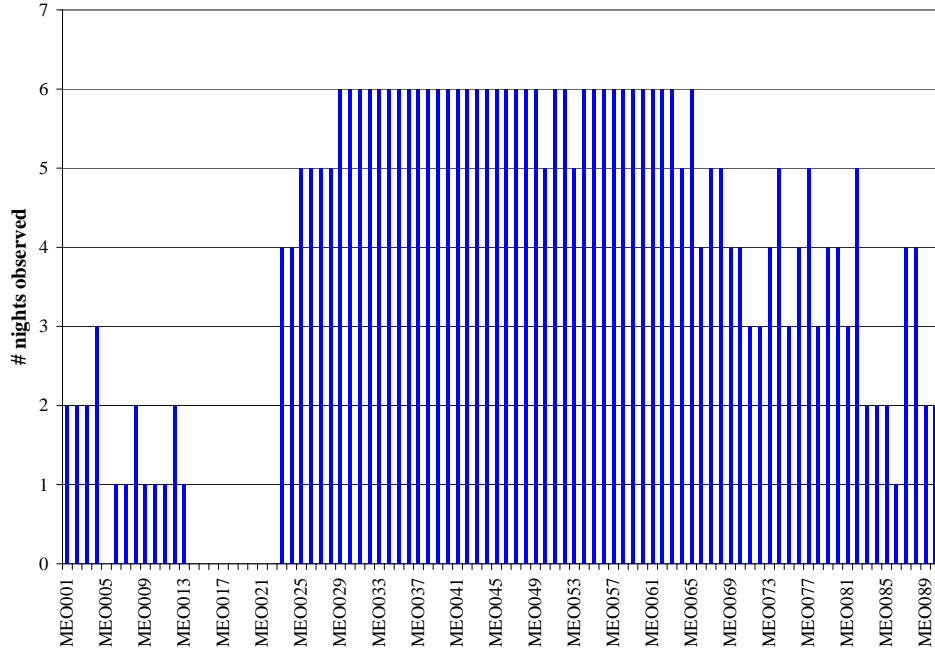
(a) Number of observed nights per pseudo-object
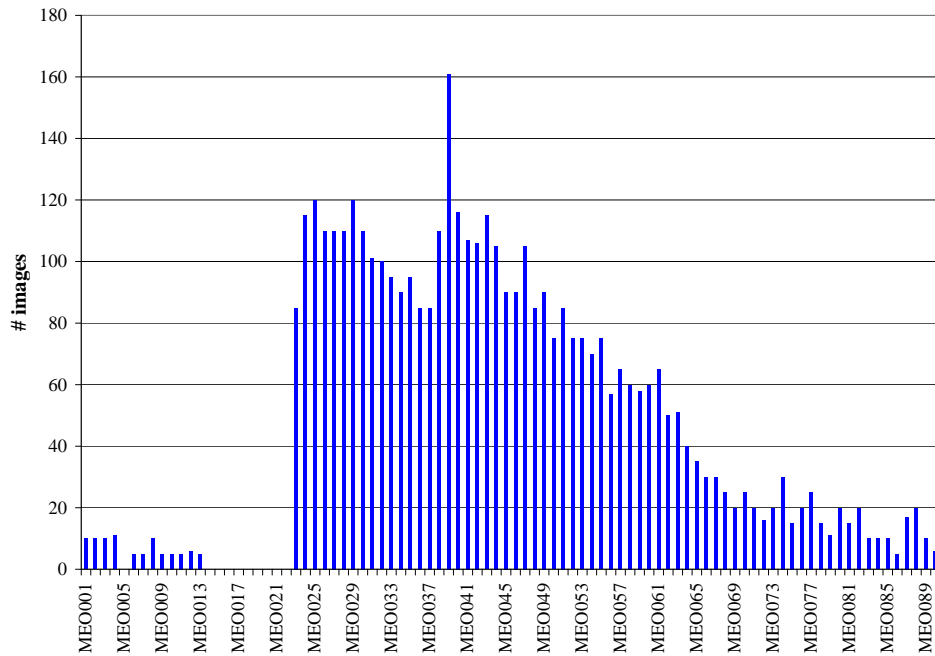
(b) Number of observed images per pseudo-object

Figure 2.15: Distribution of observed nights and images in the orbital plane of 04005A

2.3.7.6 NAVSTAR GPS orbital Plane D

In this plane the base object was chosen to be NAVSTAR 23 (USA 71, 91047A). This orbital plane was observed between October 28th to November 20th, 2011. By chance, during the observation period this satellite was decommissioned on November 4th.

The correlation coefficient between the observed nights and images is about 0.859, which is comparable to the other NAVSTAR GPS orbital plane.

Within the limits around the orbital plane of the base object there were six catalogue objects, including the base object. All of them had circular orbits. Only one could be detected during the observation period, although the determined visibilities should have been sufficient. Again, the used elements might not have been updated recently and the true orbital were not identical to the determined ones.

Apart from the detected object, there were 41 tracklets, which could not be associated to any catalogued objects. Four of these tracklets from to subsequent nights could be connected to each other and stored into the catalogue as a preliminary undetected object. This object was stored into the AIUB internal ZimSMART catalogue as a newly detected object. Furthermore, it was taken into the observation plans of the telescopes ZIMLAT and ESASDT. As of December 3, 2011 it could be observed twice with ZIM-LAT (on November 16 and 17, 2011) and once with ESASDT (on November 28, 2011). Due to these observations it stayed in the plan of regular observations with ZIMLAT for a start.

Later, it had to be concluded that the new object was identical to 91047A. The first determined orbits suggested it might be a different object, but with more observations both orbits appeared to be identical. Therefore it was not a "no-show". The RAAN of the other four unobserved objects differed too much to ensure detections.

The other 37 tracklets remained single and nine of them contained tracklets of MEO objects, based on a simple orbit determination. These tracklets were found on three different fields. The parameters of total observed fields n and fields with unassociated tracklets k, respectively, for the estimation of the limits became $n = 59$ and $k = 3$. The limits themselves were $\mathcal{N}_l = 4.0640 \approx 4$ and $\mathcal{N}_u = 5.5602 \approx 6$. Due to the small number of observed fields, one can expect to find more objects in the other fields.
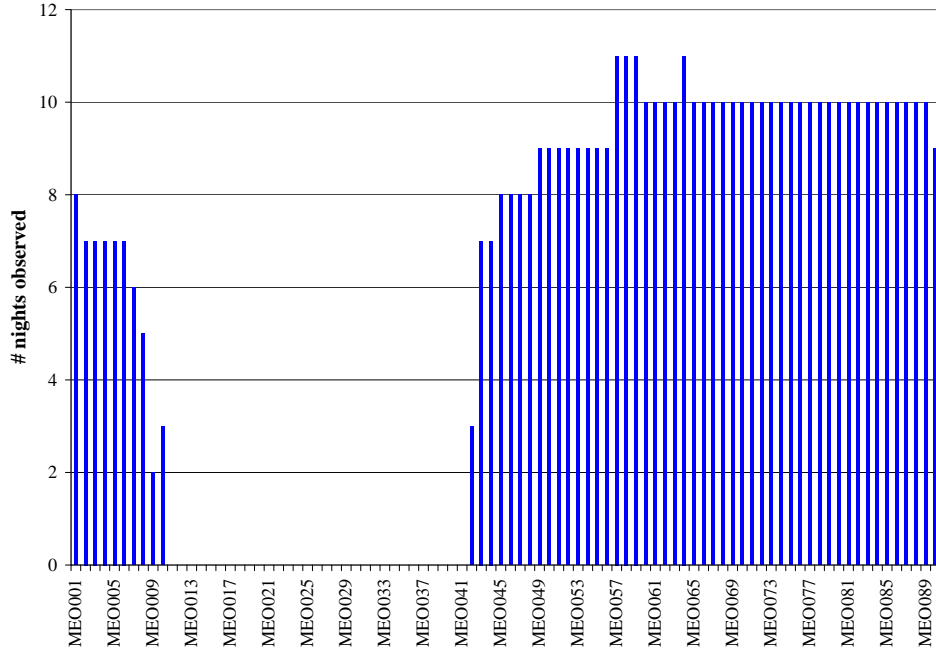
(a) Number of observed nights per pseudo-object
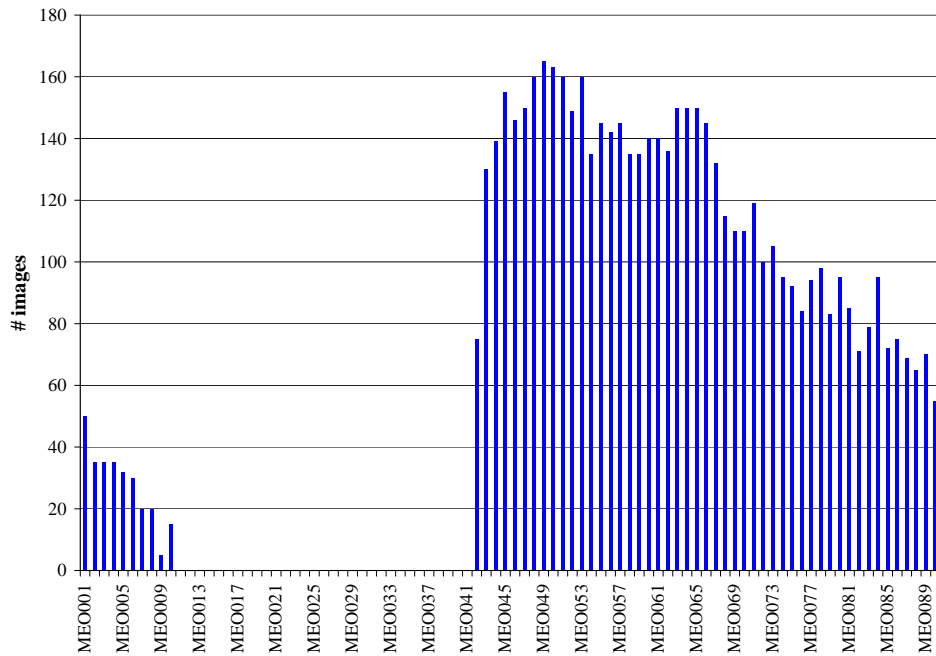
(b) Number of observed images per pseudo-object

Figure 2.16: Distribution of observed nights and images in the orbital plane of 91047A

2.4   Concluding Remarks

In this chapter survey scenarios for the geostationary ring and the Medium Earth Orbit region were presented. For the GEO surveys, declination stripes at fixed right ascension were defined. I could conclude that a scenario with two pairs of stripes is optimal to cover completely the part of the geostationary ring, which is visible from Zimmerwald. Other scenarios, like one stripe or one pair of stripes, were also discussed. With two pairs of stripes, one can ensure that at least one pair is visible, no matter if one pair rises during the night or the other one sets.

A complete coverage of the geostationary ring can be achieved when in several subsequent nights observations could be performed. I could conclude that an interval of one week is sufficient for a complete coverage. With two pairs of stripes the objects are detected up to four times a night as they can cross each stripe.

In addition, the search for space debris was expanded to the MEO region. This region is mostly populated with satellites of Global Navigation Satellite Systems and has not been investigated with telescopes in Zimmerwald before.

A scenario was developed where the orbital plane of an GNSS satellite was observed completely. It was split up into fields with pseudo-objects defined in their centre with a distance of the FoV of ZimSMART ($\approx 4°$) between them along the orbit. Each field around the pseudo-object was observed several times and then the orbital plane was changed. According to this method, the orbital planes of GIOVE−A and MOLNIYA 1 − 93 were investigated to test the scenario on circular and elliptical orbits, respectively. In the routine operation, two orbital planes of GLONASS and two of NAVSTAR GPS were investigated. Several objects, which were supposed to be in or near the orbital planes of the base objects, were not detected.

In the future the other NAVSTAR GPS orbital planes may be investigated as well as the unobserved fields of the already investigated planes.

Chapter 3

Object Identification and Catalogue Built-up

> It is not necessary for the public to know whether I am joking or whether I am serious, just as it is not necessary for me to know it myself.
>
> Salvador Dalí

In contrary to tasked follow-up observations, where the observed object is known, in surveys, no a priori information on the objects is available. A survey is a search for unknown objects in a specific orbital region. Often, several object images are on one frame, especially, when a large FoV is used. In this case, it is more efficient to separate the extraction of tracklets from the identification. The object identification is then a process to relate the observations in a tracklet to an object in an object catalogue. Therefore, the processing pipeline *ZimPipe* was installed.

In *ZimPipe* the object identification process is split up into several steps, where in each step the number of tracklets left to analyse is decreased in the ideal case. Firstly, the tracklets of one night are correlated with several catalogues by comparing the observed positions and velocities with ephemerides, determined from catalogue elements. I use three different catalogues: the catalogue of objects found with ZimSMART (called AIUB internal ZimSMART catalogue), GEO objects in the USSTRATCOM catalogue and then the combination of the USSTRATCOM and the AIUB internal catalogue.

A certain fraction of tracklets will be left over for some reason, e. g. because an uncatalogued object was discovered. Those leftover tracklets are checked pairwise whether or not some of them belong to the same object. This test is done by means of a first orbit determination. Finding matching tracklets reduces the amount of comparisons in the following steps and avoids the possibility of associations of several individual tracklets to one object. Tracklets, for which at least one other matching tracklet could be found, are called "object candidates", the others remain single.

The object candidates run through an additional filtering step by investigating their orbital elements. Two representations of elements are investigated: the classical Keplerian elements and the synchronous elements defined by E. M. Soop (e. g. presented in [Soop 94]).

Finally, each possible correlation has to be confirmed by an orbit determination. In case of the ZimSMART processing pipeline orbit determinations are performed with the *CelMech* routines *ORBDET* and *SATORB*.

Chapter 3. Object Identification and Catalogue Built-up

3.1 Theoretical Background

3.1.1 The Equation of Motion

To determine an orbit from observations or simulations, the equation of motion has to be solved:

$$\ddot{\vec{r}} = -\vec{\nabla} V_\oplus(\vec{r}) - \vec{\nabla} V_\odot(\vec{r}) - \vec{\nabla} V_\mathbb{C}(\vec{r}) + \vec{a}_{\mathrm{ng}}. \tag{3.1}$$

In this equation, $\vec{r}$ represents the vector between the Sun and the object and $\ddot{\vec{r}}$ the acceleration to the Sun, consequently. Furthermore, there are the gradient of the gravitational potential of the Earth ($\vec{\nabla} V_\oplus$), the Sun ($\vec{\nabla} V_\odot$) and the Moon ($\vec{\nabla} V_\mathbb{C}$). Any other acceleration is collected in the term of non- gravitational accelerations $\vec{a}_{\mathrm{ng}}$.

In the following paragraphs, the individual summands are presented in detail.

3.1.1.1 Gravitational Potential of the Earth

The gravitational potential of the Earth can be decomposed into spherical harmonics. It may be written as (taken from [Beut 05]):

$$
\begin{aligned}
V_\oplus(\vec{r}) &= V_\oplus(r, \phi, \lambda) \\
&= \frac{GM_\oplus}{r} \sum_{i=0}^{\infty} \left(\frac{R_\oplus}{r}\right)^i \cdot \sum_{k=0}^{i} P_i^k(\sin(\phi)) \left[C_{ik}\cos(k\lambda) + S_{ik}\sin(k\lambda)\right]
\end{aligned} \tag{3.2}
$$

The index i is the degree, k the order of the spherical harmonics. In this equation $R_\oplus$ is the equatorial radius of the Earth, P_i^k the associated Legendre functions and especially P_i^0 the Legendre polynomials:

$$P_i^0(x) = \frac{1}{2^i \cdot i!} \frac{\mathrm{d}^i}{\mathrm{d}x^i}\left[\left(x^2 - 1\right)^i\right]$$

$$P_i^k(x) = \left(1 - x^2\right)^{k/2} \frac{\mathrm{d}^k}{\mathrm{d}x^k} P_i^0(x)$$

For practical reasons, one will take an upper limit of i and k for the calculation of the gravitational potential. In case of the software package *CelMech*, developed by G. Beutler, it is chosen to be $i_{\max} = k_{\max} = 12$ by default, but these values may be changed by the user.

For my reference calculations, presented in Paragraph 3.2.3, I only used the non-vanishing terms with lowest order, $i = k = 0$ and $i = 2$, $k = 0$. All terms with $i = 1$ are vanishing, because the Parameters C_{10}, C_{11} and S_{11} are equal to zero (see again [Beut 05]). When these conditions are applied to Eq. 3.2 and the Legendre polynomial $P_0^2(\sin(\phi))$ is calculated, the simplified model of the gravitational potential becomes:

$$
\begin{aligned}
V_\oplus(\vec{r}) &= \frac{GM_\oplus}{r} + \frac{GM_\oplus}{r} \cdot \left(\frac{R_\oplus}{r}\right)^2 \cdot C_{20} P_2^0(\sin(\phi)) \\
&= \frac{GM_\oplus}{r} + \frac{GM_\oplus R_\oplus^2 C_{20}}{r^3} \cdot \frac{3\sin^2(\phi) - 1}{2}
\end{aligned} \tag{3.3}
$$

That represents a spherical Earth with an equatorial bulge.

In the equation of motion, the gradient of the potential is used:

$$\vec{\nabla} V_{\oplus}\left(\vec{r}\right) = -\left(\frac{GM_{\oplus}R_{\oplus}^2}{r^2} + \frac{3}{2}\frac{GM_{\oplus}R_{\oplus}^2 C_{20}}{r^4}\left(3\sin^2(\phi)-1\right)\right)\cdot\vec{e}_r$$

$$+ \frac{3GM_{\oplus}R_{\oplus}^2 C_{20}}{r^4}\sin(\phi)\cos(\phi)\cdot\vec{e}_\phi$$

$$= -\frac{GM_{\oplus}\vec{r}}{r^3} + \frac{3GM_{\oplus}C_{20}R_{\oplus}^2}{2r^5}\begin{pmatrix} r_1\left(1-5\dfrac{r_3^2}{r^2}\right) \\[2mm] r_2\left(1-5\dfrac{r_3^2}{r^2}\right) \\[2mm] r_3\left(3-5\dfrac{r_3^2}{r^2}\right) \end{pmatrix} \qquad (3.4)$$

The gravitational potential in the latter form is written in Earth-centred space-fixed Cartesian coordinates.

3.1.1.2 Gravitational Potentials of Objects of the Solar System

The Moon and Sun may be considered as point sources and their gravitational potentials may therefore be represented as central potentials. Then, they may be written as:

$$V_j\left(\vec{r}_j, \vec{r}\right) = GM_j \cdot \left(\frac{1}{|\vec{r}-\vec{r}_j|} + \frac{\vec{r}\cdot\vec{r}_j}{r_j^3}\right), \qquad (3.5)$$

with the gradient of the potential

$$\vec{\nabla} V_j\left(\vec{r}_j, \vec{r}\right) = GM_j \cdot \left(\frac{\vec{r}-\vec{r}_j}{|\vec{r}-\vec{r}_j|^3} + \frac{\vec{r}_j}{r_j^3}\right). \qquad (3.6)$$

The index j denotes the Moon or the Sun. The vector $\vec{r}$ represents the direction from the Earth to the object, $\vec{r}_{\mathbb{C}}$ from the Earth to the Moon and $\vec{r}_{\odot}$ from the Earth to the Sun.

Equation (3.5) is not only valid for the Moon or the Sun, but also for the planets of the Solar system. To give an estimation of the perturbations of the other planets, I present the absolute value of the maximum perturbing acceleration of each object in the Solar system. The maximum is achieved, when the object is closest to the Earth. In case of the Sun this is when the Earth is in its perihelion, in case of the Moon it is its perigee. The individual inclinations against the equatorial plane of the Earth are neglected, I assumed the planets and the Sun to be in the equatorial plane of the Earth. I also assumed that the perihelion position of each planet is at the aphelion of the Earth's orbit to achieve the smallest possible distance between the Earth and the other object. The absolute value of the perturbing acceleration with this assumption can be written as:

$$\left|GM_{\mathrm{P}} \cdot \left(\frac{\vec{r}-\vec{r}_{\mathrm{P}}}{|\vec{r}-\vec{r}_{\mathrm{P}}|^3} + \frac{\vec{r}_{\mathrm{P}}}{r_{\mathrm{P}}^3}\right)\right| \approx GM_{\mathrm{P}} \cdot \left(\frac{1}{(r-r_{\mathrm{P}})^2} + \frac{1}{r_{\mathrm{P}}^2}\right), \qquad (3.7)$$

where r is the distance from the object to the Earth, r_{P} from the object to one planet or the Sun and M_{P} is the mass of the planet or the Sun. The calculation is done for a geostationary object on a circular orbit with a radius of $42\,000\,\mathrm{km}$. For objects with smaller radii or semi-major axes, the effect of the gravitational potential of the Earth becomes even more dominant than the perturbing effects of the planets and the Sun. The results are presented in Tab. 3.1. The masses and orbital parameters were taken from [NASAa], the minimum distances were calculated concerning the assumption above and the perturbations were determined with Eq. (3.7).

Table 3.1: Maximum perturbation of the Sun, Moon and planets of the Solar system

Object	Mass (kg)	Minimum distance from the Earth (AU)	Minimum distance from a GEO object (AU)	Maximum contribution to $\ddot{\vec{r}}$ (m s^{-2})
Earth	5.9736×10^{24}		0.0003	2.2601×10^{-1}
Sun	1.9891×10^{30}	0.9834	0.9831	1.2283×10^{-2}
Moon	7.3490×10^{22}	0.0024	0.0021	1.1419×10^{-4}
Jupiter	1.8986×10^{27}	3.9347	3.9344	7.3187×10^{-7}
Venus	4.8685×10^{24}	0.2554	0.2551	4.4682×10^{-7}
Saturn	5.6846×10^{26}	7.9930	7.9927	5.3095×10^{-8}
Mars	6.4185×10^{23}	0.3724	0.3721	2.7678×10^{-8}
Mercury	3.3020×10^{23}	0.5168	0.5165	7.3888×10^{-9}
Uranus	8.6832×10^{25}	17.2624	17.2621	1.7387×10^{-9}
Neptune	1.0243×10^{26}	28.7889	28.7887	7.3743×10^{-10}

As one can see, the maximum perturbation of the Earth compared to the Sun and Moon is approximately 2000:100:1, and of Jupiter it is even more than two orders of magnitude less. Thus, it can be justified to use only the gravitational potential of the Earth, Sun and Moon, and not to take those of the other planets into account to estimate the evolution of the orbital elements. Nevertheless, the tool *CelMech* includes all of them to achieve a higher accuracy.

3.1.1.3 Non-gravitational Forces

All other, non-gravitational forces are collected into $\vec{a}_{ng}$. For example, decelerating forces of the atmosphere of the Earth will contribute to $\vec{a}_{ng}$ for objects with low perigees, e.g. highly eccentric orbits or Low Earth Orbits (LEO). Other possible sources of non-gravitational forces are relativistic effects or the Solar radiation pressure, as described below.

The Solar Radiation Pressure

Photons coming from the Sun transfer energy and momentum to an illuminated object because of the conservation laws of energy and momentum, respectively.

The Solar radiation pressure (also called direct radiation pressure, DRP) results in an acceleration in the direction of the pressure, the direction Sun $\rightarrow$ object (taken from [Beut 05] and shown in Fig. 3.2(b)):

$$\vec{a}_{DRP} = D(t) \cdot \vec{e}_D$$
$$= \frac{C}{2} \frac{S}{c} \frac{A}{m} \frac{(1\,\text{AU})^2}{\left|\vec{r} - \vec{r}_{\odot}\right|^2} \frac{\vec{r} - \vec{r}_{\odot}}{\left|\vec{r} - \vec{r}_{\odot}\right|} \tag{3.8}$$

The value C represents the reflective properties of the satellite surface and is set to $C = 2$ by default, which stands for full absorption. This value can only be an assumption as the true reflective properties are unknown.

The vector $\vec{r}$ is the geocentric position vector of the object and $\vec{r}_{\odot}$ the geocentric position vector of the Sun. The vector $\vec{r} - \vec{r}_{\odot}$ is consequently the vector from the Sun to the object. The fraction S/c is the solar constant at a distance of 1 AU ($I_0 = 1360.8(5)\,\text{W m}^{-2}$, taken from [Kopp 11]) divided by the speed of light. Within $SATORB$ not the individual quantities are defined but the fraction is set by default to $4.56 \times 10^{-6}\,\text{W s m}^{-3}$.

The fraction A/m is the area-to-mass ratio (AMR), where A is the surface of the object, which is exposed to the Sun, and m is the total mass of the object. Any deviation from full absorption ($C \neq 2$) is also
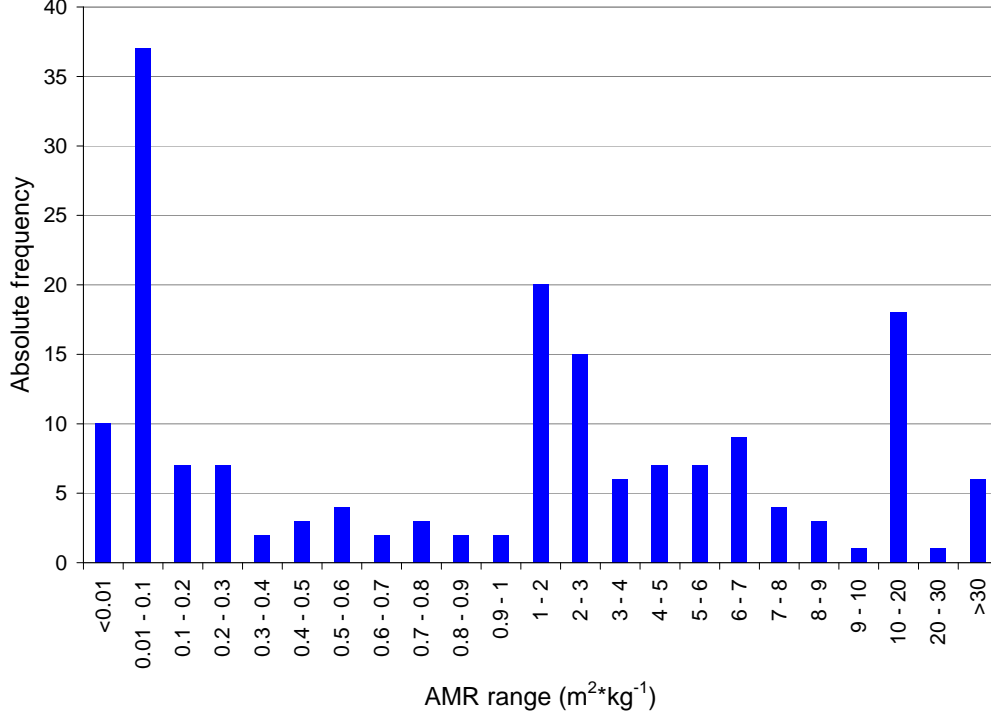
Figure 3.1: Distribution of the AMR values of objects in the AIUB internal catalogue

included, when estimating this parameter. For example, a sheet of standard office paper by ISO 216, which is perpendicular to the Sun, has an AMR of about $10\,\mathrm{m^2\,kg^{-1}}$. Referring to [Beut 05], GPS satellites have an AMR value of about $0.02\,\mathrm{m^2\,kg^{-1}}$. The distribution of AMR values of the object in the current AIUB internal catalogue is very broad, ranging from below $0.01\,\mathrm{m^2\,kg^{-1}}$ to more than $30\,\mathrm{m^2\,kg^{-1}}$, shown by Fig. 3.1.

Empirical Parameters

The Gaussian perturbation equations describe the effects on the Keplerian elements by any perturbation, displayed by the possibly time-dependent vector $\vec{a}_{\mathrm{emp}}(t) = \big(R(t), S(t), W(t)\big)^{T}$. The interpretation of this vector is that it subsumes all non-gravitational forces to a resulting acceleration. It can be written as

$$\vec{a}_{\mathrm{emp}}(t) = R(t) \cdot \vec{e}_R + S(t) \cdot \vec{e}_S + W(t) \cdot \vec{e}_W,$$

with the following definition of the also time-dependent components R, S and W:

- $\big(\vec{e}_R, \vec{e}_S, \vec{e}_W\big)^{T}$ builds a right-handed Cartesian reference frame
- $\vec{e}_R$ is in the direction from the Earth to the object, directing away from the Earth,
- $\vec{e}_S$ is perpendicular to $\vec{e}_R$, but still in the orbital plane, and
- $\vec{e}_W$ is perpendicular to the orbital plane.

To physically model the Solar radiation pressure into account, one can replace the R-component. The decision in favour of the R-component is sensible as during the night the direction of the Solar radiation

pressure is similar to $\vec{e}_R$. The perturbation vector then becomes

$$\begin{aligned}
\vec{a}_{\mathrm{emp}}(t) &= \big(D(t), S(t), W(t)\big)^T \\
&= D(t) \cdot \vec{e}_D + S(t) \cdot \vec{e}_S + W(t) \cdot \vec{e}_W.
\end{aligned}$$

The definition of $D(t) \cdot \vec{e}_D$ is equal to Eq. (3.8). The reference frame is not a Cartesian one anymore because the unit vector $\vec{e}_D$ is not necessarily perpendicular to $\vec{e}_S$ or $\vec{e}_W$, respectively. Additionally, it is possible that the vector $\vec{e}_D$ is parallel to one of the others and the estimation of these parameters will lead to ambiguous results. This happens to a GEO object near the sunrise or sunset and to a MEO object when it rises or sets itself. Furthermore the inclination of the orbit must be as large as the current declination of the Sun. This might be unlikely but cannot be neglected in special cases.

Figure 3.2(a) shows the an example of a circular orbit with the empirical parameters in RSW-decomposition. To demonstrate the direction of vector $\vec{e}_R$ the line between the centre of the Earth and the object is added. The R-component was replaced by the D-component in Fig. 3.2(b), together with the direction to the Sun. The grey arrow represents again the R-component for comparison. In both cases the red dots mark an observed object.

(a) RSW-decomposition   (b) DSW-decomposition
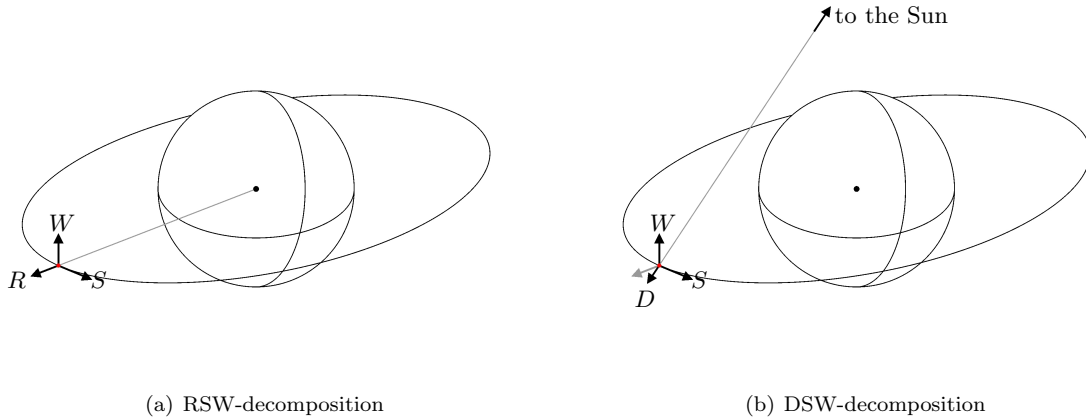
Figure 3.2: Orientation of the empirical parameters

3.1.2 Orbital Elements

To describe an orbital state completely, six orbital elements at a certain epoch (called osculating elements) are one possibility. The form of the elements set is arbitrary, if they are independent of each other.

In this paragraph, I focus on three forms: the Keplerian and the synchronous elements, and finally state vectors. Before that, I introduce the angular momentum vector, which can be used to display the orientation of the orbital plane. The angular momentum vector defines the orientation of the orbital plane with respect to the equatorial plane, i.e. the inclination i and the right ascension of the ascending node (RAAN) Ω can be determined directly.

3.1.2.1 The angular Momentum Vector per Unit Mass

The normal vector of an orbital plane is parallel to its angular momentum vector. The angular momentum vector also defines the orientation of the orbital plane and the evolution of the normal vector can be described with the evolution of the angular momentum vector. The angular momentum is defined as $\vec{L} = m\vec{r} \times \dot{\vec{r}}$. Without perturbations it would be constant, $\vec{L} = \mathrm{const.}$, which represents an orbital plane

with fixed orientation. Since the multiplication of a scalar factor to the angular momentum vector does not change its direction, I divide $\vec{L}$ by m and get the angular momentum vector per unit mass:

$$\vec{l} = \vec{r} \times \dot{\vec{r}}. \tag{3.9}$$

The angles, which defines the orientation are the inclination i and the RAAN Ω.

$$\vec{l} = \begin{pmatrix} l_1 \\ l_2 \\ l_3 \end{pmatrix} = |\vec{l}| \begin{pmatrix} \sin(\Omega)\sin(i) \\ -\cos(\Omega)\sin(i) \\ \cos(i) \end{pmatrix} \tag{3.10}$$

Vice versa, the inclination i and the RAAN Ω can be determined from $\vec{l}$.

3.1.2.2 Keplerian Elements

The Keplerian elements are the most common form to display orbital elements. They can consist of the semi-major axis a, eccentricity ε, inclination i, RAAN Ω, argument of perigee ω and the mean anomaly M. The latter value can also be replaced by the epoch of the passage through the perigee T_Π or the time interval between the passage and the epoch of the orbit determination ΔT_Π.

Semi-major Axis
By definition, the semi-major axis a of an object is the average distance to the centre of mass. The equivalent of a circular orbit is the radius.

Via the 3rd Kepler's law of planetary motion, the semi-major axis is directly connected to the orbital period (see again 1.1):

$$T^2 = \frac{4\pi^2}{G\left(M_{\oplus} + m\right)} \cdot a^3.$$

Eccentricity
The eccentricity ε is a measure of the deviation of the orbit from a circle. By definition, an eccentricity equal to zero represents a circle, values between greater than zero and smaller than one stand for ellipses. Satellites and space debris objects orbiting around the will have eccentricities smaller than one. An eccentricity equal to one represents a parabolic orbit, while with larger values an orbit becomes hyperbolic. The parabolic and hyperbolic cases are not relevant for an orbit determination of space debris object and only mentioned for completeness.

The limit $\varepsilon = 1$ separates the bound systems from the unbound ones.

Inclination
The inclination i describes the angle between the orbital plane and the equatorial plane. It can be derived directly from the angular momentum vector with Eq. (3.10):

$$\frac{l_3}{|\vec{l}|} = \cos(i)$$

$$\Rightarrow \qquad i = \arccos\left(\frac{l_3}{|\vec{l}|}\right) \tag{3.11}$$

Right Ascension of the ascending Node

At the RAAN Ω, the orbit of an object crosses the equatorial plane in Northern direction. The angle is measured in the equatorial plane from the vernal point. It can be determined using the angular momentum vector (3.10):

$$\frac{l_1}{l_2} = \frac{\sin(\Omega)\sin(i)}{-\cos(\Omega)\sin(i)} \tag{3.12}$$

$$\Rightarrow \qquad \Omega = \arctan\left(\frac{l_1}{-l_2}\right) \tag{3.13}$$

Equation (3.13) is only valid if $i > 0$. For $i \to 0$, $\sin(i) \to 0$ and the numerator as well as the denominator in Eq. (3.12) go to zero. For $i = 0$ the RAAN is not defined, because the orbital plane and the equatorial plane are identical. In this case, the RAAN can be set to a default value (e.g. to the vernal point, $0°$) to ensure six parameters.

Argument of Perigee

The argument of perigee ω is the position of the perigee of the orbit and is the angle between the RAAN and the perigee, measured from the central object. In case of a perfectly circular orbit, the perigee is not defined. To get six parameters, this parameter can be set to a default value (e.g. to the RAAN, $0°$).

Mean Anomaly

The mean anomaly M is an auxiliary quantity for the position of an object on its orbit at the reference epoch. An auxiliary pseudo-object is assumed to be on a circular orbit with the same semi-major axis like the object's orbit, therefore its angular velocity is constant and the orbital period is equal to the object's period. The object and the pseudo-object, both passed the perigee of the object at the same time, then the mean anomaly is the angle between the perigee and the current position of the pseudo-object, measured from the centre of the ellipse.

The corresponding angle of the object is the eccentric anomaly E, which can be calculated from the mean anomaly via Kepler's equation:

$$M = E - \varepsilon\sin(E)$$

Compared to Eq. (2.2), one gets the connection between the mean anomaly and the epoch of the passage through the perigee T_Π and the time interval since the passage ΔT_Π, respectively:

$$M = 2\pi \cdot n \, (t - T_\Pi)$$
$$= 2\pi \cdot n \cdot \Delta T_\Pi$$

The mean motion n can be derived from the 3rd Kepler's law of planetary motion. The mean anomaly is growing linear with time, because the orbit of the pseudo-object is circular. The conversion into the eccentric anomaly has to be performed with iterative procedures.

There are other quantities, which can also be used. These are e.g. the true anomaly T and the argument of latitude u. The true anomaly is the angle between the position of the object on its orbits and its perigee and is connected to the eccentric anomaly E via the following equation:

$$\tan\left(\frac{T}{2}\right) = \sqrt{\frac{1+\varepsilon}{1-\varepsilon}}\cos\left(\frac{E}{2}\right)$$

The argument of latitude is the angle between the position of the object on its orbit and its RAAN. It is therefore the sum of the argument of perigee and the true anomaly:

$$u = \omega + T \tag{3.14}$$

The true anomaly and the argument of latitude, both take the true motion of the object into account, unlike the mean anomaly, which only refers to the average motion.

3.1.2.3 Synchronous Elements

With the Keplerian elements there occur some problems if the eccentricity is close to zero and the inclination is close to $0°$. In the first case the argument of the perigee is not defined, in the latter the RAAN is not defined. That makes it impossible do define a Keplerian orbit and to determine accurate positions of an object.

Therefore, one can define equivalent parameters, where such singularities do not occur at all or only for those parameter constellations, which are already captured by the Keplerian elements.

Anyway, every equivalent set of elements must consist of six parameters at an epoch, only then the set is distinct and all sets can be converted into each other.

I decided on the synchronous elements presented by E. M. Soop (see [Soop 94]). They consist of a two-dimensional eccentricity vector $(\varepsilon_x, \varepsilon_y)$, a two-dimensional inclination vector (i_x, i_y), the mean longitude drift rate D and the mean longitude at epoch λ_0, described below in detail.

Inclination Vector
The unit vector of the angular momentum vector in Eq. (3.10) is also called three-dimensional inclination vector $\vec{I}$. Its projection on the on the equatorial plane is then called two-dimensional inclination vector.

$$\vec{I} = \begin{pmatrix} \sin(\Omega)\sin(i) \\ -\cos(\Omega)\sin(i) \\ \cos(i) \end{pmatrix}$$

$$\Rightarrow \qquad \begin{pmatrix} i_x \\ i_y \end{pmatrix} = \begin{pmatrix} \sin(\Omega)\sin(i) \\ -\cos(\Omega)\sin(i) \end{pmatrix}$$

Because the synchronous elements are used in cases of small inclinations, I can apply the approximation for small angles to $\sin(i)$: $\sin(i) \approx i$. For inclinations smaller than $4.4°$ the error of this approximation is below $0.1\,\%$ (cf. [Bron 01]). Then, the two-dimensional inclination vector becomes:

$$\Rightarrow \qquad \begin{pmatrix} i_x \\ i_y \end{pmatrix} = \begin{pmatrix} i \cdot \sin(\Omega) \\ -i \cdot \cos(\Omega) \end{pmatrix} \tag{3.15}$$

The geometrical interpretation of the vector is that it represents the projection of the orbital pole onto the equatorial plane.

Eccentricity Vector
In the same manner an eccentricity vector can be defined:

$$\begin{pmatrix} \varepsilon_x \\ \varepsilon_y \end{pmatrix} = \begin{pmatrix} \varepsilon \cdot \cos(\Omega + \omega) \\ \varepsilon \cdot \sin(\Omega + \omega) \end{pmatrix} \tag{3.16}$$

This vector represents the direction to the perigee of the orbit. But one has to be aware that the angle $\Omega + \omega$ only make sense if i is close to $0°$, because Ω is measured in the equatorial plane and ω in the orbital plane. Only if these two planes are approximately identical, the sum can be used to represent the physical orbit.

Mean Longitude Drift Rate

The deviation between the rotation of the Earth and the orbital period of an object can be expressed in the mean longitude drift rate D (taken from [Soop 94]):

$$D = -1.5 \cdot \frac{a - 42\,164.1716\,\mathrm{km}}{42\,164.1716\,\mathrm{km}}$$

To get the mean longitude drift rate in units of degree per day, this equation has to be multiplied by $360.9856°\,\mathrm{d}^{-1}$. Objects with an semi-major axis greater than $42\,164.1716\,\mathrm{km}$ will drift westward ($D < 0°\,\mathrm{d}^{-1}$), semi-major axes below $42\,164.1716\,\mathrm{km}$ will cause a drift eastward ($D > 0°\,\mathrm{d}^{-1}$).

For objects of the geostationary ring the drift rate is very small, with semi-major axes $41\,964\,\mathrm{km} \leq a \leq 42\,364\,\mathrm{km}$ one gets drift rates of $2.571°\,\mathrm{d}^{-1} \geq D \geq -2.566°\,\mathrm{d}^{-1}$.

Mean Longitude at Epoch

The mean longitude at epoch λ_0 represents the geographical longitude of the Earth, above which an object appears at the corresponding epoch.

$$\lambda_0 = (1 + D) \cdot s_0 - s_G - D \cdot (\Omega + \omega) \tag{3.17}$$

In this formula there are another two parameters, the sidereal angle of the object s_0 and and the sidereal angle of the Greenwich longitude s_G. The sidereal angle is measured in the equatorial plane from the vernal equinox to λ_0. The sidereal angle of the Greenwich longitude is also called sidereal time.

$$s_G = 100.4606° + 360.985\,647\,3°\,\mathrm{d}^{-1} \cdot (t_0 - 51544.5) \tag{3.18}$$

This linear approximation can be found in [Mont 00], t_0 is the osculating epoch written in the Modified Julian Date (MJD). To get the sidereal time T_sid one has to divide the angle by the factor of $15°\,\mathrm{h}^{-1}$ and reduce the time to an interval between $0\,\mathrm{h}$ and $24\,\mathrm{h}$.

The sidereal angle of the object can be written as

$$s_0 = \Omega + \omega + 360.985\,647\,3°\,\mathrm{d}^{-1} \cdot (t_0 - t_\omega), \tag{3.19}$$

where t_ω is the epoch of passing the estimated perigee. Again, this equation is valid, only if the i is close to $0°$, because else the sum $\Omega + \omega$ has no physical meaning.

3.1.2.4 State Vectors

Using the Keplerian elements, one is not only able to determine the state vectors in the orbital plane, like shown in Chapter 2 by the Eq. (2.1a) and (2.1b). With the information on the inclination, RAAN and the argument of perigee, the state vectors in co-ordinates of the equatorial system can be determined. With the rotation matrices $\mathcal{R}_1$ and $\mathcal{R}_3$, which are commonly defined as

$$\mathcal{R}_1(-\theta) = \begin{pmatrix} 1 & 0 & 0 \\ 0 & \cos(\theta) & -\sin(\theta) \\ 0 & \sin(\theta) & \cos(\theta) \end{pmatrix}, \qquad \mathcal{R}_3(-\theta) = \begin{pmatrix} \cos(\theta) & -\sin(\theta) & 0 \\ \sin(\theta) & \cos(\theta) & 0 \\ 0 & 0 & 1 \end{pmatrix},$$

the vectors $\vec{r}_\Pi$ and $\dot{\vec{r}}_\Pi$ can be expressed in coordinates referring to the equatorial plane, without index Π.

$$\vec{r} = \mathcal{R}_3(-\Omega)\mathcal{R}_1(-i)\mathcal{R}_3(-\omega)\vec{r}_\Pi, \tag{3.20a}$$

$$\dot{\vec{r}} = \mathcal{R}_3(-\Omega)\mathcal{R}_1(-i)\mathcal{R}_3(-\omega)\dot{\vec{r}}_\Pi. \tag{3.20b}$$

One can simplify the multiplication of the matrices. The result is the following rotation matrix:

$$\mathcal{R}_3(-\Omega)\mathcal{R}_1(-i)\mathcal{R}_3(-\omega) =$$
$$\begin{pmatrix} \cos(\Omega)\cos(\omega) - \cos(i)\sin(\omega)\sin(\Omega) & -\cos(\Omega)\sin(\omega) - \cos(i)\cos(\omega)\sin(\Omega) & \sin(\Omega)\sin(i) \\ \cos(\omega)\sin(\Omega) + \cos(i)\cos(\Omega)\sin(\omega) & -\sin(\Omega)\sin(\omega) + \cos(i)\cos(\Omega)\cos(\omega) & -\cos(\Omega)\sin(i) \\ \sin(i)\sin(\omega) & \cos(\omega)\sin(i) & \cos(i) \end{pmatrix}$$

3.1.3 Orbit Determination

To confirm a possible association of new observations and a catalogued object or observations of a newly detected object, an orbit determination is performed. This is done with the *CelMech* routines *ORBDET* and *SATORB*, respectively. While *ORBDET* is used for a first orbit determination, with *SATORB* an orbit improvement step is done. Both routines are briefly described in the next two paragraphs, for further details I refer to [Beut 05].

3.1.3.1 First Orbit Determination with *ORBDET*

With *ORBDET* an orbit determination without knowledge of a priori elements is possible. The user can decide to use a Keplerian orbit (set of six parameters) or a circular orbit (with four parameters; the eccentricity is kept fixed at zero and the argument of the perigee is kept fixed at $0°$).

This orbit can then be stored into an element catalogue, but it can also be used as an a priori orbit for an orbit improvement with *SATORB*.

In the following I describe briefly the determination of a first circular orbit using two observations, also illustrated by Fig. 3.3.
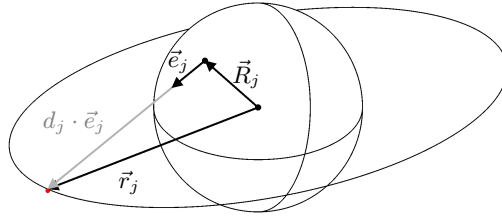
Figure 3.3: First orbit determination (circular orbit, sketch)

The user defines two astrometric positions, represented by the unit vectors $\vec{e}_j$ ($j = 1, 2$) from the observer directing to the object. To achieve suitable results, both observations should separated by a certain temporal gap. Unfortunately, *ORBDET* does not take into account that an object could have performed several revolutions between both observations, they must be selected within one revolution.

The position vectors $\vec{r}_j$ refer to the epoch $t_j - \frac{d_j}{c}$, where t_j is the observation epoch, d_j the topocentric distance of the object at t_j and c the speed of light. The term $\frac{d_j}{c}$ is of the order of $0.1\,\text{s}$ for space debris observations, because the topocentric distance is small compared to the speed of light. The geocentric

distance can be written as

$$\vec{r}_j = \vec{R}_j + d_j \cdot \vec{e}_j. \tag{3.21}$$

The vectors $\vec{e}_j$ with their components right ascension α_j and declination δ_j, and $\vec{R}_j$ with the geographic latitude β and the sidereal angle of the station s_λ, respectively, are both not necessarily in the same reference frame and have to be converted:

$$\vec{e}_j = \begin{pmatrix} \cos(\delta_j)\cos(\alpha_j) \\ \cos(\delta_j)\sin(\alpha_j) \\ \sin(\delta_j) \end{pmatrix}$$

$$\vec{R}_j = R_\oplus \cdot \begin{pmatrix} \cos(\beta)\cos(s_\lambda) \\ \cos(\beta)\sin(s_\lambda) \\ \sin(\beta) \end{pmatrix}$$

The sidereal angle of the station can be determined via its longitude λ and the sidereal angle of the Greenwich longitude (3.18):

$$s_\lambda = \lambda + 100.4606° + 360.985\,647\,3°\,\mathrm{d}^{-1} \cdot (t_j - 51544.5)$$

Longitudes of the Western hemisphere are given with a minus sign, those of the Eastern hemisphere with a plus sign.

Squaring the Eq. (3.21) and solving for d_j leads to an expression for the topocentric distance:

$$d_j = -\vec{e}_j\vec{R}_j + \sqrt{\left(\vec{e}_j\vec{R}_j\right)^2 - \vec{R}_j^2 + \vec{r}_j^2}$$
$$\approx -\vec{e}_j\vec{R}_j + \sqrt{\left(\vec{e}_j\vec{R}_j\right)^2 - \vec{R}_j^2 + a^2}. \tag{3.22}$$

For the determination of a circular orbit one has to replace the absolute value of the geocentric distance, $|\vec{r}_j|$, by the – still unknown – semi-major axis of the orbit a. All other quantities are known and the topocentric distance depends only on the semi-major axis a.

Between the observation epochs t_1 and t_2 the object covers the angle α along its orbit. For this angle both a geometric and a dynamic expression exist. In the geometric equation the angle α represents the included angle by the vectors $\vec{r}_1$ and $\vec{r}_2$ and can be written as

$$\alpha_{\mathrm{geom}}(a) = \angle(\vec{r}_1, \vec{r}_2) = \arccos\left(\frac{\vec{r}_1(a) \cdot \vec{r}_2(a)}{a^2}\right). \tag{3.23}$$

It does not consider whether an object already performed complete revolutions between t_1 and t_2. Therefore t_2 has to be chosen to exclude the possibility of completed revolutions.

The dynamical equation takes the mean motion of the object into account:

$$n = \sqrt{\frac{G\left(M_\oplus + m\right)}{a^3}}$$
$$\approx \sqrt{\frac{GM_\oplus}{a^3}},$$

as defined before in Eq. (2.4). The included angle can then be determined by multiplying the elapsed time in seconds:

$$\alpha_{\mathrm{dyn}}(a) = n \cdot \left(t_2 - \frac{d_2}{c} - t_1 + \frac{d_1}{c} \right)$$
$$\approx \sqrt{\frac{GM_\oplus}{a^3}} \cdot \left(t_2 - \frac{d_2}{c} - t_1 + \frac{d_1}{c} \right) . \tag{3.24}$$

Again, the observation epochs have to be corrected by the topocentric distance divided through the speed of light. These distances can be replaced by Eq. (3.22) and α_{dyn} only depends on the semi-major axis a.

The Eq. (3.23) and (3.24) are equal at the searched radius and one can set up the difference function

$$B(a) = \alpha_{\mathrm{geom}}(a) - \alpha_{\mathrm{dyn}}(a). \tag{3.25}$$

In general, there will be several roots and therefore different radii of the circular approximation of the orbit. Normally, all but one can be excluded.

$$B(a) = \alpha_{\mathrm{geom}}(a) - \alpha_{\mathrm{dyn}}(a)$$
$$0 = \alpha_{\mathrm{geom}}(a) - \alpha_{\mathrm{dyn}}(a)$$
$$= \arccos\left(\frac{\vec{r}_1(a) \cdot \vec{r}_2(a)}{a^2} \right) - \sqrt{\frac{GM_\oplus}{a^3}} \cdot \left(t_2 - \frac{d_2}{c} - t_1 + \frac{d_1}{c} \right) \tag{3.26}$$

In most cases, this equation cannot be solved analytically, but only with iterative procedures, e.g. the Newton method or the Banach fixed-point theorem.

The orientation of the orbital plane with respect to the equatorial plane, represented by the inclination i and the RAAN Ω, can be determined with construction of a vector parallel to the angular momentum:

$$\vec{h} = \vec{r}_1 \times \vec{r}_2 \tag{3.27}$$

The vector $\vec{h}$ does not represent the angular momentum per unit mass (3.9), but the unit vectors point in the same direction. The vector $\vec{h}$ can be used as a substitute for the angular momentum vector. Both observations have to be chosen carefully, especially if observation 2 was chosen when $\vec{r}_1 \parallel \vec{r}_2$ or nearly parallel, $\vec{h}$ would vanish and the following determinations would be impossible.

The calculations for Ω and i are according to Eq. (3.13) and (3.11):

$$\Omega = \arccos\left(\frac{h_1}{-h_2} \right)$$
$$i = \arccos\left(\frac{h_3}{|\vec{h}|} \right)$$

Let u_1 be the argument of latitude of the object's first observation epoch, determined with Eq. (3.14), then the passing epoch through the ascending node, T_0, can be calculated as follows:

$$a \cdot \begin{pmatrix} \cos(u_1) \\ \sin(u_1) \\ 0 \end{pmatrix} = \mathcal{R}_1(i)\mathcal{R}_3(\Omega) \cdot \begin{pmatrix} r_{1,1} \\ r_{2,1} \\ r_{3,1} \end{pmatrix}$$
$$T_0 = t_1 - \frac{d_1}{c} - \frac{u_1}{n} \tag{3.28}$$

Now a complete set of orbital elements for a circular orbit is determined. Subsequently, an orbit improvement step may be performed. When chosen, an eccentric orbit is determined, otherwise the orbital elements of the circular orbit are kept.

The measure of quality of the derived orbit is the root mean square (RMS) of the residuals. The residuals are the differences in right ascension and declination, respectively, between the measurements (t, α^O, δ^O) and the determined positions for the same epochs (t, α^C, δ^C), based on the newly determined orbit. Let P_j stand for the orbital elements before the orbit improvement and P_j^C for those thereafter, then the residuals are in right ascension and declination:

$$v_{\alpha_i} = \sum_{j=1}^{6} \frac{\partial \alpha_i^C}{\partial P_j} \left(P_j - P_j^C \right) - \left(\alpha^O(t_i) - \alpha^C(t_i) \right) \tag{3.29a}$$

$$v_{\delta_i} = \sum_{j=1}^{6} \frac{\partial \delta_i^C}{\partial P_j} \left(P_j - P_j^C \right) - \left(\delta^O(t_i) - \delta^C(t_i) \right), \tag{3.29b}$$

where the index i denotes the epoch t_i.

A number of observations n were used for the orbit determination; the residuals are v_{α_i} and v_{δ_i}. The root mean squared is calculated as:

$$\text{RMS} = \sqrt{\frac{\sum_{i=1}^{n} \left(v_{\alpha_i}^2 \cdot \cos^2(\delta_i^O) + v_{\delta_i}^2 \right)}{2 \cdot n - p}} \tag{3.30}$$

The term $2 \cdot n - p$ represents the degrees of freedom, the number of observations (in right ascension and declination) reduced by the number of fitted parameters. For a circular orbit, $p = 4$ (the eccentricity ε and the perigee ω are not estimated but fixed at default values), for a Keplerian orbit $p = 6$.

3.1.3.2 Orbit Improvements with *SATORB*

Unlike *ORBDET*, *SATORB* uses a model of the gravitational potential of the Earth up to a higher degree and order. It maximum degree and order can be defined be the user, by default the values are $i_{\max} = k_{\max} = 12$.

Additional parameters can also be estimated, like the Solar radiation pressure (DRP), a scaling factor for the area-to-mass ratio (AMR) estimation or empirical parameters for the perturbation equations. The perturbation equations can be displayed by parameters decomposed in a system with two vectors in the orbital plane and one vector perpendicular to the plane. The system in which the vectors are written are arbitrary but the unit vectors have to be linear independent.

With these parameters, *SATORB* performs an iteration in ten steps. Due to the iteration process and additional parameters, *SATORB* leads to more exact results. The measure of quality of an orbit is in both cases, *ORBDET* and *SATORB*, respectively, the root mean squared (RMS) of the residuals similar to Eq. (3.30); only the degrees of freedom have to be adjusted to the estimated parameters:

$$\text{RMS} = \sqrt{\frac{\sum_{i=1}^{n} \left(v_{\alpha_i}^2 \cdot \cos^2(\delta_i^O) + v_{\delta_i}^2 \right)}{2 \cdot n - (6 + p)}} \tag{3.31}$$

The quantities v_{α_i} and v_{δ_i} are equal to Eq. (3.29a) and (3.29b), except for the number of estimated parameters, which has to be adjusted.

With *SATORB*, elliptical orbits are determined, so the number of orbital parameters is always equal to six. In Eq. (3.31), the number p is the number of additionally estimated parameters. For a Keplerian orbit p is equal to zero, with estimating empirical parameters in the RSW- or DSW-decomposition p can be up to equal to three, consequently, depending on how much parameters were actually estimated. When estimating the scaling factor for the Solar radiation pressure, p is equal to one.

3.1.4 Orbit Propagation

If the Earth had a perfect spherical gravitational potential and was the only object in the Solar system, the orbital elements of objects around the Earth would be constant over time; only the mean anomaly would increase.

But due to perturbing effects, orbits change and the orbital elements evolve. When solving the equation of motion (3.1), one does not only get the information of the orbit for the observation epochs but also the temporal evolution into the past and the future.

3.1.4.1 Analytical Propagation

While in the orbit determination process the parameters are estimated, the propagation uses these parameters to determine past or future orbital elements. In case of *SATORB*, the osculating elements of the last orbit determination are used together with the estimated AMR value. This AMR value is assumed to be constant for the complete propagation interval, although studies showed (e. g. [Herz 12b]), that some space debris objects show AMR value variation. This is crucial for HAMR objects, because due to the increased influence of the Solar radiation pressure the orbital parameters evolve differently (see [Herz 12a] for examples of the geostationary ring). If the AMR value changes significantly during the propagation interval, the orbital elements will be propagated wrongly. Other empirical parameters are not used.

3.1.4.2 Numerical Propagation

For the reference calculations, presented in Paragraph 3.2.3, I used Eq. (3.4) as an approximate model of the gravitational potential of the Earth (3.4) with the Sun and the Moon as perturbing objects and started from the evolution of the angular momentum vector described by the time derivative, the torque vector.

In development process of *ZimOProK*, I first assumed constant orbital elements, and later included perturbations. And the evolution itself was calculated with a model of the gravitational potential of the Earth up to degree $i_{\max} = 2$ and order $k_{\max} = 0$ and up to degree and order of $i_{\max} = k_{\max} = 12$, respectively. The calculations with the first model can be performed analytically, presented in the following paragraphs, but in this case the following orbital elements do not change: the semi-major axis, the eccentricity and the argument of perigee remain constant. Therefore, this approach can only give a rough estimation of the evolution of orbital elements. The evolution of the argument of perigee can be determined with another approach.

Torque Vector per Unit Mass

The torque vector is the first time derivative of the angular momentum vector, $\dot{\vec{l}}$:

$$\dot{\vec{l}} = \frac{\mathrm{d}\vec{l}}{\mathrm{d}t} = \frac{\mathrm{d}}{\mathrm{d}t}\left(\vec{r} \times \dot{\vec{r}}\right)$$
$$= \dot{\vec{r}} \times \dot{\vec{r}} + \vec{r} \times \ddot{\vec{r}}$$
$$= \vec{r} \times \ddot{\vec{r}}. \tag{3.32}$$

In this equation, $\ddot{\vec{r}}$ might be replaced by Eq. (3.1), or Eq. (3.4), respectively. and the vector product can be determined. With

$$\vec{l}_n = \int_{t_0}^{t_n} \dot{\vec{l}}\,\mathrm{d}t$$

one would get a new angular momentum vector at epoch t_n. A numerical integration with short time steps Δt_i will give also suitable results:

$$\vec{l}_n = \vec{l}_0 + \sum_{i=1}^{n} \dot{\vec{l}}_i \cdot \Delta t_i \,.$$

This approach is used for the reference calculation of the evolution of orbital elements.

Inclination and Right Ascension of ascending Node
With the components of the angular momentum vector $\vec{l}_n$ we derived the inclination i_n using Eq. (3.11):

$$i_n = \arccos\left(\frac{l_{n,3}}{|\vec{l}_n|}\right). \tag{3.33}$$

and the RAAN Ω_n is calculated with Eq. (3.13):

$$\Omega_n = \arctan\left(\frac{l_{n,1}}{-l_{n,2}}\right), \tag{3.34}$$

Argument of perigee
The oblateness of the Earth causes a secular drift of the perigee (see [Kaul 66]).

$$\dot{\omega} = \frac{d\omega}{dt} = -\frac{3}{4} \cdot n \cdot R_\oplus^2 \cdot \frac{5\cos^2(i) - 1}{a^2\left(1 - \varepsilon^2\right)^2} \cdot C_{20} \tag{3.35}$$

Taking into account only the oblateness term (C_{20}) may be useful for objects of the geostationary ring when propagating over short time intervals, but will lead to false results for objects with smaller semi-major axes. In those cases, one has to take terms of higher degree and order into account, done by the software package *CelMech*. For comparison I limit myself to this degree and order.

Again, a numerical integration is performed, to get the new argument of the perigee.

$$\omega_n = \omega_0 + \sum_{i=1}^{n} \dot{\omega}_i \cdot \Delta t_i$$

3.2   Processing Pipeline *ZimPipe*

As mentioned above, the identification, which objects were observed, is done in a procedure after the extraction of tracklets. Step by step the number of tracklets is reduced and therefore the possibility of multiply associated tracklets.

During the complete filtering process, the following steps are performed: All tracklets, which could be extracted from the observations of a night, are filtered via positions and velocities. These are determined from the observations and are compared to the positions and velocities determined from orbit catalogues. During the filtering process, the tracklets are called differently, depending on the state of the process:

unfiltered	– All tracklets of a night before entering the filtering process.
unassociated	– Tracklets, which could not be associated to a catalogued object, but which are still in the filtering process.
associated	– Tracklets, which could be associated to an already catalogued object.
single	– Tracklets, which could not be associated to a catalogued object, throughout the complete filtering process.
combined	– Tracklets, which could not be associated to a catalogued object, but could be associated to at least one other tracklets of that night.
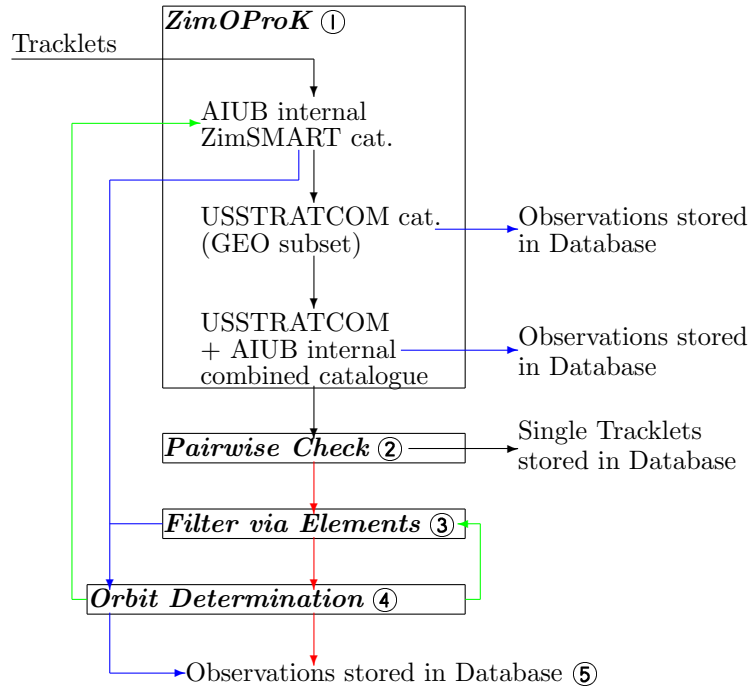
Figure 3.4: Flowchart of the processing pipeline *ZimPipe* (scheme)

Each step is described in more detail in the following subsections. The scheme of the processing pipeline is shown in Fig. 3.4. The boxes correspond to individual routines within the pipeline. The numbers stand for the order in the filtering process within the pipeline. The colour-coded arrows represent the state of the individual tracklets, whether they are unfiltered, unassociated/single, associated or combined.

Three different catalogues were analysed separately: the AIUB internal ZimSMART catalogue, a sub-catalogue of GEO objects from the USSTRATCOM catalogue of unclassified objects. The sub-catalogue of GEO objects of the USSTRATCOM catalogue consists of objects with the following orbital parameters:

- semi-major axis between $35\,000\,\mathrm{km}$ and $47\,000\,\mathrm{km}$

- eccentricity between 0 and 0.2

- inclination between $0°$ and $20°$

The last analysed catalogue is a combined catalogue, consisting of the complete USSTRATCOM and the AIUB internal catalogue.

To confirm that the associated tracklets belong to the associated objects, an orbit determination is performed.

3.2.1 Filter Method via Positions and Velocities – *ZimOProK* ①

The filter program *ZimOProK* consists of the filtering subroutine *COROBS* and the subsequent analysis steps.

The tracklets of objects, which were observed during one series of images, are combined to one file to reduce the analysis steps and to avoid multiple associations. A series of images is defined as consecutive observations of the same field. Multiple associations might occur for objects with short arcs when two or more object images are detected near the determined positions.

3.2.1.1 *COROBS*

For each observation epoch, ephemerides of objects in the TLE catalogue as well as of those in the orbital elements catalogue are calculated. The elements of the catalogue objects are propagated to the current night.

The filtering itself is performed by applying a nearest neighbour decision ([Früh 11]). The criterion is based on a combination of distances between the observations and the ephemerides, which are determined in the following way:

- arc length error – the angular distance between observed position and calculated ephemerides

- intrack and crosstrack error – the deviation of the measured to the calculated positions in-plane and out-of-plane

- deviation in apparent velocity

- angle between apparent velocities of the ephemerides and observations

The determined single differences are weighted as described in [Früh 11] and are used to determine a measure for the smallest distance. An analysis of the USSTRATCOM TLE catalogue led to empirical limits for the parameters, given in Tab. 3.2. Further investigations with more catalogue objects led to values of the intrack and crosstrack errors, which are slightly differing from those given in [Früh 11].

Table 3.2: Limits of the parameters used by *COROBS*

Parameter	Upper limit
Arc length error	$0.16°$
Intrack error	$82\,\mathrm{km}$
Crosstrack error	$57\,\mathrm{km}$
Deviation of the apparent velocity	$0.05\,\mathrm{millidegree/s}$
Angle between direction of motion	$1°$

In general, there are two classes for possible associations: most likely candidates and others. A selection is made which might be the most probable object for the investigated tracklet. The decision is non-ambiguous as for each tracklet maximum one nearest neighbour is selected.

There are two cases when this process leads to wrong results. On the one hand, it is possible that the objects of two or more tracklets are near the calculated position of one catalogue object.

On the other hand, the list of possible candidates might be too long to make any decision concerning the nearest neighbour. In this case, the subroutine does not provide an output. As seen in Chapter 2, this happened several times when analysing MEO surveys. Due to this results the maximum number of

possible candidates was increased to cover the most cases. There will be still a problem when a tracklet belongs to an object of a large debris cloud, a nearest neighbour decision might be ambiguous. When several tracklets of one series are associated to the same object, an orbit determination has to be used to identify the correct ones.

For small clouds the process leads to correct results, as shown in [Früh 11] on the basis of the ASTRA satellite clusters.

The number of probable candidates also depends on the number of objects in the used catalogue. Using subcatalogues instead of one with all available objects might reduce the probability of multiple correlations. But as a disadvantage, maybe not the best decision is made, when a better matching object would be in a catalogue analysed later.

Finally, *COROBS* only gives a list of nearest neighbour decisions, the interpretation and combination of the tracklets to the associated objects is done separately.

3.2.1.2 Selecting possible Connections

The lists of nearest neighbour decisions are read out and if there is a nearest neighbour given, the corresponding tracklet is associated. In case, more than one tracklet of a series is associated to the same object, the correct tracklet must be selected by an orbit determination; for the correct tracklet the orbit determination will be successful, for the others it will not.

Tracklets, which were successful associated, are removed from further analysis steps. If the object is in the USSTRATCOM or the AIUB internal catalogue, the observations are just stored. But if it is in the AIUB internal ZimSMART catalogue then the name of the object is written in a list for the automatic orbit determination process, which concludes the pipeline.

3.2.2 Pairwise Check for possible Connection ②

The leftover tracklets are checked pairwise if some of them belong together. A first orbit determination is performed with *CelMech*. If the RMS of the residuals is below $1.5''$ the tracklets are defined to belong together.

The tracklets are numbered in temporal order, tracklets belonging to one series are not tested against each other as they were found on the same images and it is impossible that they belong together.

Tracklet number 1 is tested with the numbers 2, 3 and so on until a match is found or all tracklets are tested. If a match is found through the first orbit determination, the other tracklets are skipped. The underlying hypothesis is that if tracklets belong together (e. g. number 1, 3 and 6), then the connection will be successful by identifying the matches between tracklet 1 and 3 and later between 3 and 6. A connection of the tracklets 1 and 6 is implied, which is in general correct.

When all pairs containing tracklet 1 are tested as well as a connection could be found, pairs with tracklet 2 is tested with 3, 4 and so on, but already matched tracklets are skipped. The hypothesis here is that if 1 and 2 do not match but 1 and 4 do, then 2 and 4 also do not match.

An example will illustrate the method in more detail: six tracklets are investigated, from which the tracklets 1, 3 and 6 will belong together.
The complete testing order is: $1-2$, $1-3$ (match!), $2-4$, $2-5$, $2-6$, $3-4$, $3-5$, $3-6$ (match!), $4-5$.
Here, the combinations $1-4$, $1-5$, $1-6$, $2-3$, $4-6$ and $5-6$ are skipped, because of the hypotheses above.

Tracklets, which could be combined, are stored in a file with the name of the first tracklet but with a different file extension to avoid confusion with the original tracklet. Those newly created files are called

"object candidates". If in the subsequent filter step no association to a catalogued object can be found then they are stored into the AIUB internal ZimSMART catalogue as newly detected objects.

3.2.3   Filter Method via orbital Elements ③

If a tracklet is not being associated to a catalogued object, it does not necessarily mean that this tracklet does not belong to any object. On the one hand, if the time difference to the last observations is large, the propagation of the orbital elements as well as the determined positions and velocities may cause large differences to the observed ones.

On the other hand, orbit determinations with tracklets of only one night may result in orbital elements with large errors and that some of the orbital elements are correlated to each other. Consequently, the determined orbit does not exactly represent the true orbit. So, the propagation of the orbit may worsen the situation by departing more and more from the true orbit.

When the orbital elements were compared directly without calculating positions and velocities, some of the leftover tracklets could also be associated to catalogued objects. In this filter step the limits of the investigated elements are wider and using it as a first step would lead to a large amount false connections.

In this filter method, the orbital elements of objects in the AIUB internal ZimSMART catalogue are propagated to the current investigated night. These propagated elements are then compared to the elements from the first orbit determination of the "object candidates".

Constant Keplerian Elements
The simplest assumption is that orbital elements do not change significantly between two nights. One has to define an uncertainty interval, based on the past successful connections. If the orbit determination was successful, the observations are stored into the database and the orbital elements are updated.

The number of associated tracklets was insufficient, and two evolution models were tested: first with a model of the gravitational potential of the Earth up to degree $i_{\max} = 2$ and order $k_{\max} = 0$. Thereafter, the gravitational potential up to degree and order of 12 and numerical integration, both provided by *SATORB*, is used. Additionally, perturbations of the Sun, Moon were included into the calculations, and in the latter case also those of the planets.

Considering the Evolution of the Keplerian Elements
Assuming constant Keplerian elements is sufficient if the time interval between observations is not too large, ideally if observations stem from subsequent nights. If this is not the case then new tracklets may not be associated to an object although they would belong to it.

The Fig. 3.5(a) to 3.6(b) show the results of three different propagation methods, exemplified by the inclination and the RAAN. The blue squares represent results of orbit determinations. The first orbit was calculated with observations only of that night, while for the other orbits the observations were added. Each result is used as a starting point for the individual propagation methods and is then propagated until the following osculating epoch.

The red lines represent constant elements. The black curve represents the model of the Earth's gravitational potential up to degree $i_{\max} = 2$ and order $k_{\max} = 0$, while the green curve represent one up to degree and order of $i_{\max} = k_{\max} = 12$ as well as perturbations of the Sun, Moon and planets, mentioned above.

Figure 3.5(a) shows the evolution of the inclination of an object over 12 days. The object is a geosynchronous object with an eccentricity of about 0.1 and a semi-major axis of about 42 166 km, based on a first orbit determination. Each set of elements is propagated to the osculating epoch of the next orbit

determination, in steps of one tenth of day ($\hat{=}2.4\,$h). For the following propagation interval, the newly derived orbital elements were used.

As one can see, the deviation for the inclination between the constant assumption and the evolution models is about $0.002°$ within a time interval of 12 days. Going to a larger time intervals after the first orbit determination (e. g. 63 days, Fig. 3.5(b)), the deviation from the constant approach increases to approximately $0.02°$. Also, the evolution can only be described correctly by using higher degrees and orders of the gravitational potential.

The same approach was used for the RAAN (Fig. 3.6(a) and 3.6(b)). The colour code is equal to the figures before. For short time intervals the deviation between the constant assumption and the evolution models is below $0.01°$, but for larger time intervals, also the deviation increases. For example, the difference of the RAAN between the first two orbits is about $0.04°$ after a time interval of 6 days.

For that reason, the constant approach was replaced by one of the evolution models. The model with the model of the gravitational potential of the Earth up to degree $i_{\max} = 2$ and order $k_{\max} = 0$ leads to large deviations after propagating the orbital elements over several days, therefore the model with a gravitational potential up to degree and order of $i_{\max} = k_{\max} = 12$ is used.

When an orbit determination is performed with short arcs, as it is done with new tracklets, the comparison of all Keplerian elements is not advised. For the filter method via orbital elements, the semi-major axis a, the inclination i and the RAAN Ω were selected as elements to be compared. The limits, given in the Tab. 3.3(a) and 3.3(b), are different for the orbit types GEO, eGEO, GTO, MEO and eMEO, respectively. Furthermore, the limits of catalogued objects with observations of one night (shown in Tab. 3.3(a)) differ from those of catalogue objects with observations of more nights in Tab. 3.3(b), due to the different accuracies in orbit determinations. For some orbit types even less orbital elements are compared (marked with $-$). The reason therefore is, that there were too few successful connections to achieve suitable statistical results.

Table 3.3: Compared orbital elements and maximum limits for the deviation

(a) Limits for objects with observations of one night

Orbital Element	GEO	eGEO	GTO	MEO/eMEO
Semi-major axis (km)	950	1100	—	—
Inclination (°)	0.4	0.5	10	10
RAAN (°)	40	—	—	—

(b) Limits for objects with observations of several nights

Orbital Element	GEO	eGEO	GTO	MEO/eMEO
Semi-major axis (km)	1150	1100	—	—
Inclination (°)	0.1	0.5	10	10
RAAN (°)	3	—	—	—

The limits presented in the Tab. 3.3(a) and 3.3(b) are larger than the real differences (cf. Fig. 3.5(a) to 3.6(b)), but the limits were calculated from all successful connection of each orbit type. Successful means that the RMS of an orbit determination with the new observations was below $2''$.

The limits themselves were determined from the maximum value plus the standard deviation of the distribution for each orbital element. The new limits were updated regularly as more data becomes available to reduce the number of false connections.
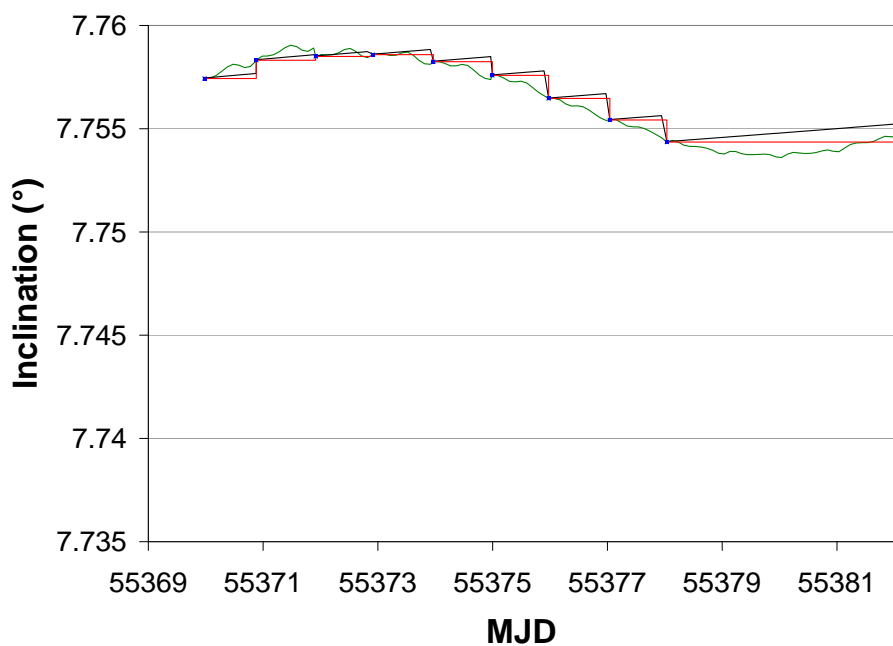
(a) Time interval 12 d
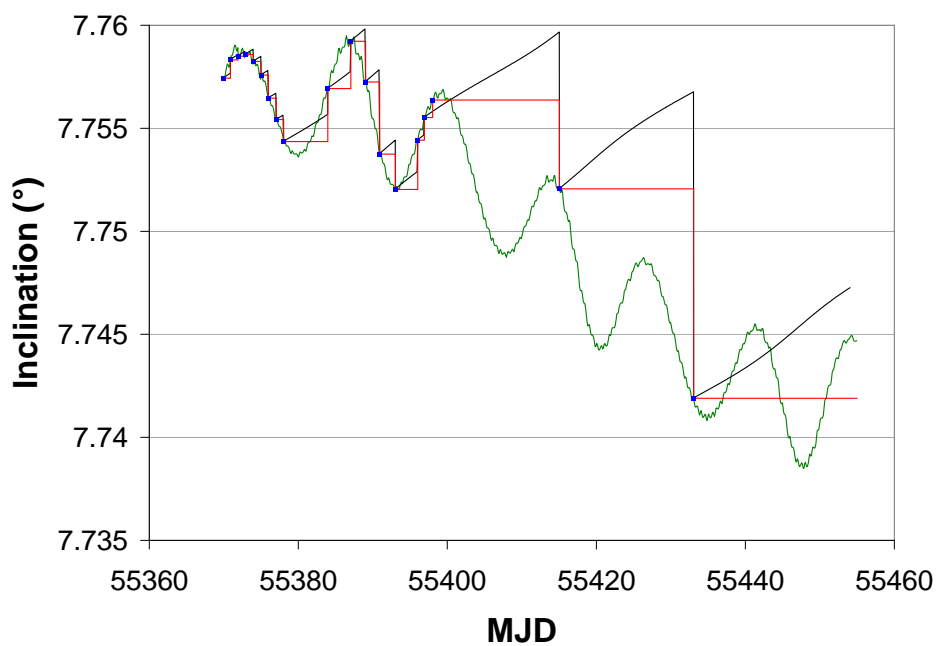
(b) Time interval 63 d

Figure 3.5: Propagation of orbital elements, exemplified by the inclination.
Blue squares: results of orbit determinations, red lines: assumption of constant inclination,
black line: perturbations with gravitational potential up to degree $i_{\max} = 2$ and order
$k_{\max} = 0$, green line: perturbations with gravitational potential up to degree and order of
$i_{\max} = k_{\max} = 12$.

(a) Time interval 12 d

(b) Time interval 63 d

Figure 3.6: Propagation of orbital elements, exemplified by the RAAN.
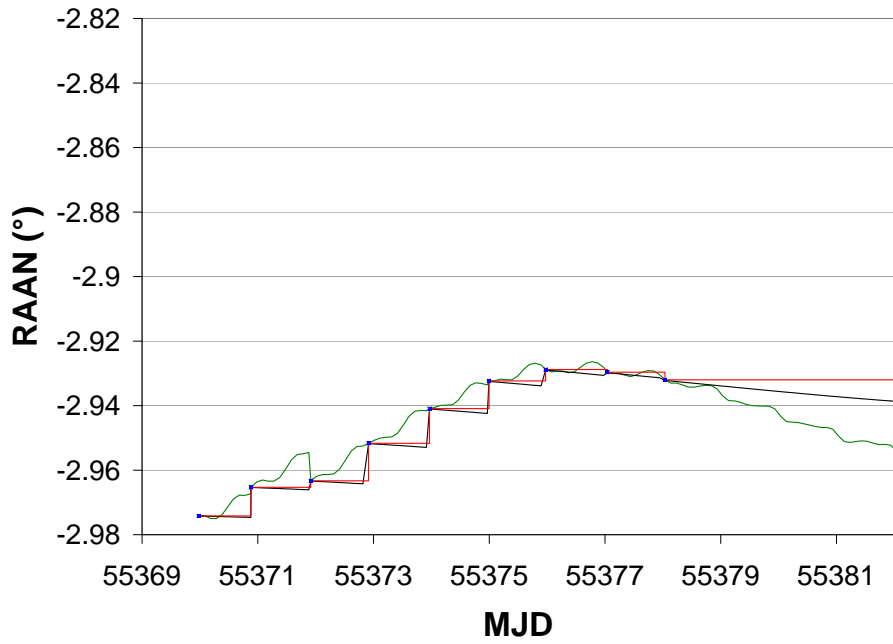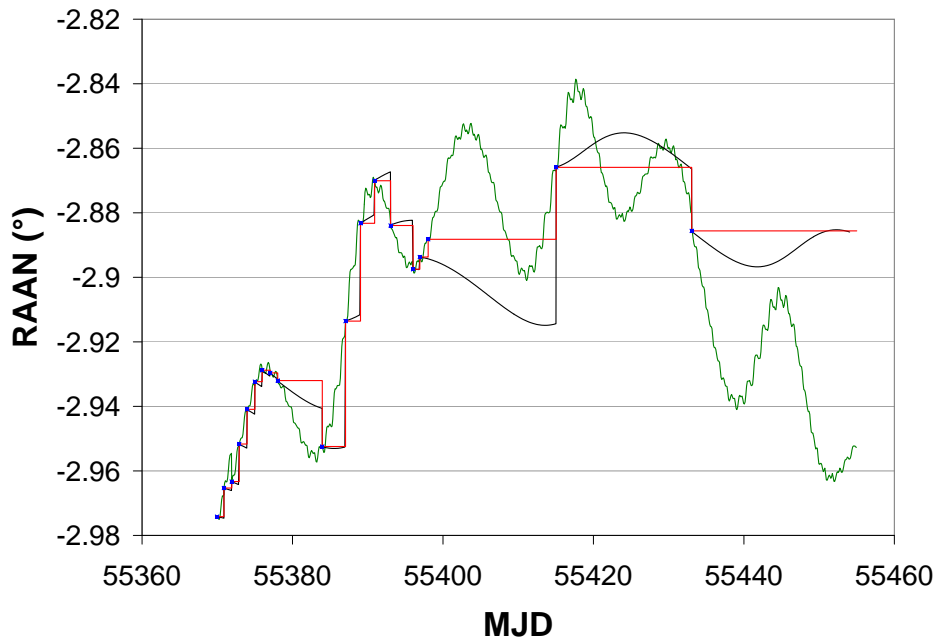Blue squares: results of orbit determinations, red lines: assumption of constant RAAN, black line: perturbations with gravitational potential up to degree $i_{max} = 2$ and order $k_{max} = 0$, green line: perturbations with gravitational potential up to degree and order of $i_{max} = k_{max} = 12$.

Synchronous Elements

The RAAN Ω is not well defined for orbits with small inclinations, and the argument of the perigee is not well defined for orbits with small eccentricities. Therefore, for orbits with eccentricities lower than 0.01 and inclinations lower than 1°, the Keplerian elements are replaced by synchronous elements. Prior to the comparison of the elements, the elements themselves are checked whether the comparison should be done with the Keplerian or the synchronous elements.

Although this approach should only be applied to GEO objects, it is possible to investigate also objects of other orbital regions, provided not every synchronous element is compared. The mean longitude drift rate D is constant for circular orbits and choosing exclusively the mean longitude drift rate, the comparison is also applicable to MEO objects. Therefore the possibility is not excluded in the object identification process, although the data set of successful connections is too small to derive suitable limits.

The limits for D are different for objects with observations from one nights and several nights, respectively. For GEO objects with observations from one night the limit is $0.025\,\mathrm{d}^{-1}$, with observations from several nights the limit becomes $0.001\,\mathrm{d}^{-1}$. These values correspond to a maximum difference of the semi-major axis of about 702 km and 28 km, respectively. While the limit for observations from one night has the same order of magnitude like in the comparison of the Keplerian elements (702 km compared to 950 km), the limit for observations from several nights is much narrower (28 km compared to 1150 km).

For MEO objects, the data set with only one confirmed association is too small to gain statistically suitable results and for observations of one night as well as of more nights, respectively, the limit of the mean longitude drift rate is set to $0.1\,\mathrm{d}^{-1}$. This corresponds to a difference of the semi-major axes of about 2811 km. This value can also be used as a first hint when comparing the Keplerian elements.

3.2.4 Confirmation of associated Tracklets ④

Objects of the AIUB internal ZimSMART catalogue were filtered and an orbit determination was performed. Firstly, this is to confirm that the associated tracklets really belong to these objects. Secondly, in case that more than one tracklet of one image series was associated to the same object, the correct tracklet need to be selected. Thirdly, the "object candidates", which could not be associated to catalogue objects in the orbital elements filter step, are stored as new detections and a first orbit is determined. An orbit determination for an object of the first two cases is an orbit improvement performed with *SATORB*. Orbits of new detections are assumed to be circular and are determined with *ORBDET*.

3.2.4.1 Catalogued Objects with new Tracklets

The orbit determination of each catalogued object with newly associated tracklets is performed automatically and has only to be checked when the limits to accept an orbit are exceeded. One limit is the RMS, derived with Eq. (3.31), which is set to 2″. If the RMS is greater than 2″, then the oldest observations used in the orbit determination are removed until the RMS is below 2″. Nevertheless, at least two older nights with observations had to be used for an orbit determination, to connect the new observations to the last determined orbit. If this was not possible as the orbit determination also failed, the new tracklets most likely do not belong to the object.

A second criterion is, that the scaling factor for the Solar radiation pressure must be positive, if it is estimated. If the estimation of this factor leads to a negative factor, the new tracklets most likely do not belong to that object.

3.2.4.2 Newly detected Objects

The so-called "object candidates", tracklets which could be connected to other tracklets of that night but could not be associated to catalogue objects, are treated differently. First, an orbit determination

with *ORBDET* is performed, which is a prerequisite for an orbit improvement with *SATORB* or the ephemeris calculation.

For a successful orbit determination with *ORBDET*, we require that the RMS, calculated with Eq. (3.30), does not exceed $2''$.

If there are at least three tracklets spread over the entire night used in the orbit determination, then an orbit improvement with *SATORB* is feasible. As pointed out before, the time interval between the first and the last observation of one tracklet is approximately 1 min, which is an arc of only about 0.07 % of the complete orbit of a geostationary object. Consequently, one tracklet can essentially be considered as one single position on the orbit. An elliptical orbit has six orbital elements and thus needs at least three tracklets for the orbit determination.

3.2.5   Storage into the Catalogue ⑤

The "object candidates" are finally stored into the AIUB internal ZimSMART object catalogue. At this point, they get a catalogue name. The naming convention is similar to the AIUB internal catalogue: Z*yydoy*$\mathcal{L}$, where Z stands for ZimSMART, *yy* the two digit year and *doy* the day in the year of detection. Finally, the letter(s) $\mathcal{L}$ indicatethe sequence number of the detection within the night. For example, Z08161A is the first object found in the 161$^{\text{st}}$ night in 2008 (equal to the night June 9$^{\text{th}}$/10$^{\text{th}}$).

The catalogue is updated with the newly detected objects and the latest derived orbital elements of all detected catalogue objects. Older elements of the latter objects are still available in the data sets, for comparison.

3.3   Results of the Processing Cycles

The data presented in this thesis are based on the analysis of ZimSMART observations. There was no existing processing tool and the newly developed pipeline *ZimPipe* evolved through different development stages. First, I only used the filter method via positions and velocities. In a second run, with processing all tracklets from the beginning and to achieve a higher rate of correlated tracklets, I added an additional filter step, the filter method via orbital elements. During the further development the filter method via orbital elements was refined by the possibility to use either Keplerian elements or synchronous elements, deoending on the inclination and the eccentricity.

The description of the first run and the first part of the second run are brief and has only demonstrative character. The description of the complete second run will demonstrate the full performance of the processing pipeline.

3.3.1   The Data Set

Although ZimSMART is used for routine observation, it is in a experimental state and software as well as hardware changes are made. Due to a hard disk and computer change, the information about the number of observed fields has been lost, but the number of tracklets is available. Figure 3.7 shows the distribution of analysed tracklets per month.

3.3.2   First Run

The first run was performed with the filter method via positions and velocity only. This has been done in order to show the efficiency of the tool *COROBS* in a routine processing and forms the basis for further comparison with additional filter steps.
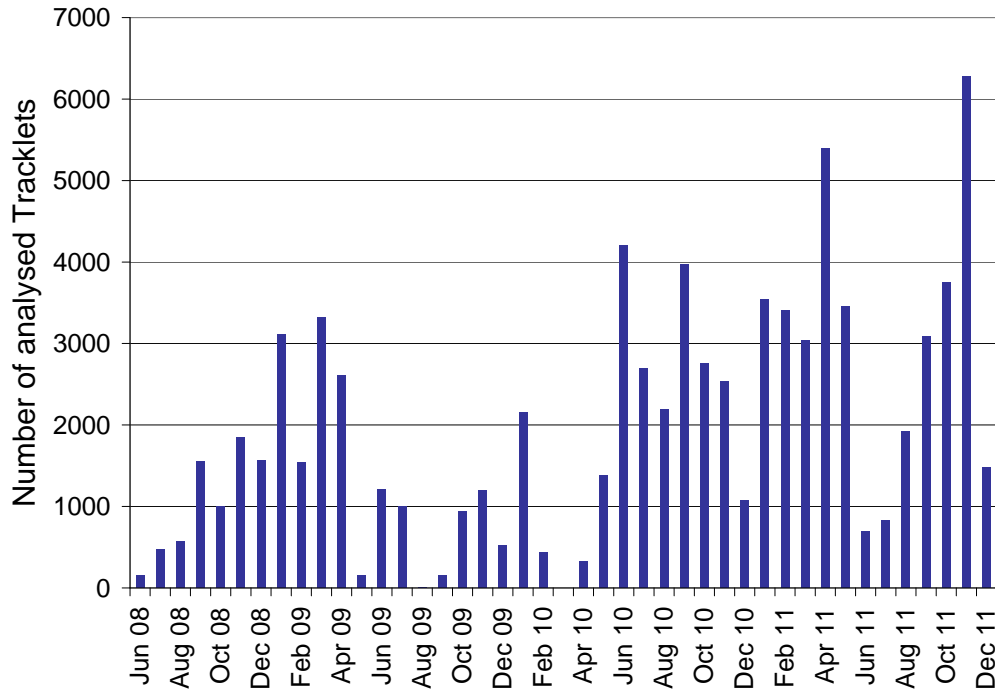
Figure 3.7: Distribution of analysed tracklets per month

The first observation period began on June 9th, 2008 and lasted until August 1st, 2009. Within these 419 days, there were 92 nights with observations, where 84360 images were taken. A total of 20109 tracklets could be extracted from these images.

Among these tracklets, there were 133 tracklets ($\hat{\approx}$ 0.66 %) of all tracklets) which consisted of two observations (sets of epochs and positions) only. However, each filter step needs at least three observations to give suitable results. This means that 19976 tracklets were analysed.

After *COROBS*, 17263 tracklets, which is approximately 86.4 % of all analysed tracklets, could be associated to catalogued objects. Figure 3.8 shows the number of observed objects in the analysed catalogues. There were found 899 objects of the USSTRATCOM catalogue (blue sector) and 17 objects of the AIUB internal catalogue (red sector).

The other 2713 tracklets remained unassociated, ($\hat{\approx}$ 13.6 %). These tracklets were tested pairwise, whether they belong together. If at least two tracklets matched, they were stored as one object in an independent AIUB internal ZimSMART catalogue.

This way, 574 preliminary uncatalogued objects were stored into the AIUB internal ZimSMART catalogue (green sector in Fig. 3.8). These objects might not be individual objects and one object may be listed under several names. This is because of the uncertainties in the orbital elements. The determined errors of the orbit may be large, especially when the orbit is based on observations from one night only. When those elements are propagated the orbital errors will grow further and new tracklets of the same object will be associated to that object.

On the other hand, even if a tracklet was associated to an object, it does not mean that it really belongs to this object. The same uncertainties can cause that the determined positions and velocities are in agreement with a new tracklet by chance.
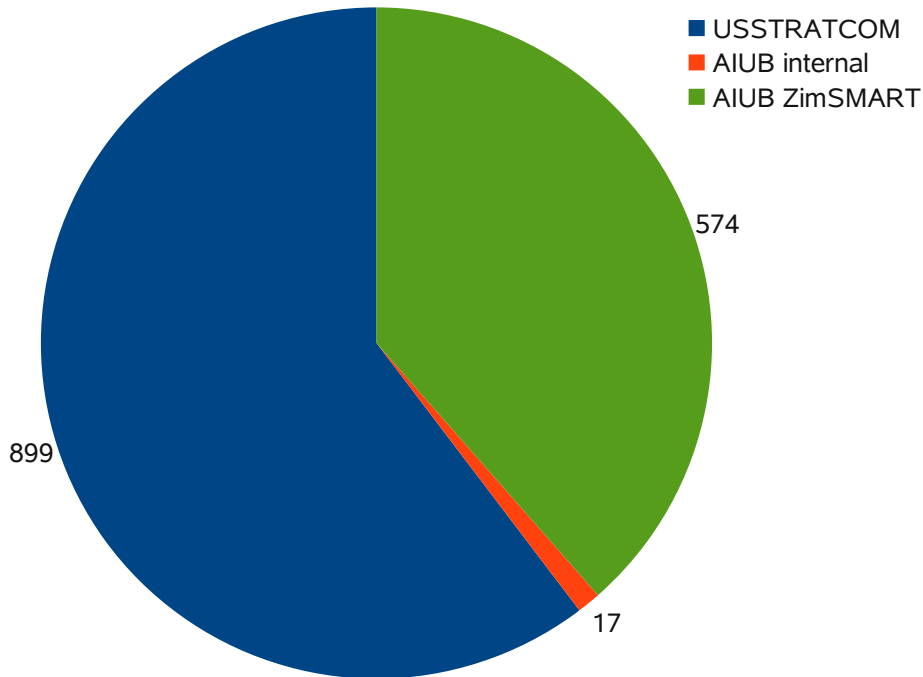
Figure 3.8: Distribution of observed objects, selected by catalogue

3.3.3 Second Run – first Part of the Data Set

The filtering method via orbital elements was added for testing purposes. During this run the method underwent different enhancements, from using only constant orbital elements to considering the propagation of orbital elements. The last enhancements were to use synchronous elements to increase the fraction of correlated tracklets of objects with small eccentricities and inclinations.

To confirm that adding this new filter step reduces the number of unassociated tracklets significantly, I compared the results of the first run with those of the second run within nearly the same time interval.

The period ended on August 5st, 2009, but the total number of nights with observations increased only by one to 93 with respect to the first run. Also, the number of tracklets only increased insignificantly to 20110.

The number of discarded tracklets stayed at 133, which is approximately $0.66\,\%$ of all tracklets. They consisted of two observations, which is not sufficient to achieve suitable results. This means, 19977 tracklets were analysed.

This time, *COROBS* could associate 17364 tracklets ($\widehat{\approx}\ 86.9\,\%$ of all analysed tracklets) with already catalogued objects. This means that 101 tracklets more than in the first run could be associated. The reason therefore is not a change within *COROBS*. Due to the second filter step, more tracklets could be associated to objects in the AIUB internal ZimSMART catalogue and their orbits became more accurate. As a consequence, the filter method with *COROBS* in subsequent nights was more successful than before.

After the second filter step, via orbital elements, only 932 tracklets remained unassociated, which corresponds to approximately $4.7\,\%$ of the analysed tracklets. This means, $95.3\,\%$ of all analysed tracklets could be associated to catalogued objects. Figure 3.9 shows the distribution of the relative frequencies per month of the unassociated tracklets after *COROBS* and after the complete process.
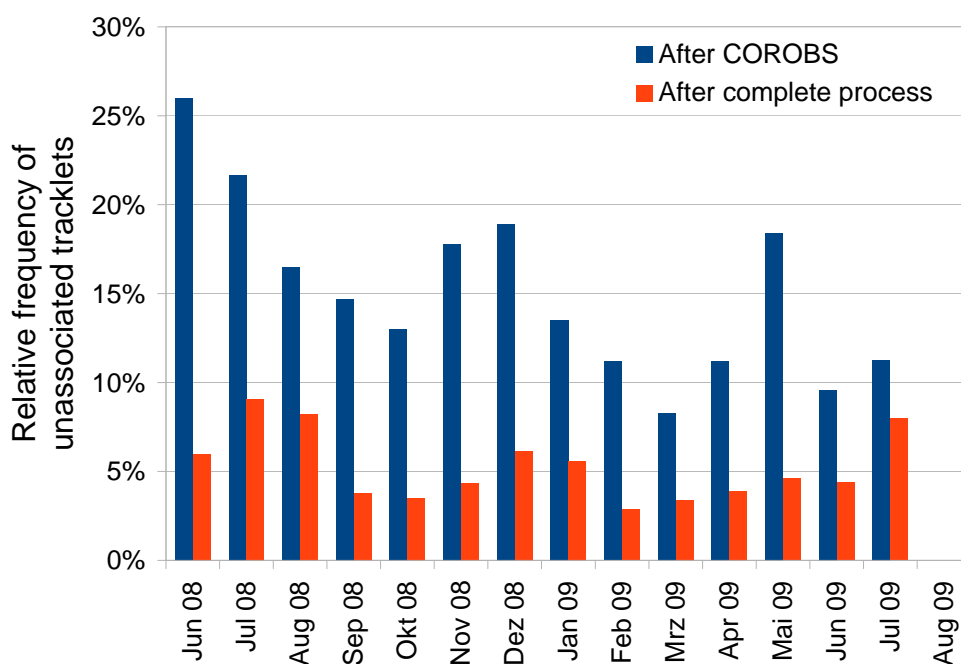
Figure 3.9: Relative frequency of unassociated tracklets per month after *COROBS* (blue) and after the complete process (red)

Figure 3.10 shows the distribution of observed objects, where 901 objects could be identified from the USSTRATCOM catalogue, representing two objects more than in the first run. In the AIUB internal catalogue there were 18 identified objects (+1). Because of the second filter step and and improving orbits after associating more tracklets to already catalogued objects, the number of objects in the AIUB internal ZimSMART catalogue decreased by 63 to 511. It means that 63 objects, which were categorised as individual objects in the first run, did indeed belong to already catalogued objects.

Figure 3.11 show the distribution of different object types in the AIUB internal ZimSMART catalogue. The classes are according to the definitions given in Section 1.1.1 and 1.1.2, resectively. The number of objects represent only partially the ratios between the different object classes. As the survey scenario was optimised for GEO objects, it was less likely to observe an eGEO or GTO object in a second stripe in that night than a GEO object. Also, the detected GEO objects might not be individual objects; one object could be stored into the catalogue under several names, when more recent tracklets could not be associated to older ones.

The small number of MEO and eMEO objects is due to the shorter analysis interval of the MEO surveys and also due to a lack of bright uncatalogued objects in the analysed orbital planes.
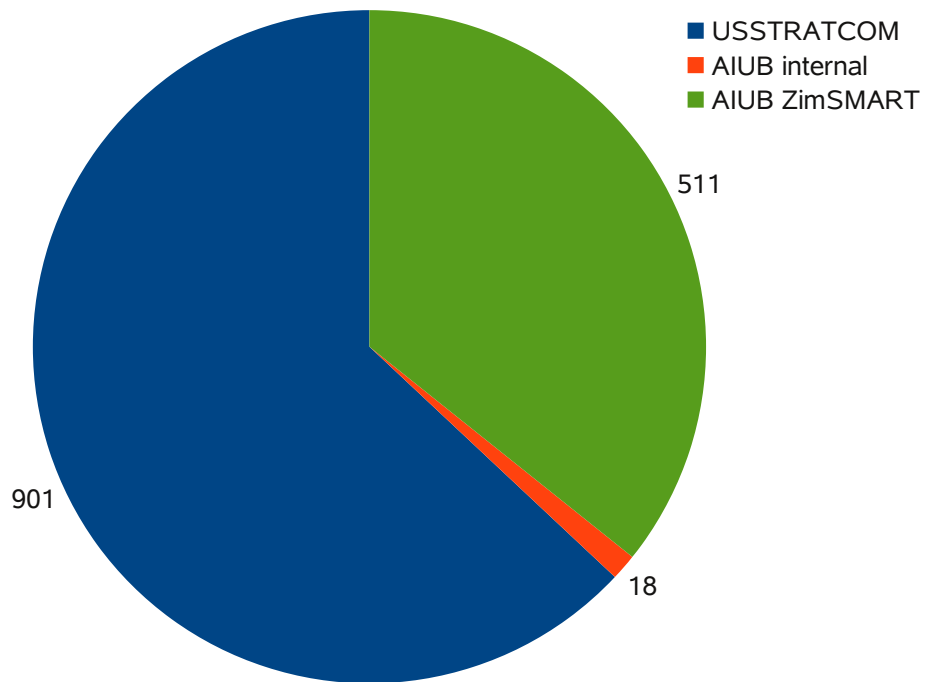
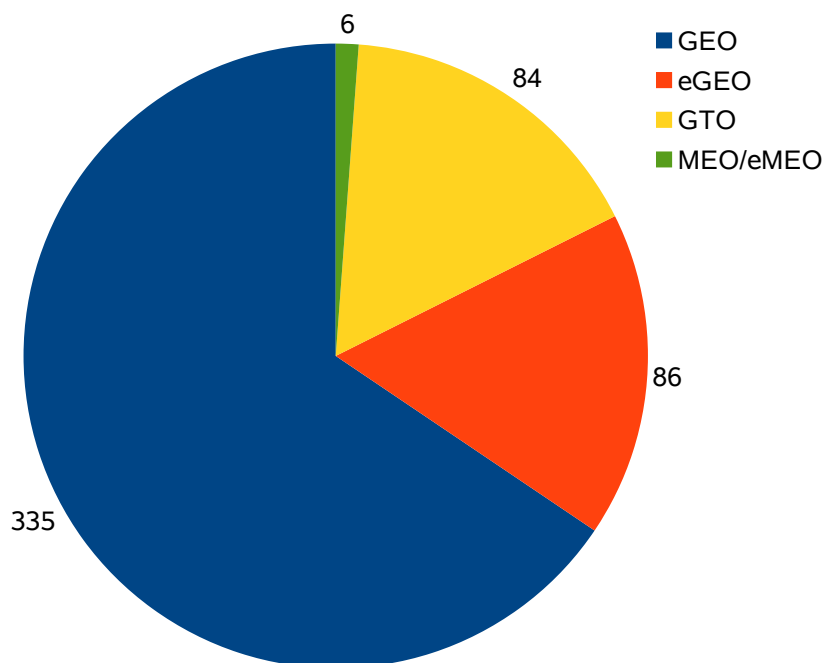**Figure 3.10:** Distribution of observed objects, selected by catalogue

Figure 3.11: Distribution of objects in the AIUB internal ZimSMART catalogue, selected by object type

3.3.4 Second Run – complete Data Set

After deciding in favour of the new filter step, the analysis continued with this set-up. Nevertheless, the individual filter steps passed through modifications from time to time, like adjustments of the filtering parameters. The latter were initially determined with a subset of successful assciations where the statistical significance was small. With more successful associations the parameters could be readjusted and the number of wrongly associated tracklets could be reduced.

The observations were taken in 360 nights between June 9th, 2008 and December 14th, 2011. Within these nights 343910 images were taken and 85012 tracklets could be extracted. Among these, there were 2164 tracklets ($\approx 2.5\%$) with only one or two entries. Those had to be discarded and 82848 tracklets were analysed.

After *COROBS*, 68744 tracklets could be associated to already catalogued objects, which is about 83.0%. That means, only 14104 tracklets ($\hateq 17.0\%$), left unassociated. By performing also the filtering step via orbital elements, the amount of unassociated tracklets could be reduced to 7354 tracklets. This represents approximately 8.9%. The number of unassociated tracklets per month is shown in Fig. 3.12. The blue bars represent the fraction of unassociated tracklets after the first filter step *COROBS*, the red bars after the complete filtering process. The fraction of unassociated tracklets of the entire analysis interval is slightly higher than for the first part of the data set (17.0% compared to 13.1%), but still of the same order of magnitude. With the additional filter step via orbital elements, this fraction could be almost reduced by a factor of two.
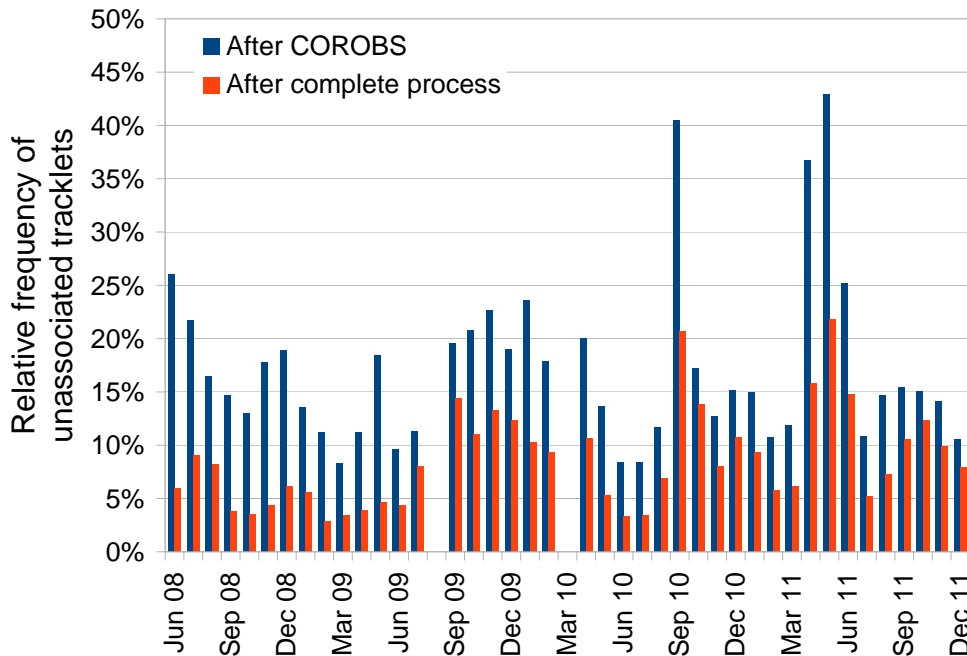

Figure 3.12: Relative frequency of uncorrelated tracklets per month after *COROBS* (blue) and after the complete process (red)

3.3.4.1 Associated Tracklets

In total, 1491 objects with 67359 tracklets were associated with the USSTRATCOM catalogue of unclassified objects. Another 817 tracklets were associated to 41 objects of the internal AIUB catalogue.

Whether all tracklets really belong to the associated objects of the USSTRATCOM catalogue was not confirmed by orbit determinations. Therefore, it is unknown, how many tracklets were associated wrongly. Tracklets associated to objects of the AIUB internal catalogue were confirmed by oebit determination.

There were 15537 tracklets, which could not be associated to any catalogued object, but belonged to at least one other tracklet. They were stored into the AIUB internal ZimSMART catalogue; in total, these are 2040 objects. For this catalogue, associated tracklets are always confirmed by an orbit determination.

Figure 3.13 shows the distribution of observed objects by catalogue. With 2040 objects, the majority of objects belong to the AIUB internal ZimSMART catalogue, 1491 objects to the USSTRATCOM catalogue of unclassified objects were found. The other 41 objects belong to the AIUB internal catalogue of objects, discovered with the ESASDT in Tenerife.
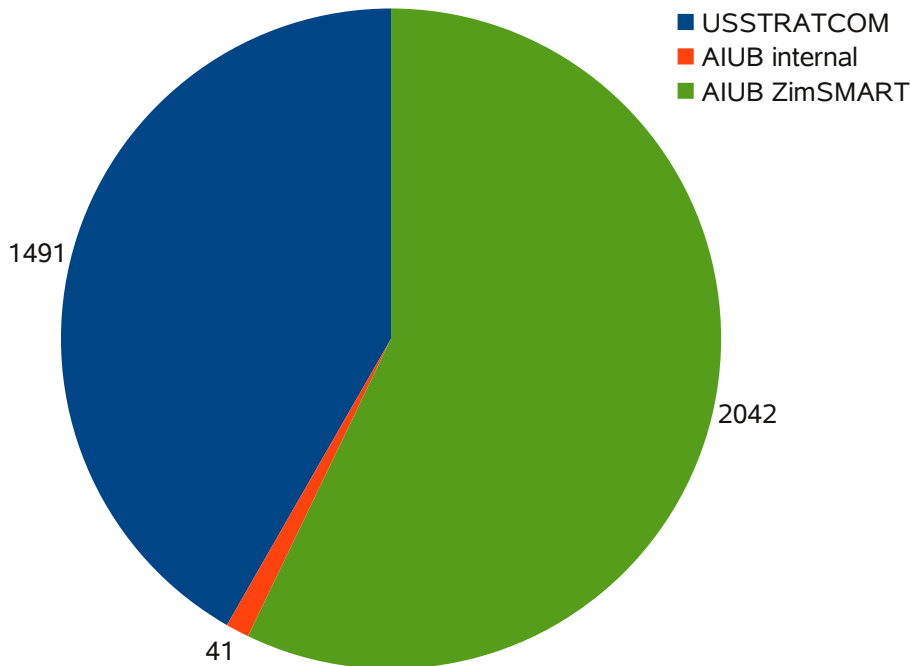
Figure 3.13: Distribution of observed objects, selected by catalogue

3.3.4.2 Multiply and wrongly associated Tracklets

The number of analysed tracklets (82848) compared to the sum of associated tracklets (83713) leads to a difference of 865 tracklets. This means, that several tracklets were associated multiple times.

These multiple associations can occur, when two objects are in a similar orbit and have the similar orbital elements. Especially when debris clouds or stallite clusters are observed, tracklets might be associated wrongly. A study to minimise the number of wrongly associated tracklets, was performed with observations of the ASTRA satellites by C. Früh ([Früh 11]). For debris clouds with objects, which are closer together, this problem is unsolved.

Another case, when two orbits appear as identical, is the following: an object of the USSTRATCOM catalogue had a manoeuvre and its TLEs were not updated yet. New observations could not be associated to that object. If two tracklets or more were found, these observations were stored as a newly detected object into the AIUB internal ZimSMART catalogue. Later, when the TLEs of the original object were updated, the comparison leads to two identical orbits. The tool *COROBS* cannot decide, which orbit is correct and sets the same flag for both objects. The subsequent association step then only uses the flag without checking if the tracklet was associated to more than one object.

On on hand with investigating one large catalogue of objects, the multiple associations of the second kind are likely. On the other hand, when using several smaller catalogues, a tracklets might not be associated to the correct object, but to the best matching object in that catalogue. The compromise found in this analysis

It is also possible that two or more tracklets, belonging to the same series of images, were associated to the same object. Only one of these tracklets may belong to the object, as two simultaneous tracklets must belong to two separate objects. Based on the selection criteria of *COROBS* no decision can be made, which tracklet does belong to the associated object and which do not, and sets the same flag for all tracklets. The subsequent association step then takes these tracklets and merges them with older tracklets of that object.

The identification of the wrongly associated tracklets is performed with an orbit determination. Only for the correct tracklet, the orbit determination will be successful, for the others, it will lead to orbits with large uncertainties, large residuals or it will not converge at all, respectively.

Within the investigation period, 666 tracklets were wrongly associated to objects of the AIUB internal ZimSMART catalogue. Compared to the 15537 tracklets of objects in the AIUB internal ZimSMART catalogue, this number represents a fraction of 4.3 %.

3.3.4.3   The AIUB internal ZimSMART Catalogue

The AIUB internal ZimSMART catalogue consists of objects, whose observations were not associated with the USSTRATCOM or the AIUB internal catalogue. Figure 3.14 shows the distribution of object types in the catalogue. The majority, 1382 objects, are objects in geosynchronous orbits (GEO). 281 objects in the catalogue had eccentric geosynchronous orbits (eGEO). 325 objects were on highly eccentrical transfer orbits (GTO). The other 54 objects belonged to the MEO region and consisted of circular orbits as well as of elliptical ones (MEO/eMEO).

Taking these numbers and also the analysed and associated tracklets, I can conlcude that a build-up of an object catalogue with an survey-only approach is possible.

The more difficult is the maintenance of that catalogue. This includes observations of the objects on a regular basis to update the orbital elements.

Although I showed in Chapter 2, that one week is sufficient to cover the visible part of the geostationary ring, this does not neccessarily mean that each object is observed. The orbits of many objects are not exactly geostationary or geosynchronous, which means that they drift in longitude and that they are not visible for a certain time span from a given observation site.

Figure 3.15 shows the numbers of objects with observations of at least one night, two nights, three nights and more than three nights, respectively. The numbers above the black line give the total number of objects in the AIUB internal ZimSMART catalogue with these arc lengths. 903 objects were observed in at least two nights ($\approx 44\,\%$ of the total number). This means that nearly 56 % of the objects are lost after the first night. They might be redetected later, but not identified and stored in the catalogue with a new name. For objects with observations in more than two nights, the situation becomes worse: more than 77 % of all objects are lost.
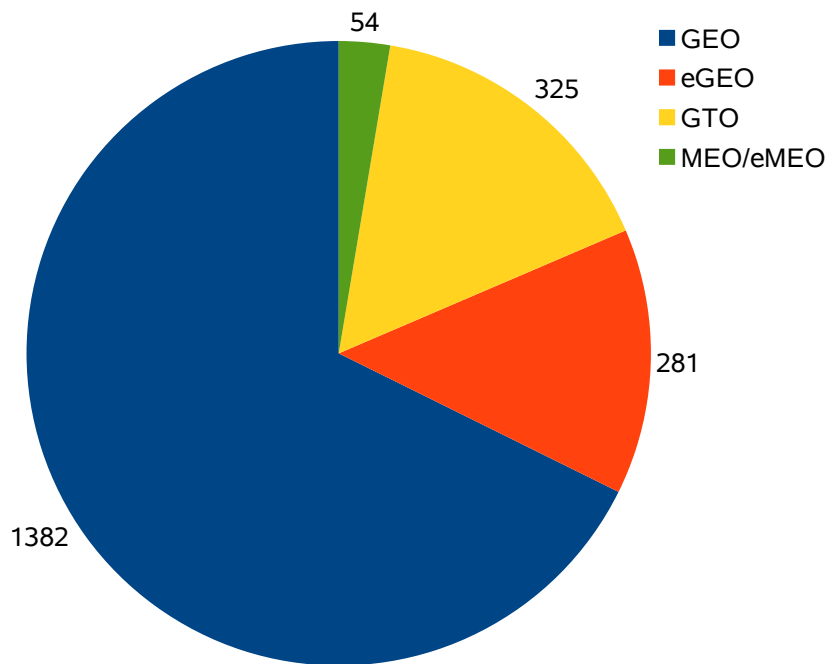
Figure 3.14: Distribution of objects in the AIUB internal ZimSMART catalogue, selected by object type
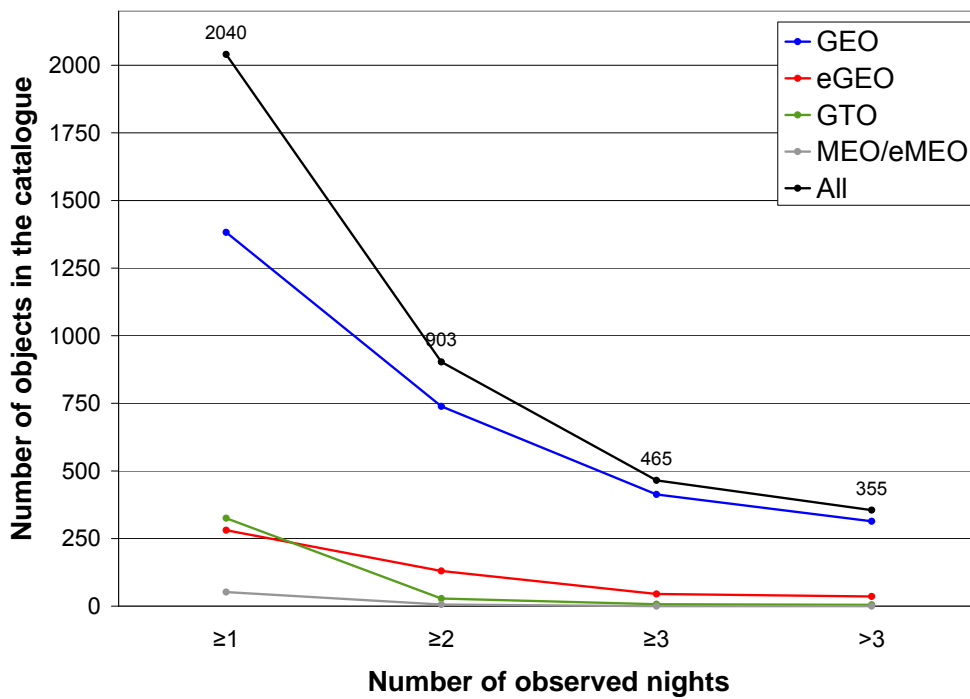

Figure 3.15: Number of objects in the AIUB internal ZimSMART catalogue with observations in different nights

The reasons are in the problematic orbit determination of short arcs and the corresponding propagation errors, as well as in non-regular observations. The influence of the time interval between the first and the second nights is shown in Fig. 3.16. The time interval is in units of one day and a time interval equal to one day represents subsequent nights. The 903 objects, which were observed in at least two nights, were analysed how large the time interval between the first and second night with observations was. The distributions are shown separately for the following orbit types: circular, geosynchronous orbits (GEO), eccentric orbits (eGEO/GTO/eMEO) and circular orbits in the MEO region (MEO). The majority of objects, 283 of 903 ($\approx 31.3\%$), were observed in the night right after the night of detection, representing the ideal case. They consist of 237 GEO objects, 44 eGEO/GTO/eMEO objects and 2 MEO objects.

Including also larger time intervals, 533 objects were observed for the second time within ten nights after detection, representing approximately 59.0%: 438 GEO, 93 eGEO/GTO/eMEO and 2 MEO objects, respectively. This means, that no MEO object was found after a time interval of more than one night. The reasons were that not all pseudo-objects fields were observed each night and that the investigated orbital planes were changed after a certain time.
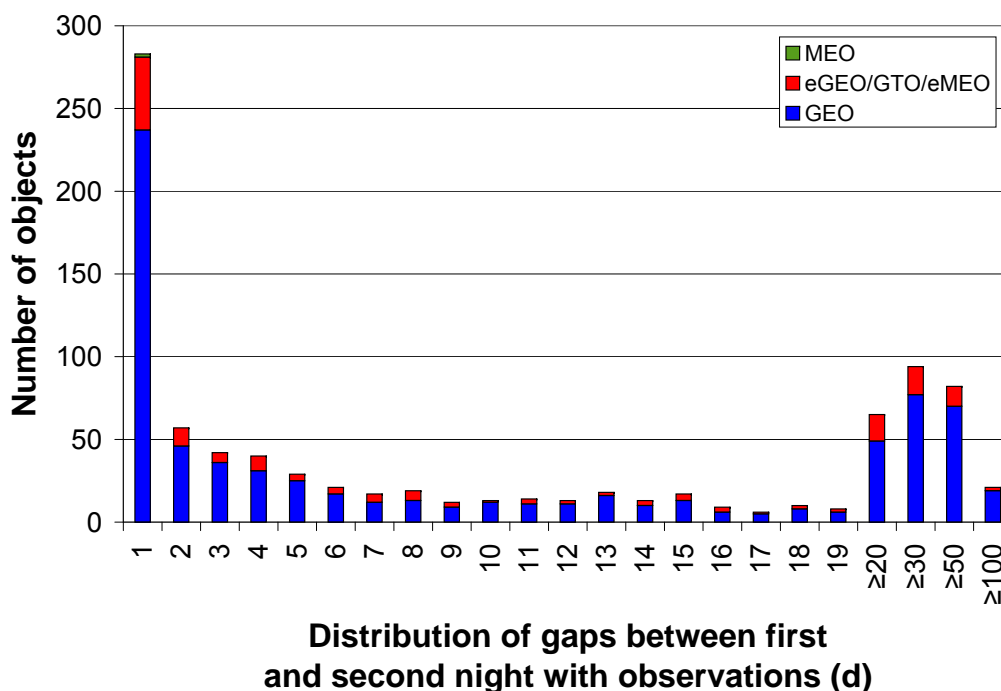
Figure 3.16: Time interval in days between the first and the second night with observations

The analysis, how long the objects of the AIUB internal ZimSMART catalogue were observed, led to Fig. 3.17. The figure displays the arc lengths of the objects, which were observed in at least two nights. Most objects have total arc lengths of more than 20 days, but below 50 days. The ratio of objects with near-circular orbits to those with eccentric orbits is approximately 4:1 for total arc lengths shorter than 100 days. A number of objects have total arc lengths of more than 100 days, but the fraction of objects with eccentric orbits is smaller than before.
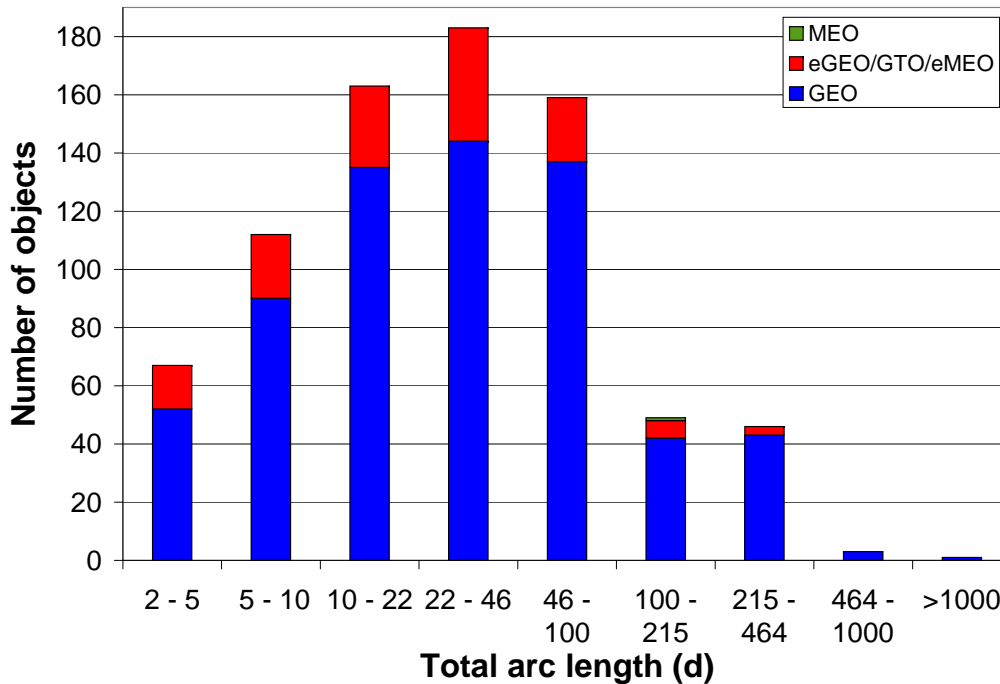
Figure 3.17: Distribution of total arc lengths of the objects in the AIUB internal ZimSMART catalogue; only objects observed in at least two nights are considered

3.4 Concluding Remarks

In this chapter, the build-up and maintenance of an object catalogue of objects in the geostationary ring as well as in the Medium Earth Orbit region has been presented.

When extracting the coordinates of the observed objects, an object identification has not been performed immediately, because often, several objects have been detected on one series of images and the object identification would have been very time consuming.

The object identification process had to be performed afterwards. For this purpose, the processing pipeline *ZimPipe* has been developed. It consists of three filter steps. First, the tracklets were analysed with *COROBS*, which determines positions and velocities based on catalogued orbital elements and compares them to observations. Second, the remaining, unassociated tracklets have been tested, if there are some, which belong together. When such matching tracklets have been found, they were called "object candidates". Third, these "object candidates" have then been filtered via their orbital elements, whether they belong to objects of the AIUB internal ZimSMART catalogue. Those "object candidates", which could not be associated to any object, have been stored as new objects into the catalogue.

ZimPipe is suited for tracklets of objects of the geostationary ring as well as of the MEO region. When performing MEO surveys (presented in Section 2.3), the observations have been extracted in the same way as those of objects from surveys in the geostationary ring and they are all processed together.

The statistical analysis of the catalogue led to the conclusion that the maintenance of an object catalogue is problematic, when observations have been obtained in survey-only mode by a single sensor. More than 77 % of all objects were observed for three nights or less and then lost eventually. This might be enough when a second telescope in a sensor network also observes the objects. This additional telescope might operate in follwo-up mode, i.e. tasked observations, or another telescope operating in survey-only mode.

Nevertheless, when an object could be observed for more than three nights, it is possible for a single sensor to be observed for a longer time span, as Fig. 3.17 shows. A catalogue of GEO objects can be maintained also this way.

A possible scenario for a telescope with follow-up observations can be that the most interesting objects, detected in the preceding night, are stored into the observation schedule of the follow-up telescope. The term "most interesting" refers to the current field of interest: it can be HAMR objects or objects with highly eccentric orbits.

Drifters and manoeuvring satellites are an unsolved problem. Tracklets of drifting objects might be associated to the correct object, if the orbital plane evolves like propagated. This also depends on the AMR value of the object, amongst the orbitel elements. The orbital elements are propagated , expecting the AMR value to be constant. This is not necessarily the case as earlier studies showed (e. g. [Musc 10], [Früh 11] and [Herz 12b]). If the AMR value shows strong variation, an object might not be redetected as the determined positions and velocities do not agree with the real ones.

The change of orbital elements compared to propagated ones is also problematic for manoeuvring objects. The orbital elements are changed after a manoeuvre compared to those before, consequently the filter steps do not give associations. While problem with the drifters can be solved by a network of sensors, the manoeuvres have to be detected by a subsequent analysis step, discussed in the following chapter.

Chapter 4

Manoeuvre Detection

> Abandon all hope, ye who enter
> here.
>
> Dante Alighieri

Orbital planes are not stable, due to the disturbing forces of the Sun and Moon, and the gravitational potential of the Earth. This means for geostationary satellites, that they will move away from the equatorial plane, where they are supposed to be. From the operator's point of view, manoeuvres are important to ensure that the mission of a satellite can be accomplished. For example a television satellite, which covers parts of Europe and provides the corresponding TV signals, will drift away after a certain time, and it might appear above Asia, or – even worse – might be uncontrollable forever, because signals from the operational ground station cannot reach the satellite anymore, and will be lost eventually. Therefore, only manoeuvres can expand the satellites' life times.

Of course, the observer's point of view is different. Manoeuvres transfer the satellite in a new orbital plane, which creates problems in terms of object identification and orbit determination processes, and results in absence of the exact manoeuvre data in two possible cases for an individual satellite:

1. If the elements of that satellite are recently updated after the manoeuvre, the new orbit is included in the planning phase and the telescope observes the correct co-ordinates. If the object is actually observed and tracklets are extracted. The observations and orbital elements of the former orbital plane are tried to connect to these newly extracted observations, but an orbit determination will probably fail. So:
   The satellite could be observed and identified, but the corresponding orbit determination failed!

2. The elements are not updated and the telescope observes the co-ordinates, where the satellite would have been without manoeuvring. Despite the manoeuvre, the satellite may still be in the FoV of the telescope. It may be observed and tracklets may be extracted, but the tracklets cannot be associated to the supposed satellite. So:
   The satellite could be observed, but the identification failed! An orbit determination would fail as well.

In the following investigation, focus has been laid on the second case, because the orbital elements in the AIUB internal catalogues are based on the last orbit determination. The propagation of the orbital elements is performed with *SATORB*, introduced in Section 3.1.4. The investigation of manoeuvres was limited to satellites in the geostationary ring, because the analyses use synchronous elements, presented by [Soop 94] and introduced in Chapter 3. These elements are only valid if the inclination is close to

$0°$ and the eccentricity is close to zero. Therefore, the manoeuvre detection analysis is assessable for geostationary objects, only.

In general, a manoeuvre changes all orbital elements

$$(D, \lambda_0, e_x, e_y, i_x, i_y) \xrightarrow{\text{manoeuvre}} (D + \Delta D, \lambda_0 + \Delta \lambda_0, \varepsilon_x + \Delta \varepsilon_x, \varepsilon_y + \Delta \varepsilon_y, i_x + \Delta i_x, i_y + \Delta i_y),$$

but in special cases some of them stay constant. In the following two kinds of manoeuvres are investigated.

4.1 Types of Manoeuvres

There are the following criteria to distinguish manoeuvres. They are characterised by their thrust length or the direction of the thrusting.

The thrust lengths can be short or long. For short thrusts, the thrust interval can be approximated to be instantaneous, corresponding to one single thrust epoch; it is assumed that the position vector stays constant during the thrust. During a long thrust this position vector changes and the total thrust time interval has to be taken into account. Referring to [Soop 94], long thrusts can also be expressed as one short thrust in the middle of the manoeuvre with adjusted parameters.

The direction of the thrust are divided into two types, an in-plane and an out-of-plane manoeuvre. The in-plane manoeuvre is also called East-West station-keeping manoeuvre (EWSK), while the out-of-plane is called North-South station-keeping manoeuvre (NSSK). These manoeuvres are performed separately and hardly simultaneously.

4.1.1   North-South Station-keeping Manoeuvre

Figure 4.1: Orientation of orbital planes before (black) and after (blue) an NSSK manoeuvre (sketch); the object (black dot) is at the point of its manoeuvre

When the thrust is perfectly perpendicular to the orbital plane, only the inclination of the orbit is changed. The other orbital elements will stay the same. I take the two-dimensional inclination vector (3.15) to display the change after the manoeuvre (again by [Soop 94]):

$$\begin{pmatrix} i_x \\ i_y \end{pmatrix}_{\text{new}} = \begin{pmatrix} i_x \\ i_y \end{pmatrix}_{\text{old}} + \frac{\Delta V}{V} \begin{pmatrix} \sin(s) \\ -\cos(s) \end{pmatrix}, \tag{4.1}$$

where V is the absolute value of the satellite's orbital velocity and ΔV the velocity change perpendicular to the orbital plane caused by the thrust. By definition, a $\Delta V > 0$ represents a thrust in Northern

direction, $\Delta V < 0$ in Southern direction. The sidereal angle of the satellite s is determined according to Eq. (3.19).

The value of the new inclination can be calculated with squaring the equation above:

$$i_{\text{new}} = \sqrt{i_{\text{old}}^2 + \left(\frac{\Delta V}{V}\right)^2 + \frac{2i_{\text{old}}\Delta V}{V}\cos\left(s - \Omega_{\text{old}}\right)} \tag{4.2}$$

To eliminate the components of the old inclination vector, i_x and i_y, and to display the Keplerian elements, the RAAN of the old orbit Ω_{old} was included. The inclination before the manoeuvre, i_{old}, is defined as:

$$i_{\text{old}} = \sqrt{i_{x,\text{old}}^2 + i_{y,\text{old}}^2}.$$

The old and the new orbital plane cross each other at two points (A and B in Fig. 4.1). Accordingly, once every half orbital period the distance between the propagated radius vectors reaches a minimum. As both orbital planes are not stable, the crossing points are not stable, too, but at least for the first periods after the manoeuvre it is a valid assumption.

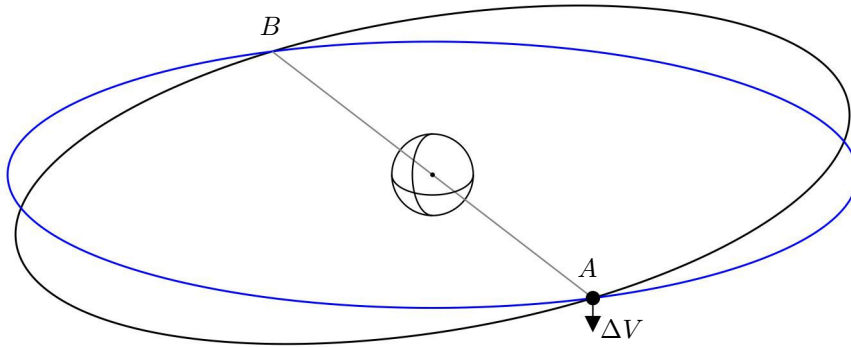## 4.1.2 East-West Station-keeping Manoeuvre
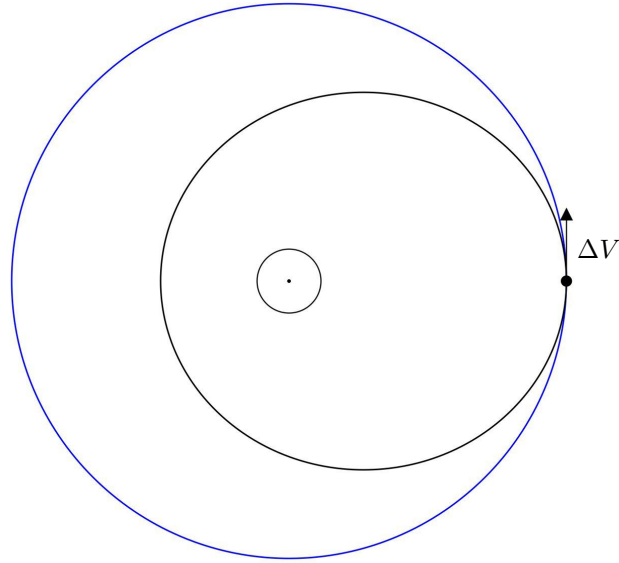
Figure 4.2: Orientation of orbital planes before (black) and after (blue) an EWSK manoeuvre (sketch); the object (black dot) is at the point of its manoeuvre

When the thrust vector lies perfectly within the orbital plane, the shape of the satellite's orbit with the following orbital elements are subject to change: the mean longitude at epoch λ, the mean longitude drift rate D (and therefore the semi-major axis a) and the eccentricity ε (taken from [Soop 94]).

$$\lambda_{\text{new}} = \lambda_{\text{old}} + \frac{3\Delta V}{V}\left(s - s_0\right), \tag{4.3}$$

$$D_{\text{new}} = D_{\text{old}} - \frac{3\Delta V}{V}, \tag{4.4}$$

$$\begin{pmatrix} \varepsilon_x \\ \varepsilon_y \end{pmatrix}_{\text{new}} = \begin{pmatrix} \varepsilon_x \\ \varepsilon_y \end{pmatrix}_{\text{old}} + \frac{2\Delta V}{V}\begin{pmatrix} \cos\left(s\right) \\ \sin\left(s\right) \end{pmatrix}, \tag{4.5}$$

with V and s defined as above, but ΔV is here the velocity change in the direction of motion. The sidereal angle s_0 is calculated for the epoch of the osculating elements. By definition, a thrust with $\Delta V < 0$ represents a thrust in Western direction and $\Delta V > 0$ in Eastern direction. With $\Delta V > 0$, the satellite is accelerated, the semi-major axis becomes larger and the point of the manoeuvre becomes the new perigee. Similar to that, with $\Delta V < 0$, the satellite is decelerated, the semi-major axis becomes smaller and the point of the manoeuvre becomes the new apogee. The old and the new orbit are tangent to each other at the point of the manoeuvre (see Fig. 4.2). The orbits have a close conjunction once an orbital period. Here again, the old and the new orbit are both perturbed differently, but at least for one period the tangent point can be considered to be stable.

The value of the new eccentricity can also be calculated:

$$\varepsilon_{\text{new}} = \sqrt{\varepsilon_{\text{old}}^2 + \left(\frac{\Delta V}{V}\right)^2 + \frac{4\varepsilon_{\text{old}}\Delta V}{V}\cos\left(s - \Omega_{\text{old}} - \omega_{\text{old}}\right)} \qquad (4.6)$$

Here, to eliminate the components of the old eccentricity vector, ε_x and ε_y, the RAAN Ω_{old} and the argument of the perigee ω_{old} were included. The eccentricity before the manoeuvre, ε_{old}, is defined as:

$$\varepsilon_{\text{old}} = \sqrt{\varepsilon_{x,\text{old}}^2 + \varepsilon_{y,\text{old}}^2}.$$

With knowledge of type, epoch and thrust of the manoeuvre, it is possible to determine the orbital elements, either synchronous or Keplerian, after the manoeuvre.

4.1.3 The Observer's Point of View

For an observer the information about the manoeuvres are mostly not available. Normally, one discovers a manoeuvre has taken place, when an orbit determination fails although the tracklets belong to the same object. The only information might be that the manoeuvre was performed between the last and the first of the current observations, which can be a large interval.

As pointed out before, a manoeuvre changes the orbit of an object. Therefore, one has to take the last elements before the manoeuvre and the first ones thereafter. Both element sets have to be compared at the epoch of the manoeuvre. The older elements are propagated into the future, the current ones into the past. They can be converted into state vectors, which were introduced in Section 3.1. The state vectors must fulfil the following condition at the time of the manoeuvre t_M: the position vector propagated with both the old and new elements, $\vec{r}_o$ and $\vec{r}_n$, must be equal,

$$\vec{r}_o\left(t_M\right) = \vec{r}_n\left(t_M\right).$$

A similar consideration can be applied to the velocity vectors at the epoch of the manoeuvre. The new and the old velocity vectors both differ by the thrust vector $\Delta\vec{V}_M$:

$$\vec{v}_n\left(t_M\right) = \vec{v}_o\left(t_M\right) + \Delta\vec{V}_M.$$

Working with real observations and orbital elements determined thereof, computationally exact equalities cannot be achieved. In addition, orbital uncertainties leads to deviations of the position vectors from each other at the epoch of the manoeuvre, when propagating the orbital elements. The determined vectorial velocity difference will deviate from the given thrust vector.

In general, the thrust vector and the total thrust time interval are unknown. As pointed out above, a long thrust can also be interpreted as a short thrust with adjusted parameters, therefore I consider every manoeuvre to be instantaneous.

If I assume that a geostationary satellite was observed in the night before the manoeuvre and thereafter, then it would pass the point of the manoeuvre only once and the epoch of the manoeuvre is well defined.

The more revolutions are passed between the observation before and after the manoeuvre, the more ambiguities occur concerning the estimation of the epoch of the manoeuvre.

4.2 Detection and Analysis Method

The base for the analysis are orbits. One orbit has to be determined with observations before the assumed manoeuvre, using the longest possible arc to achieve good results. For orbits after the manoeuvres, the observations of the first three nights were used. The procedure is close to the routine process, where the observations after a manoeuvre were filtered to the object, the orbit determination fails, but it is ensured that the same object was observed. With observations of two nights or less, the new orbit is too inaccurate to compare the components of the velocity vectors. For comparison, this is shown in the tables for circular orbits based on two tracklets after the manoeuvre. A manoeuvre can be expected, if the following conditions are fulfilled:

1. The distance between the both radius vectors at the manoeuvre epoch, determined from the orbits before and after the manoeuvre, respectively, must be equal. With real observations the equality will not be achieved, but I expect the absolute distance to be very small at the manoeuvre, compared the distances at other epochs:
$$\Delta R = |\vec{r}_o(t_M) - \vec{r}_n(t_M)| \approx 0$$

2. The angle between the velocity vectors of both radius vectors must be small because the thrust vector is small compared to the velocity vectors. This angle can be determined with the scalar product:
$$\cos(\alpha_v) = \frac{\vec{v}_o(t_M) \cdot \vec{v}_n(t_M)}{|\vec{v}_o(t_M)| \cdot |\vec{v}_n(t_M)|}$$

3. The vectorial velocity difference must be in the order of magnitude of the given thrust vectors,
$$\Delta \vec{V}_M = \vec{v}_o(t_M) - \vec{v}_n(t_M).$$

As far as available, the determinations can be compared to given values.

4.2.1 Propagation to a selected Epoch

The osculating elements before and after the assumed manoeuvre, respectively, are both propagated to the same epoch. For each element set, the state vectors are determined and compared to each other.

If the selected epoch is equal to the assumed manoeuvre epoch, the vectorial velocity difference leads to a supposed thrust vector and can be compared to provided date if available. The difference of the position vectors should vanish, $\Delta R \approx 0$.

4.2.2 Scan between osculating Epochs

If the epoch of the manoeuvre is unknown, the time interval between both osculating epochs has to be scanned. The orbits at the given osculating epochs are propagated to different epochs between them and compared to each other. From the results, a distinction between manoeuvres can be made.

The temporal distance between the osculating epochs of both element sets can be large. Consequently, a too detailed scan can be very time consuming. On the other side, if the time steps are too large, the epoch of the manoeuvre night not be detected. Therefore, the time steps in the analysis are variable, depending on the absolute value of the difference of the velocity vectors ΔR. The smaller ΔR gets, the closer is the conjunction of both propagated radius vectors and the smaller is the time step for the

following propagation epoch. When approaching the epoch of the manoeuvre, the time steps becomes smaller, after that epoch they become again larger. If there are more close approaches within the analysed interval, the size of the time steps also changes. This is necessary when the epoch of the manoeuvre is ambiguous, then several possible manoeuvre epochs can be investigated.

The time steps for EWSK manoeuvres are ten times larger than for NSSK manoeuvres, because otherwise NSSK manoeuvres would not be detected.

Table 4.1: Time steps of the scanning routine for EWSK and NSSK manoeuvres, respectively

ΔR (m)	Times steps for EWSK	for NSSK
> 1000000	$2\,\text{d}$	$0.2\,\text{d} \stackrel{\wedge}{=} 4.8\,\text{h}$
> 464158	$1\,\text{d}$	$0.1\,\text{d} \stackrel{\wedge}{=} 2.4\,\text{h}$
> 215443	$0.5\,\text{d} \stackrel{\wedge}{=} 12\,\text{h}$	$0.05\,\text{d} \stackrel{\wedge}{=} 1.2\,\text{h}$
> 100000	$0.2\,\text{d} \stackrel{\wedge}{=} 4.8\,\text{h}$	$0.02\,\text{d} \stackrel{\wedge}{=} 28.8\,\text{min}$
> 46415	$0.1\,\text{d} \stackrel{\wedge}{=} 2.4\,\text{h}$	$0.01\,\text{d} \stackrel{\wedge}{=} 14.4\,\text{min}$
> 21544	$0.05\,\text{d} \stackrel{\wedge}{=} 1.2\,\text{h}$	$0.005\,\text{d} \stackrel{\wedge}{=} 7.2\,\text{min}$
> 10000	$0.02\,\text{d} \stackrel{\wedge}{=} 28.8\,\text{min}$	$0.002\,\text{d} \stackrel{\wedge}{=} 2.88\,\text{min}$
> 4641	$0.01\,\text{d} \stackrel{\wedge}{=} 14.4\,\text{min}$	$0.001\,\text{d} \stackrel{\wedge}{=} 1.44\,\text{min}$
> 2154	$0.005\,\text{d} \stackrel{\wedge}{=} 7.2\,\text{min}$	$0.0005\,\text{d} \stackrel{\wedge}{=} 43.2\,\text{s}$
> 1000	$0.002\,\text{d} \stackrel{\wedge}{=} 2.88\,\text{min}$	$0.0002\,\text{d} \stackrel{\wedge}{=} 17.28\,\text{s}$
> 464	$0.001\,\text{d} \stackrel{\wedge}{=} 1.44\,\text{min}$	$0.0001\,\text{d} \stackrel{\wedge}{=} 8.64\,\text{s}$
> 215	$0.0005\,\text{d} \stackrel{\wedge}{=} 43.2\,\text{s}$	$0.00005\,\text{d} \stackrel{\wedge}{=} 4.32\,\text{s}$
> 100	$0.0002\,\text{d} \stackrel{\wedge}{=} 17.28\,\text{s}$	$0.00002\,\text{d} \stackrel{\wedge}{=} 1.728\,\text{s}$
≤ 100	$0.0001\,\text{d} \stackrel{\wedge}{=} 8.64\,\text{s}$	$0.00001\,\text{d} \stackrel{\wedge}{=} 0.864\,\text{s}$

4.3 Analysis of identified Manoeuvres

The developed strategy has to be tested with manoeuvres, from which the epochs and, if possible, the thrust vectors $\Delta \vec{V}_M$ are known. The company EUMETSAT operates of the satellites Meteosat-7 (97049B), MSG-1 (02040B) and MSG-2 (05049B) and provides, amongst other data, the epochs of manoeuvres for these three satellites and additionally the thrust vector for Meteosat-7. These data sets can be accessed by e-mail ([EUMETSAT]).

First the parameters of the manoeuvres of the satellite 97047B are analysed. The orbital elements from orbit determinations are propagated to the epochs of the manoeuvres, and the state vectors as well as the difference of the velocity vectors are compared. The difference of the velocity vectors should be equal to the thrust vector. For comparison, the vectorial velocity differences based on circular orbits are also shown the same tables.

Secondly, manoeuvres of the satellite 05049B are investigated, for which only the epochs were provided. The determined differences of the velocity vectors could only be compared to those of the manoeuvres of 97049B, whether they were in same order of magnitude.

4.3.1 Known Manoeuvre Epoch t_M and Thrust Vector $\Delta \vec{V}_M$

In Tab. 4.2, the epochs of seven manoeuvres of 97049B are listed, for which also the thrust vectors were given. The reference frame is an Earth-centred space-fixed Cartesian co-ordinate system. Each manoeuvre is an EWSK manoeuvre.

Table 4.2: Manoeuvres of 97049B with known thrust vectors, provided by EUMETSAT

Date	Time (UT)	t_M (MJD)	Thrust vector $\Delta\vec{V}_M$ $(\mathrm{m\,s^{-1}})$ X	Y	Z
13.09.2011	23:28	55 817.977 778	−0.094	0.102	0.017
11.10.2011	00:58	55 845.040 278	−0.106	−0.003	0.011
15.11.2011	01:58	55 880.081 944	−0.081	−0.100	0.003
20.12.2011	03:28	55 915.144 444	0.031	−0.098	−0.011
31.01.2012	01:58	55 957.081 944	0.085	−0.120	−0.018
20.03.2012	01:58	56 006.081 944	0.149	−0.014	−0.018

The comparison between the backward propagation based on a circular and elliptical orbit, respectively, is shown in Tab. 4.3. The orbit for the forward propagation always bases on an elliptical orbit with the longest possible arcs. The orbits for the backward propagation were determined twice: first, with a circular orbit determination with two tracklets closest to the manoeuvre and thereafter with an elliptical orbit determination consisting of tracklets of the first three nights after the manoeuvre.

Table 4.3: Comparison of velocity differences at the epochs of the manoeuvres between circular and elliptical orbits

Epoch (MJD)	Thrust vectors $(\mathrm{m\,s^{-1}})$ by EUMETSAT			Vectorial velocity differences $(\mathrm{m\,s^{-1}})$ with circular orbit			with elliptical orbit		
	X	Y	Z	X	Y	Z	X	Y	Z
55 817.977 778	−0.09	0.10	0.02	−3.79	4.02	−3.49	−0.14	−0.36	0.02
55 845.040 278	−0.11	0.00	0.01	−0.03	1.99	0.23	−0.10	0.35	0.02
55 880.081 944	−0.08	−0.10	0.00	−0.60	0.48	0.10	−0.02	−0.02	0.00
55 915.144 444	0.03	−0.10	−0.01	−4.64	−1.55	0.37	−0.11	0.07	0.01
55 957.081 944	0.09	−0.12	−0.02	−6.00	−4.54	0.36	0.06	−0.01	−0.01
56 006.081 944	0.15	−0.01	−0.02	0.05	−0.08	−0.01	0.04	0.02	0.00

The results show evidently, that a circular orbit is not sufficient for the propagation, because the calculated velocity differences deviate very much from the values given by EUMETSAT. The differences calculated from backward propagation of the elliptical orbits also show offsets to the true values, but the deviations are smaller. In some cases, neither the order of magnitude nor the sign of a vector component – and therefore the direction of the thrust – is correct.

The comparison of the provided thrust vectors with the determined ones leads to the conclusion, that this method cannot be used for a manoeuvre detection, because the determined velocity differences deviate too much from the given thrust vectors.

4.3.2 Known Manoeuvre Epoch t_M

Another satellite, the AIUB observes regularly, is MSG−2 (05049B). EUMETSAT provides the epochs of each manoeuvre but without the corresponding thrust vectors, which creates a test case for manoeuvres with limited a priori knowledge. If the calculated velocity differences are in the same order of magnitude like the thrust vectors of 97049B, one will get limits for comparisons of vectorial velocity differences of future manoeuvre analyses. In this case, not only EWSK manoeuvres were analysed, but also NSSK manoeuvres and differences in the vector components will be visible.

Table 4.4 shows the epochs of the manoeuvres provided by EUMETSAT and used in this study. The set-up is like the prior investigation. The orbit before the manoeuvre is determined with the longest

possible arc, the orbit thereafter is determined twice: first, a circular orbit with the first two tracklets and then an elliptical orbit with the first three nights after the manoeuvre. The kind of manoeuvre is displayed in the last column.

Table 4.4: Manoeuvres of 05049B, provided by EUMETSAT and comparison of the calculated velocity differences for circular and elliptical orbits

| Date | Time | t_M | Vectorial velocity differences $\Delta \vec{V}_M$ (m s^{-1}) | | | | | | Type |
| | | | with circular orbit | | | with elliptical orbit | | | |
	(UT)	(MJD)	X	Y	Z	X	Y	Z	
08.04.2009	22:28	55 047.936 111	8.16	−22.44	0.05	0.08	−0.22	0.00	EWSK
08.12.2009	03:28	55 173.144 444	8.29	−9.85	0.00	−0.02	0.02	0.00	EWSK
13.04.2010	03:28	55 299.144 444	−0.08	−0.19	0.00	0.01	−0.03	0.00	EWSK
03.08.2010	09:08:08	55 411.380 648	−0.06	−5.89	−8.43	−0.02	0.10	−8.42	NSSK
25.10.2010	14:28	55 494.602 778	0.32	1.23	0.00	0.03	−0.07	0.00	EWSK
01.03.2011	04:13	55 621.175 694	−4.22	−3.79	0.01	0.43	0.07	0.03	EWSK
05.07.2011	10:39:03	55 747.443 785	0.03	−0.01	−6.66	1.14	9.66	−6.22	NSSK
11.10.2011	23:43	55 845.988 194	1.50	0.48	0.01	0.02	0.04	0.00	EWSK
21.02.2012	06:43	55 978.279 861	−0.13	−0.43	−0.01	−0.02	−0.08	0.00	EWSK

As concluded before, the vectorial velocity difference cannot be used for comparison, but both kinds of manoeuvres can be distinguished from each other. The Z-component of the difference vector is much larger for NSSK manoeuvres than for EWSK manoeuvres.

4.4 Detecting Manoeuvres

A discrimination between EWSK and NSSK manoeuvres is possible, using the investigation of the velocity differences. But the manoeuvre epoch must be known. This is normally not the case for an observer, but if two epochs can be defined, between which a manoeuvre might have taken place, an identification of the manoeuvre epoch may be possible. These two epochs may be defined by the osculating epoch of the last orbit before and the first orbit after the manoeuvre, respectively.

4.4.1 Distinction of Manoeuvres from close Conjunctions

Manoeuvres have to be distinguished from close conjunctions of two different objects. In the latter case, there will be an epoch, where the distance between two objects is minimal, but the orbits are unrelated.

Table 4.5 shows the orbital elements of this test case. Both orbital planes are perpendicular to each other, which simplifies the geometry of the problem. The osculating elements corresponds to a certain epoch (MJD = 55 110) and were propagated backwards and forward, respectively, for ten days each. Thereafter, the interval between the epochs (55 100 and 55 120, respectively) was scanned and the distance between the radius vectors as well as the velocity vectors were calculated.

Figure 4.3 shows the distance and the angle between the velocity vectors over time between both radius vectors. At the epoch of the close conjunction, MJD = 55 110, which is represented by the red solid line in the Fig. 4.3(a) and 4.3(b), both radius vectors are closest to each other, but still about 500 km. Like constructed, the angle between both orbits is 90°.

This test provided an illustration of the problem: close conjunctions between objects on orbits, which deviate significantly from each other, will not be detected as manoeuvres. Close conjunctions between
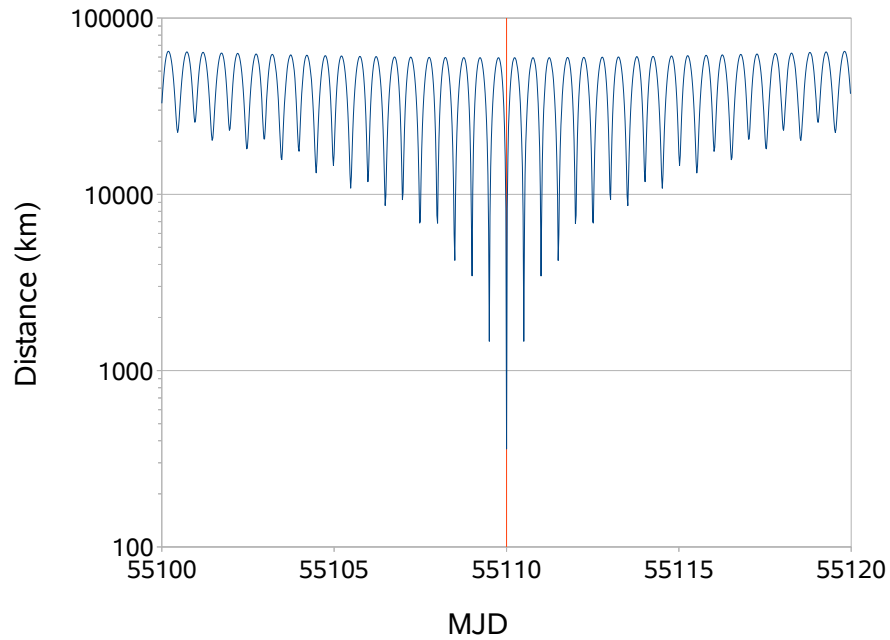
(a) Distance
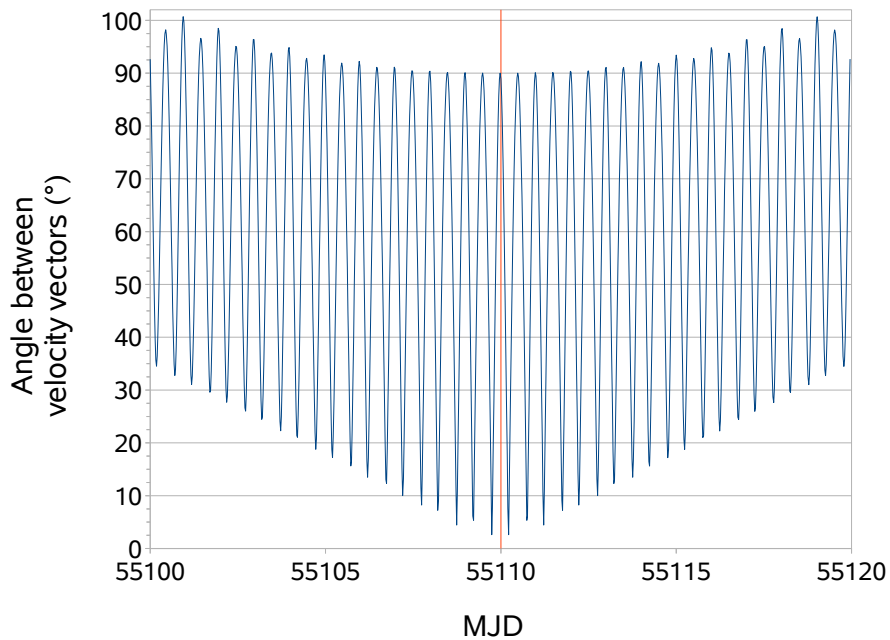
(b) Angle between the velocity vectors

Figure 4.3: Results from propagating orbital elements backwards and forward, respectively; close conjunction without manoeuvre

Table 4.5: Basic orbital elements for the test on uniqueness

| | Orbit for propagation into | |
	the future	the past
Osculating Epoch (MJD)	55 100.00	55 120.00
Semi-major axis (km)	42 560.45	42 164.46
Eccentricity	0.0999	0.1001
Inclination (°)	89.991	0.025
RAAN (°)	0.012	80.897
Argument of perigee (°)	−0.075	−80.764
Time since passage of perigee (s)	−9875.2	−2411.9

objects on similar orbits might be detected as manoeuvres, if the angle between both orbital planes is smaller.

4.4.2 Distinction of Manoeuvres from Time Intervals without Manoeuvres

If the procedure is applied to two epochs, between which no manoeuvre has taken place, a distinction from manoeuvres must be possible. Two element sets of the same orbit are taken and the time interval between them is scanned for manoeuvres. Theoretically, both orbital planes should be identical, but in practice there will be differences due to uncertainties in orbit determination, the used propagation model and numerical effects. To ensure identical orbital planes, one element set is propagated into the future for 20 d and a scan was performed between both epochs.

In Tab. 4.6, there are both element sets used for this test and in Fig. 4.4(a) and 4.4(b) the distance between both radius vectors and the angle between the velocity vectors over time, respectively. A variation of the distance is visible, but the deviation between the positions of both radius vectors is always smaller than 1000 m. There is a minimum at epoch 55 211.018 with a minimum distance of about 4 m. This epoch is marked with a vertical red line. In this case, not only the difference between both radius vectors has a minimum, but also the angle between both velocity vectors. In the complete interval, the angle never exceeds $1 \times 10^{-3\circ}$ ($\hat{=}3''$). Compared to the previous example, these differences can be neglected, and both orbital planes are identical. One can conclude, that there was no manoeuvre performed within the investigated interval.

Table 4.6: Basic orbital elements for the true positive test

	Orbit for propagation into	
	the future	the past
Osculating Epoch (MJD)	55 200.00	55 220.00
Semi-major axis (km)	42 164.17	42 164.65
Eccentricity	0.1000	0.1006
Inclination (°)	2.500	2.498
RAAN (°)	0.000	0.789
Argument of perigee (°)	0.000	−0.286
Time since passage of perigee (s)	0.0	−4711.3
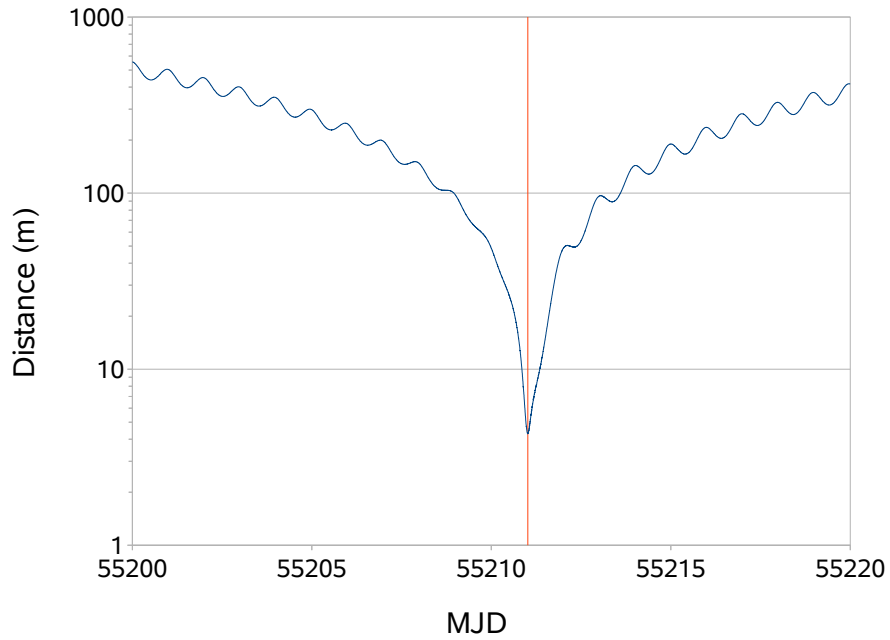
(a) Distance
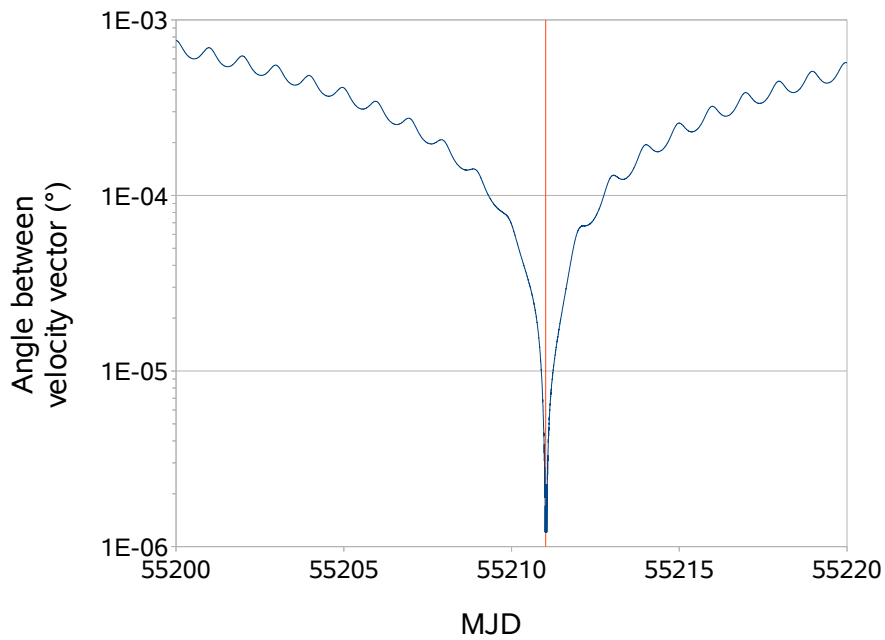
(b) Angle between the velocity vectors

Figure 4.4: Results from propagating orbital elements of identical orbital planes into the past and into the future, respectively

4.4.3 Examples of Manoeuvre Detections

Regarding a priori knowledge of a manoeuvre having taken place, the algorithm is tested, if these manoeuvres can be detected. The already investigated manoeuvres, from which the epochs were given by EUMETSAT, where scanned between the osculating epochs before and after the manoeuvres, respectively.

The procedure was similar to the analysis with given manoeuvre epoch, but now with scanning the entire time interval between the last two observation epochs. The results are presented in Tab. 4.7. The manoeuvre epoch provided by EUMETSAT, as well as the epoch from the scan and the temporal distance between them are displayed. The distance between both radius vectors and the angle between both velocity vectors at the corresponding epochs are determined using the propagated orbits. In the last three columns, there are the vectorial velocity differences (the necessary thrust vector) at the epoch of the manoeuvre. The lines marked with a star ($\star$) are epochs with NSSK manoeuvres. The calculated distances and the angle between the velocity vectors deviate from those of the EWSK manoeuvres, which makes it possible to distinguish both manoeuvre types from each other.

Most manoeuvres were detected around the given epochs with a maximum difference between the estimated and the given epoch of five hours. Three manoeuvres (⑦, ⑪ and ⑬) deviate by 10 hours to 23 hours from the given epochs. The reason for these differences is an unincisive minimum in the distance for the manoeuvres ⑪ and ⑬ (see Fig. 4.6(b)), and that ⑦ is an NSSK manoeuvre. As described above, once every half orbital period, there is a minimum in the distance. Due to numerical effects, the detected manoeuvre epoch differs approximately by a half orbital period.

Unfortunately, no thrust vector was provided by EUMETSAT, so could not be checked, if the order of magnitude and the directions of the components are correct.

The distances between the radius vectors at the manoeuvre epochs are less than 4.5 km, in general, only the already mentioned manoeuvres and the manoeuvres ⑨ and ④, differs by more than 5 km up to approximately 29 km. Manoeuvre ④ is also an NSSK manoeuvre. The largest deviation is explained to the temporal difference of the manoeuvre epoch of manoeuvre ⑦.

The angle between the velocity vectors are below 2.5′ for EWSK manoeuvres, as expected from the thrust vectors. The angles of both NSSK manoeuvres are much larger, approximately of an order of magnitude of one degree.

Table 4.7: Results of the scanning method for manoeuvres

Manoeuvre epoch (MJD)		Temporal	Distance	Angle	Vectorial velocity			
from EUMETSAT	from the scan	difference (min)	ΔR (m)	α_v ($''$)	difference (m s^{-1})			
05049B								
① 55 047.936 111	55 047.942 00	8	2892	21	0.08	−0.02	0.00	
② 55 173.144 444	55 173.067 00	−112	2070	1	−0.01	−0.01	0.00	
③ 55 299.144 444	55 299.116 00	−41	2055	6	0.01	−0.01	0.00	
④ 55 411.380 648	55 411.399 00	26	9759	3571	−0.03	0.10	−8.47	⋆
⑤ 55 494.602 778	55 494.747 00	208	1203	31	0.07	−0.05	0.00	
⑥ 55 621.175 694	55 621.073 00	−148	4471	133	0.31	−0.01	0.04	
⑦ 55 747.443 785	55 747.954 00	735	28 671	2823	−0.08	−0.53	6.68	⋆
⑧ 55 845.988 194	55 845.966 75	−31	237	10	0.02	0.04	0.00	
⑨ 55 978.279 861	55 978.106 00	−250	7051	8	0.01	0.04	0.00	
97049B								
⑩ 55 817.977 778	55 818.165 00	270	2142	82	0.05	−0.19	0.01	
⑪ 55 845.040 278	55 844.097 00	−1359	5761	29	−0.08	0.04	0.00	
⑫ 55 880.081 944	55 880.068 85	−19	434	1	−0.02	−0.02	0.00	
⑬ 55 915.144 444	55 914.665 00	−690	5166	5	−0.04	0.06	0.01	
⑭ 55 957.081 944	55 956.965 69	−167	100	23	0.05	−0.03	0.00	
⑮ 56 006.081 944	56 005.997 00	−122	492	13	0.04	0.01	0.00	

4.4.3.1 Detection of East-West Station-keeping Manoeuvres

The Fig. 4.5 and 4.6 show the results of the EWSK manoeuvres of object 05049B and 97049B, respectively. The distances as well as the angle between the velocity vectors are displayed in logarithmic scale. On the x-axis, the time before and after the manoeuvre is displayed at an interval ranging from 1.5 d before a manoeuvre until 1.5 d thereafter. All graphs are plotted in one diagram for comparison, independently from the actual epoch of the individual manoeuvre.

The distances between the positions were always below 10 km. The minimum distance, which has been detected, was about 100 m. Most minima were distinct apart from the already mentioned manoeuvres ⑪ and ⑬ of 97049B and ⑨ of 05049B.

(a) Manoeuvres of 05049B

(b) Manoeuvres of 97049B
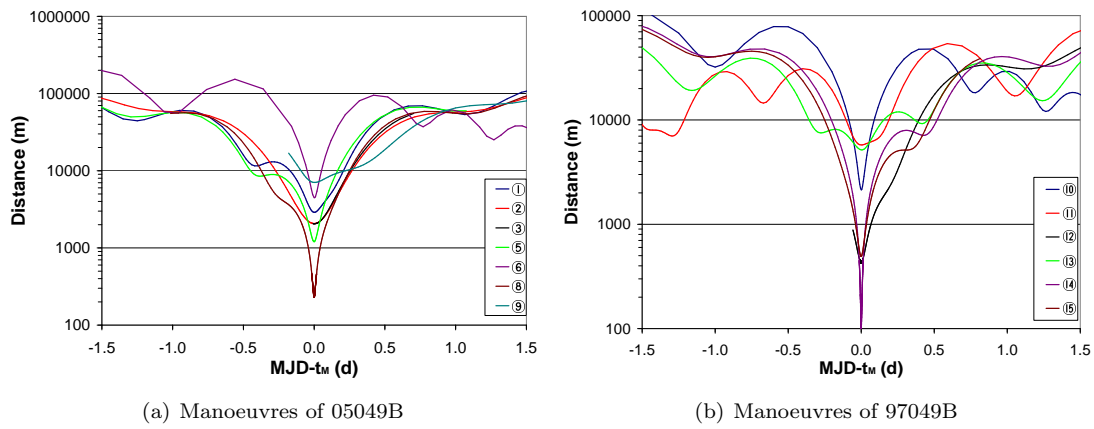
Figure 4.5: Distances at the manoeuvre epochs

The angles between the velocity vectors at the manoeuvre epoch were always below 0.1°. In general, it is not necessary that there is a minimum at the manoeuvre epoch, depending on the location on the orbit. The applied velocity differences are small compared to the orbital velocities and this criterion can be used to confirm an EWSK manoeuvre by excluding angles larger than those present (here 0.1°).

(a) Manoeuvres of 05049B

(b) Manoeuvres of 97049B
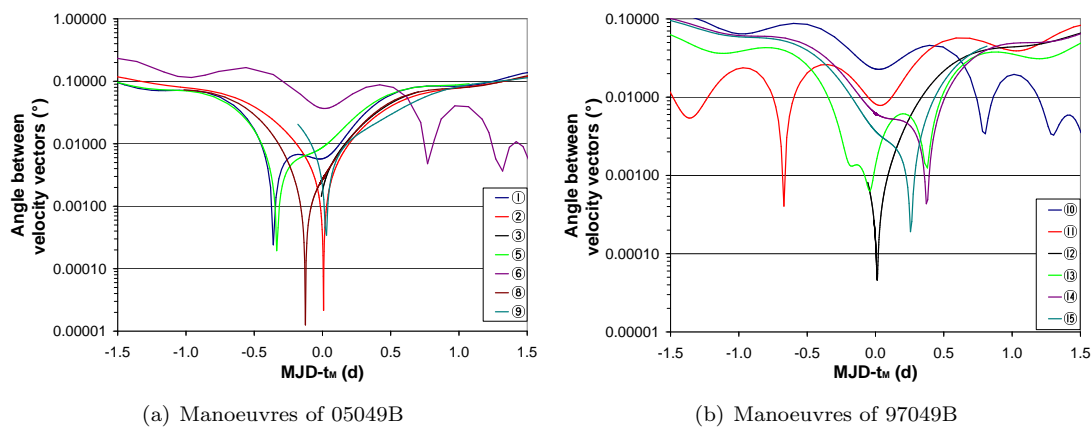
Figure 4.6: Angles between the velocity vectors at the manoeuvre epochs

4.4.3.2   Analysis of North-South Station-keeping Manoeuvres

Unfortunately, data of only two NSSK manoeuvres were available of object 05049B. As pointed out before, the estimation of the manoeuvre epoch of the second manoeuvre led to an epoch, which was approximately 12 hours later than the given epoch.

In both cases, the distance at the manoeuvre epoch was below 50 km. This was much larger than the distances for EWSK manoeuvres. This difference might be used to distinguish both manoeuvre types from each other. In Fig. 4.7, the close conjunctions once every 12 hours are visible, which did lead to problems in determining the exact manoeuvre epoch.

Figure 4.8 shows that the angles between the velocity vectors differed from those of EWSK manoeuvres by orders of magnitude. Here, they had a distinct maximum, which was at 0.78° and 1°, respectively. It could be concluded, that this is a good criterion to distinguish this manoeuvre type from the EWSK manoeuvre.
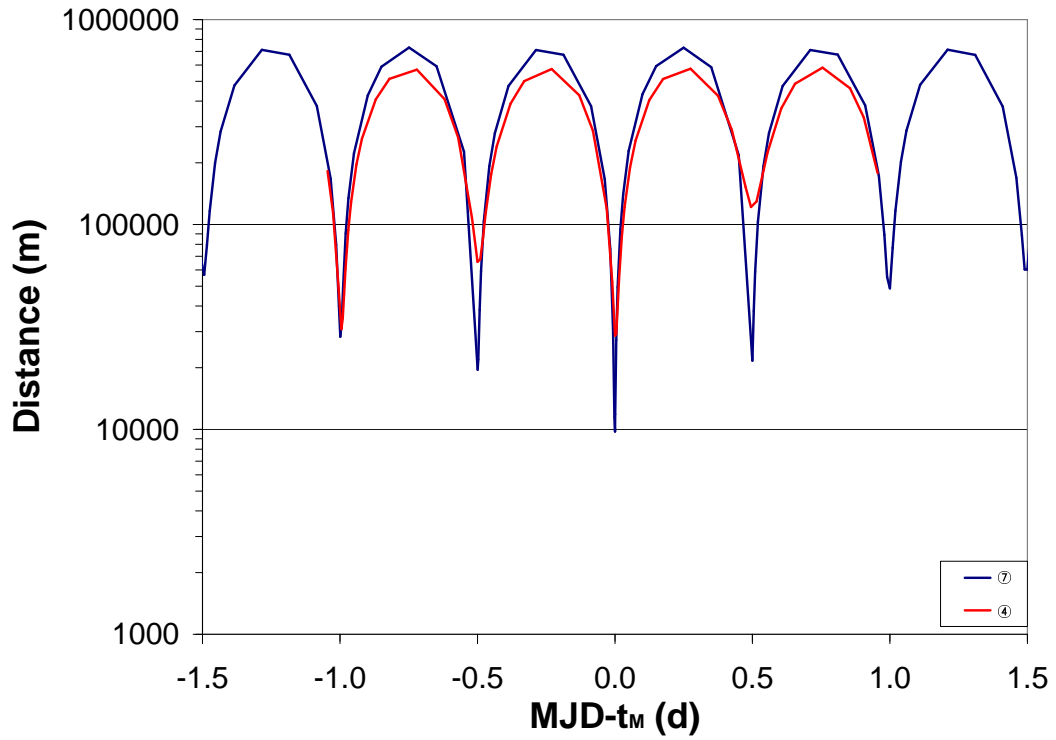
Figure 4.7: Distances at the manoeuvre epochs
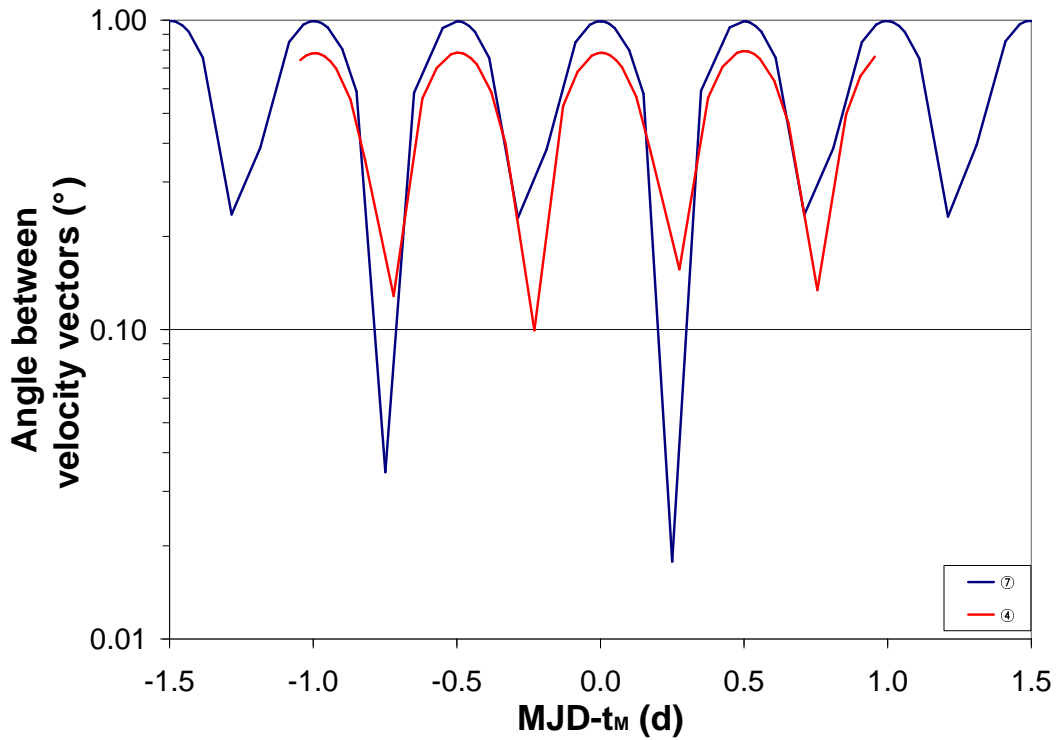
Figure 4.8: Angles between the velocity vectors at the manoeuvre epochs

4.5   Concluding Remarks

In this chapter, the methods to detect manoeuvres, with and without a priori knowledge using optical ground based observations, were investigated. From the observer's point of view, the only available information might be, that an orbit determination was not successful and a manoeuvre is one possible reason.

To search for possible manoeuvre, two elements sets were required: one before the suspected manoeuvre and on thereafter. Both sets were propagated to the manoeuvre epoch and the state vectors were compared. Theoretically, the radius vectors should be equal and the difference of the velocity vectors should be equal to the thrust vector. Due to uncertainties and numerical effects there were differences.

First, manoeuvres were analysed, for which the manoeuvre epoch and the thrust vector were provided by the operator EUMETSAT. Those manoeuvre were East-West station keeping (EWSK) manoeuvres. The vectorial velocity differences were compared to the provided thrust vectors, but it had to be concluded that they could not be used for reliable manoeuvre detection. Additionally, the distance between both propagated positions were determined.

Secondly, manoeuvres were analysed, for which only the manoeuvre epochs were provided. Within this data set, there were two North-South station keeping (NSSK) manoeuvres, and seven EWSK manoeuvres. Here again, the distance between the propagated positions and the vectorial velocity differences were determined and compared to the previous results. Especially the vectorial velocity difference distinguished EWSK manoeuvres from NSSK manoeuvres.

With these results, the given manoeuvres were analysed again, without using a priori knowledge. The time interval between two elements sets were scanned and with set criteria each manoeuvre had to be detected. The defined main criterion was the distance between the radius vectors from both propagations. Other criteria were the order of magnitude of the components of the vectorial velocity difference and the angle between both velocity vectors.

All manoeuvres could be detected with the scanning method. The differences of the manoeuvre epochs, which were estimated and provided, respectively, deviate normally by up to four hours, but in special cases up to one day. These cases were discussed and it could be proven that the minimal distance between both position vectors is insufficient as the only criterion. With more analysed manoeuvres the limits will be calculated more exact. With the calculated vectorial velocity difference a distinction between EWSK and NSSK manoeuvres is possible.

Analysing the AMR Value Variations calculated with SATORB

> In youth we learn, in age we
> understand
>
> —— Marie von Ebner-Eschenbach

As shown before, the area-to-mass ratio (AMR) is another orbit determination parameter. It roughly classifies the space debris: compact, satellite-like objects have AMR values of $1\,\mathrm{m^2\,kg^{-1}}$ and less (low area-to-mass ratio objects, LAMR); large and/or very light, foil-like objects have AMR values of more than $1\,\mathrm{m^2\,kg^{-1}}$ (high area-to-mass ratio objects, HAMR). The latter objects have a large surface area, which is exposed to the radiation of the Sun, compared to their mass. Their orbits are highly influenced by the Solar radiation pressure. The orbital elements show characteristic variations (see [Früh 11]). An AMR value can be estimated by calculating the radiation pressure. It will be shown later that this value must be treated carefully because of possible misinterpretations.

The first discoveries of space debris objects with AMR values higher than preliminary known were made by T. Schildknecht in 2004 ([Schi 04]). A large number of objects was detected, for which significantly high AMR values were estimated. These AMR values were higher than for any other object observed so far. As of December 2011, 46 objects with an AMR value of $1\,\mathrm{m^2\,kg^{-1}}$ or higher could be found using observations of AIUB. Often, a large number of follow-up observations could be made and the orbital elements of these objects could be analysed over a certain time span.

Earlier analyses (see [Musc 10] and building on that, [Früh 11]) showed a variation of the AMR values for several HAMR objects, but the number of observations and the analysed intervals were not as large as in the upcoming analysis. Figure 5.1 shows the results of the object E06321D presented in both publications. The first data set covered approximately 500 days ([Musc 10]). The error bar of the first point is so large, that the variation is hardly visible. The second data set had 1300 days of observations (taken from [Früh 11]) and variation is visible. The second graph shows a variation of about $6\,\%$ (minimum to maximum). However, there are gaps without observations and the error bars of some AMR values are still large.

The object E06321D was also chosen to be in this analysis, because it has a long total arc with observations up to today. It is the only common object analysed in all three studies. The other objects were selected to have a large range of AMR values in the subset and a large number of observations for each object.

It has to be mentioned again, that finding and correcting a software bug is nothing special. But the results of the wrongly determined AMR value variation were the base for several publications focussing on the AMR value variation. Therefore, a presentation of the error and the comparison of the old results to the new ones is justified.
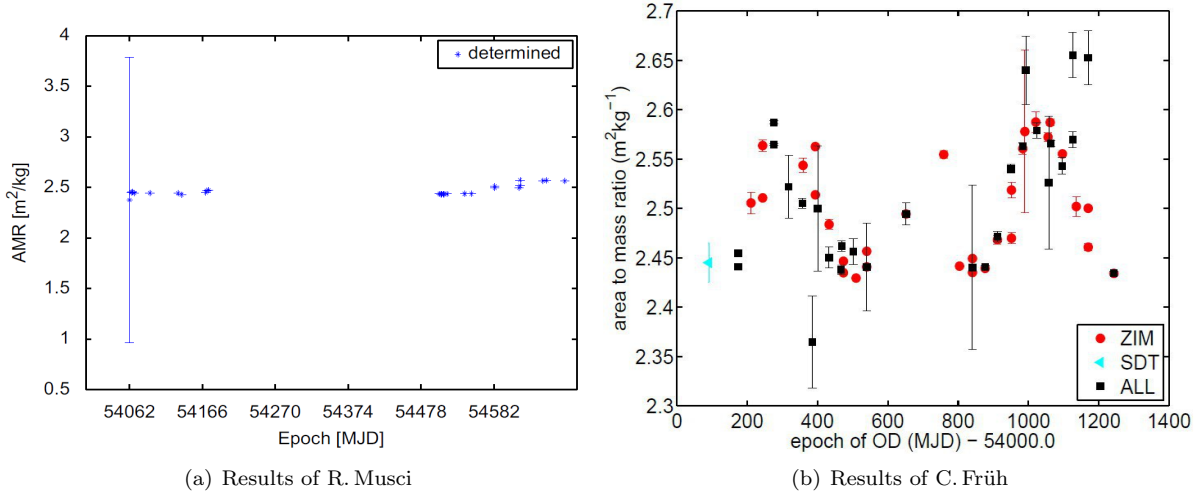
(a) Results of R. Musci

(b) Results of C. Früh

Figure 5.1: AMR values of E06321D from earlier analyses

5.1   AMR Values from Orbit Determinations with SATORB

5.1.1   Estimation of AMR Values

As pointed out before, the estimation of an AMR value differs from the estimation of osculating Keplerian elements in an orbit determination. While the osculating Keplerian elements are estimated for the first or last epoch of the used arc (which can be chosen by the user), the AMR value is averaged over the entire interval. This leads to an important consequence: the shorter the used arc is, the better the current AMR value is represented. On the other hand, if the used arc is large, the estimated AMR value will represent a mean AMR value. If a graph shows no structures apart from scattering, one can conclude that there are no variations with periods larger than the used arc length. With this method it is not possible to give statements about variations with shorter periods.

5.1.2   Analysing the Subset

The objects analysed in this chapter have observations distributed over approximately one year and more. I chose objects with mean AMR values between about $0.03\,\mathrm{m^2\,kg^{-1}}$ and approximately $29\,\mathrm{m^2\,kg^{-1}}$. Table 5.1 shows the objects analysed in this study sorted by their mean AMR value, together with total arc length of each object and the number of nights each object was actually observed. The numbers in brackets represent the uncertainties of the last digits at $68\,\%$ confidence level.

The number of AMR values is equal to the number of orbits, which were determined. For each night with observations an orbit determination is performed with as many observations of preceding nights as possible. The constraints for the quality of an orbit is, like before, the RMS of the residuals, $\mathrm{RMS} \leq 2''$. Additionally, the uncertainty of the scaling factor for the AMR value had to be smaller than $20\,\%$ of the scaling factor itself, which leads to small uncertainties of the AMR value, consequently.

Let AMR_i be the AMR values of the individual orbits, which could be determined. I assume that an orbit determination with a long arc length Δt_i leads to an AMR value, which is close to the mean AMR value, short time variations will be suppressed. The average of all individual AMR values, $\overline{\mathrm{AMR}}$, is an

Table 5.1: Results of orbit determinations, sorted by mean AMR value; the numbers in brackets are the uncertainties of the last digits on 68 % confidence level

Object	Mean AMR $\mathrm{m^2\,kg^{-1}}$	First epoch MJD	Last epoch MJD	Total arc length d	Number of nights with observations
Z09338F	0.0282(3)	55169.93	55921.80	751.87	137
05049E	0.0501(21)	53733.90	55867.97	2134.07	120
05049F	0.076(4)	55368.93	55887.75	518.82	27
E06327E	0.581(6)	54062.84	55921.80	1858.96	121
E07311D	1.374(10)	54411.92	55629.11	1280.19	70
E06321D	2.510(5)	54057.15	55945.95	1888.80	173
E09293A	4.235(19)	55124.94	55623.93	498.99	30
E07047A	4.827(17)	54847.86	55923.20	1075.34	58
E10245A	13.37(4)	55442.12	55686.74	244.62	27
S95300	28.77(8)	55302.63	55708.93	406.30	63

arc length-weighted average. So AMR values based on long used arcs got high statistical weight

$$\overline{\mathrm{AMR}} = \frac{\sum_{i=1}^{n} \Delta t_i \cdot \mathrm{AMR}_i}{\sum_{i=1}^{n} \Delta t_i} \tag{5.1}$$

with the standard deviation $\sigma_{\overline{\mathrm{AMR}}}$

$$\sigma_{\overline{\mathrm{AMR}}} = \sqrt{\frac{\sum_{i=1}^{n} \Delta t_i \cdot \left(\mathrm{AMR}_i - \overline{\mathrm{AMR}}\right)^2}{(n-1) \cdot \sum_{i=1}^{n} \Delta t_i}}. \tag{5.2}$$

The Fig. 5.2 show the graphs of the estimated AMR values of each object after each orbit determination, where the dots represent the estimated AMR values. As one can see in the collection of graphs, for mean AMR values higher than $2\,\mathrm{m^2\,kg^{-1}}$ (see Fig. 5.2f) to j)) there is a significant sinusoidal variation. For objects with lower mean AMR values (Fig. 5.2a) to e)), white noise or another kind of variation of the AMR value seems to be dominating.
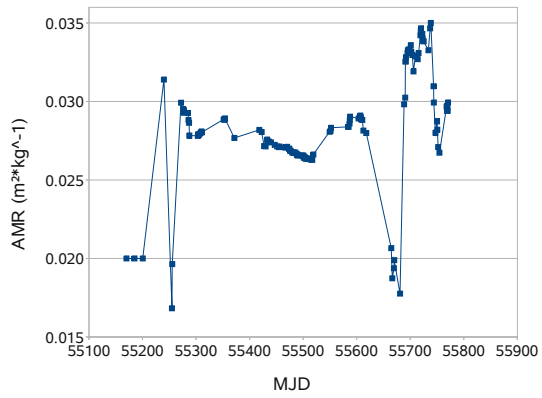
(a) Z09338F, mean AMR=$0.0282\,\mathrm{m^2\,kg^{-1}}$
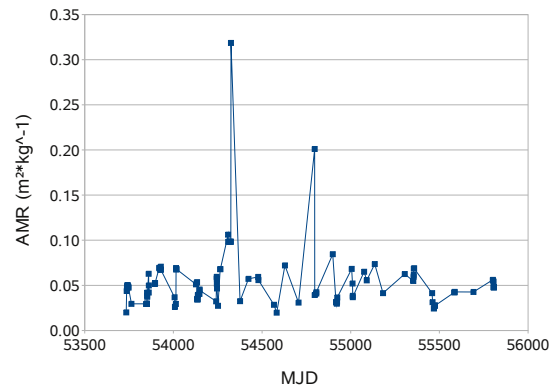
(b) 05049E, mean AMR=$0.0501\,\mathrm{m^2\,kg^{-1}}$
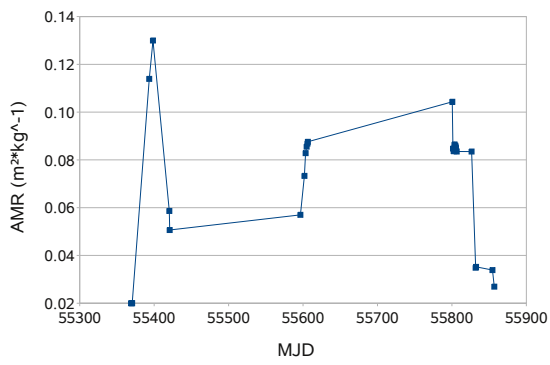
(c) 05049F, mean AMR=$0.076\,\mathrm{m^2\,kg^{-1}}$
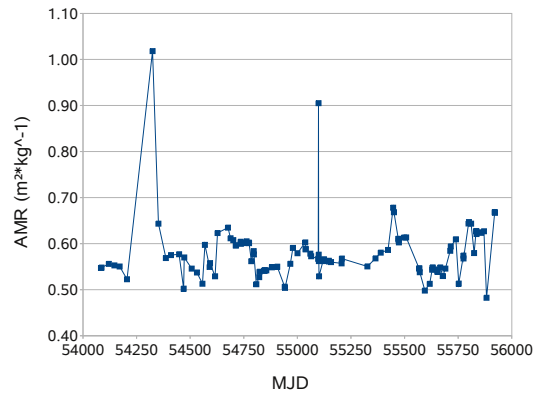
(d) E06327E, mean AMR=$0.581\,\mathrm{m^2\,kg^{-1}}$

Figure 5.2: AMR value variations over time of selected objects
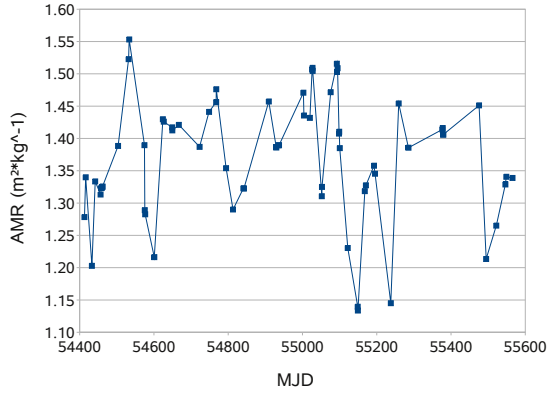
(e) E07311D, mean AMR=1.377 m^2 kg^{-1}
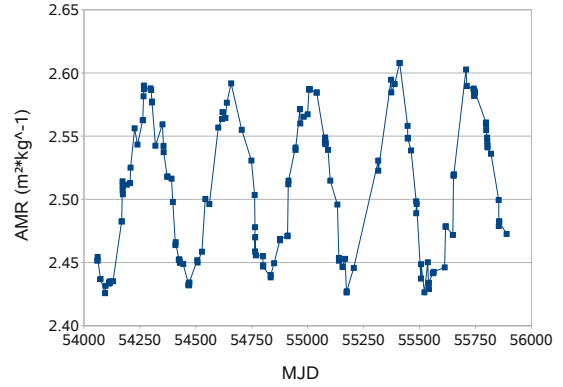
(f) E06321D, mean AMR=2.510 m^2 kg^{-1}
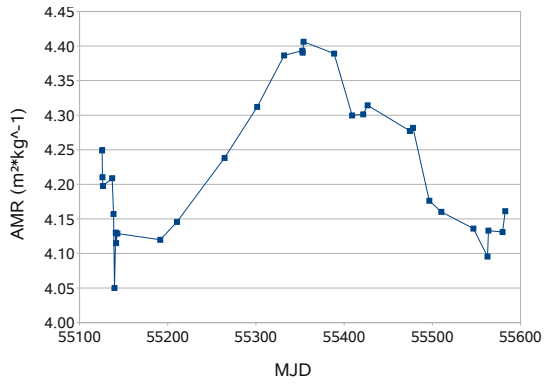
(g) E09293A, mean AMR=4.235 m^2 kg^{-1}
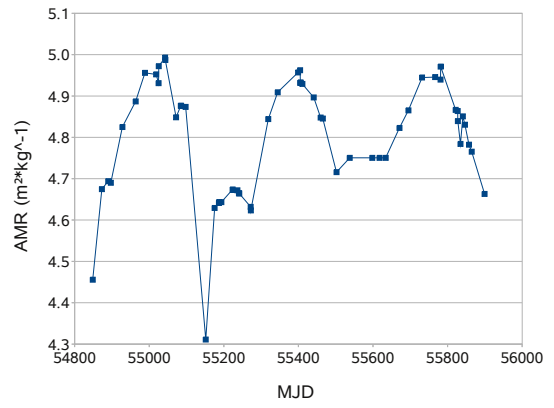
(h) E07047A, mean AMR=4.814 m^2 kg^{-1}
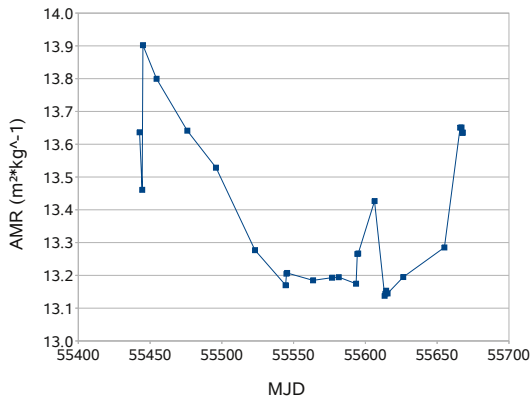
(i) E10245A, mean AMR=13.37 m^2 kg^{-1}
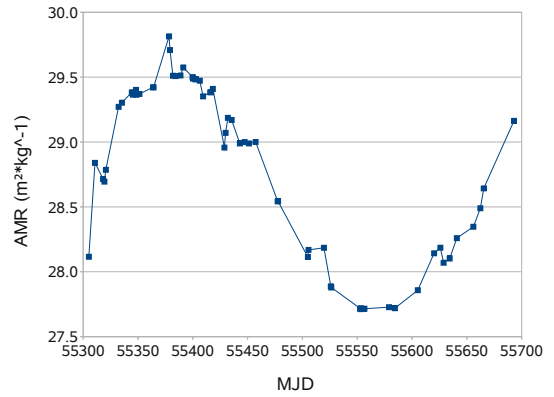
(j) S95300, mean AMR=28.77 m^2 kg^{-1}

Figure 5.2: AMR value variations over time of selected objects (cont.)

5.2   Analytical Results

The variations were analysed analytically. As a first step a function was fitted to the data and the estimated parameters for each object were compared.

5.2.1   AMR Value Variation of the HAMR Objects

An expression with a cosine function

$$y(t) = b \cdot \left(1 - c \cdot \cos \left(\frac{2\pi}{T_0} \cdot (t - t_0) \right) \right)^2 \tag{5.3}$$

was fitted to the data points of the objects with the highest AMR values, where the parameter y stands for the AMR value, t for the epoch, b for the mean AMR value, c for the amplitude and T_0 for the period of the oscillation. Table 5.2 shows the results of the fits performed with *gnuplot*. In brackets there are given the uncertainties for the last digits at 68 % confidence level.

Table 5.2: Analytical results of the cosine fits for the AMR value of HAMR objects

Object	Mean AMR b m^2 kg^{-1}	Amplitude c m^2 kg^{-1}	Period T_0 d	Phase t_0 MJD	RMS of the fit
E07311D	1.377(11)	0.0213(8)	362(19)	55556(44)	0.084
E06321D	2.5106(10)	0.0151(3)	365.0(7)	55562.6(1.8)	0.012
E09293A	4.258(8)	0.0155(15)	376(13)	55557(11)	0.038
E07047A	4.786(9)	0.0182(14)	371(5)	55572(6)	0.067
E10245A	13.43(4)	0.0105(15)	270(40)	55578(7)	0.117
S95300	28.573(18)	0.01625(5)	362(5)	55569.7(2.3)	0.135

The individual fits themselves do not give any hint of what origin those variations might be. But looking at the parameters in Tab. 5.2, one can see that they agree very well in most cases. The estimated mean AMR value is in good agreement with those of Tab. 5.1.

The phases t_0 of the cosine fits mostly agree within the uncertainties. This leads to the assumption that the objects are affected simultaneously and that the effect leading to the sinusoidal variation is not object specific.

Although the periods T_0 show large differences they agree within the uncertainties. One might conclude that each period is related to one year.

The amplitudes c range between 0.0105 and 0.0213, but these are extreme cases of a short total arc (E10245A) and a low mean AMR value (E07311D), respectively. The data set of the object E10245A covers approximately 245 days, which is less than the period, which could be estimated. Therefore, the estimated parameters are uncertain. The other amplitudes range between 0.0151 and 0.0182. They do not agree within their uncertainties but this may be explained by the fact that the effect consists of a non-object-specific part, which results in an equal order of magnitude of all amplitudes, and a specific part, which leads to the deviation from a fixed value.

The cosine curves for the HAMR objects are plotted in Fig. 5.3, the dots are again the estimated data from Fig. 5.2, the black line represent the fits. It is to see that the AMR values of the object E07311D hardly follow the fit, another kind of AMR value variation is more dominant than the sinusoidal variation.

The amplitude c and the period T_0 led to the assumption that the sinusoidal trend of the data points might be related to the orbit of the Earth, which will be investigated in the following section. If this assumption is true, then a wrong model of the Solar radiation pressure might be applied.
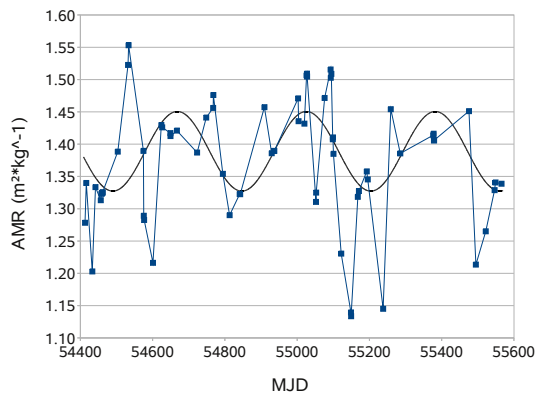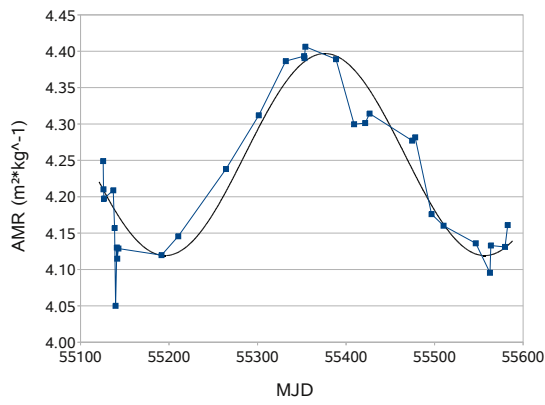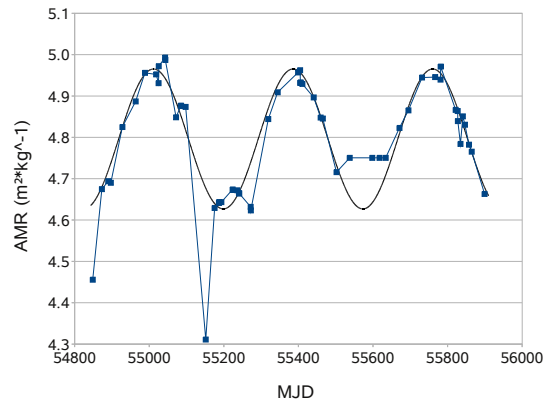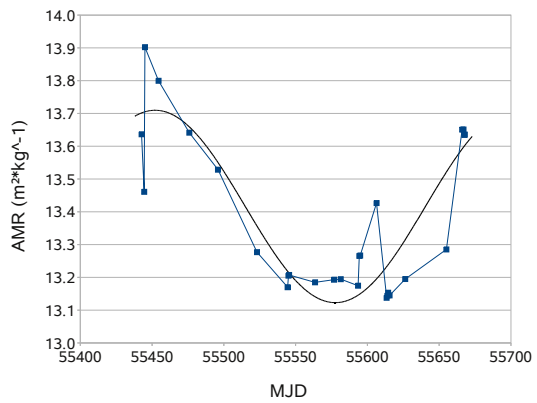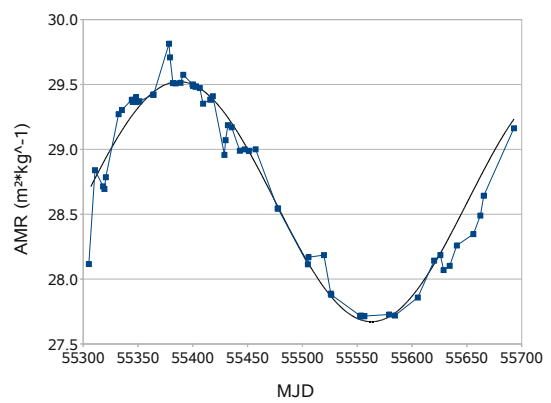
(a) E07311D
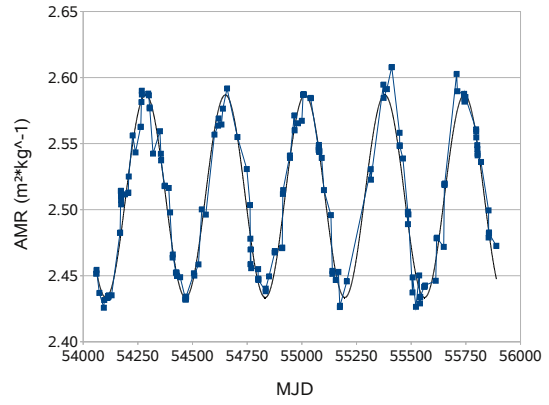
(b) E06321D

(c) E09293A

(d) E07047A

(e) E10245A

(f) S95300

Figure 5.3: Graphs of the AMR value variations of selected HAMR objects with fitted curves

5.2.2 The Distance between the Sun and the Earth

The orbit of the Earth around the Sun is an ellipse and the distance r between the Sun and the Earth varies with time. This variation can be displayed in first order approximation as:

$$r(t) = a \cdot \left(1 - \varepsilon \cos \left(\frac{2\pi}{T_{\oplus}} \left(t - T_{\Pi} \right) \right) \right) \tag{5.4}$$

In this equation, $r(t)$ can be given in Astronomical Unit (AU). The parameter a is the semi-major axis of the orbit of the Earth around the Sun, ε is the eccentricity of the orbit, $T_{\oplus}$ is the anomalistic year ($T_{\oplus} = 365.259\,635\,864$ d, (J2000.0)) and T_{Π} the epoch of a passage through the perihelion. The parameters used for the orbit of the Earth around the Sun are given in Tab. 5.3.

Table 5.3: Parameters of the orbit of the Earth (J2000.0), [NASAa]

Parameter	Value
Semi-major axis a	1.000 000 11 AU
Eccentricity ε	0.016 710 22
Longitude of the perihelion ν_{Π}	102.947 19°
Mean longitude at epoch ν_0	100.464 35°
Mass of the Sun $M_{\odot}$	$1.988\,92 \times 10^{30}$ kg

The Modified Julian Date of the standard epoch J2000.0 is 51544.5 ($\hat{=}\,T_0$), so the epoch of the passage through the perihelion can be calculated with the values given in the table above. The longitude of the perihelion ν_{Π} and the mean longitude at epoch ν_0 are measured from the position of the Sun, and so is the true anomaly $\mathcal{T}$. Angular differences are therefore equally measured and do not have to be converted. As commonly defined, the perihelion represents $\mathcal{T}_{\Pi} = 0°$, the difference in true anomaly is then $\Delta\mathcal{T} = 100.464\,35° - 102.947\,19° = -2.482\,84°$. Afterwards the epoch of the passage through the perihelion can be calculated (taken from [Beut 05]):

$$\sqrt{\frac{GM_{\odot}}{a^3}}(T_0 - T_{\Pi}) = 2\arctan\left(\sqrt{\frac{1-\varepsilon}{1+\varepsilon}} \cdot \tan\left(\frac{\Delta\mathcal{T}}{2}\right) \right) - \frac{\varepsilon\sqrt{1-\varepsilon^2}\sin(\Delta\mathcal{T})}{1+\varepsilon\cos(\Delta\mathcal{T})}$$

$$T_{\Pi} \approx 51\,546.935\,75$$

This Modified Julian Date corresponds to a passage through the perihelion on January 3, 2000 at 22:27 UTC. Using the anomalistic year given above, the passage through the perihelion in 2011 becomes $T_{\Pi} \approx 55\,564.791\,74$, which correspond to January 3, 2011 at 19:00 UTC.

5.2.3 Comparison with the AMR Value Variation

The following table combines the values in the Tab. 5.2 and 5.3 with each other.

Object	Factor[1]	Amplitude c $\mathrm{m^2\,kg^{-1}}$	Period T_0 d	Phase t_0 MJD	RMS of the fit
E07311D	1.377(11)	0.0213(8)	362(19)	55556(44)	0.084
E06321D	2.5106(10)	0.0151(3)	365.0(7)	55562.6(1.8)	0.012
E09293A	4.258(8)	0.0155(15)	376(13)	55557(11)	0.038
E07047A	4.786(9)	0.0182(14)	371(5)	55572(6)	0.067
E10245A	13.43(4)	0.0105(15)	272(38)	55578(7)	0.117
S95300	28.573(18)	0.01625(5)	362(5)	55569.7(2.3)	0.135
Orbit	1.000	0.01671022	365.259635864	55564.79174	

One may conclude that the fit parameters agree with the orbit parameters within the uncertainties. So, the variation of the AMR values over time is related to the distance variation between the Earth and the Sun. The AMR values have to be compared to the square of the distance function (5.4), with the parameters of the orbit of the Earth to proof this statement:

$$r^2(t) = a^2 \cdot \left(1 - \varepsilon \cos \left(\frac{2\pi}{T_\oplus} \left(t - T_\Pi \right) \right) \right)^2 \tag{5.5}$$

The AMR values are normalised and can be shown together in one single figure (Fig. 5.4) by dividing them through the fit parameter b (mean AMR value) for each object. The black solid line represents the distance squared between the Earth and the Sun. The majority of data seems to follow the black line, apart from two objects. The data of E10245A in light blue lie above that curve. This is due to the small number of observation (27 nights with observations) with a total arc length of approximately 245 d; the mean AMR value is underestimated. More observations might have made it possible to estimate the mean AMR value more accurately. Nevertheless, they follow the cosine curve trend. The data of E07311D in dark green do not follow the cosine curve. The mean AMR value is the smallest of this subset and another kind of variation is dominating.

---

[1]For the AMR values the factor is the parameter b in $\mathrm{m^2\,kg^{-1}}$, for the orbit of the Earth it is the parameter a in AU.
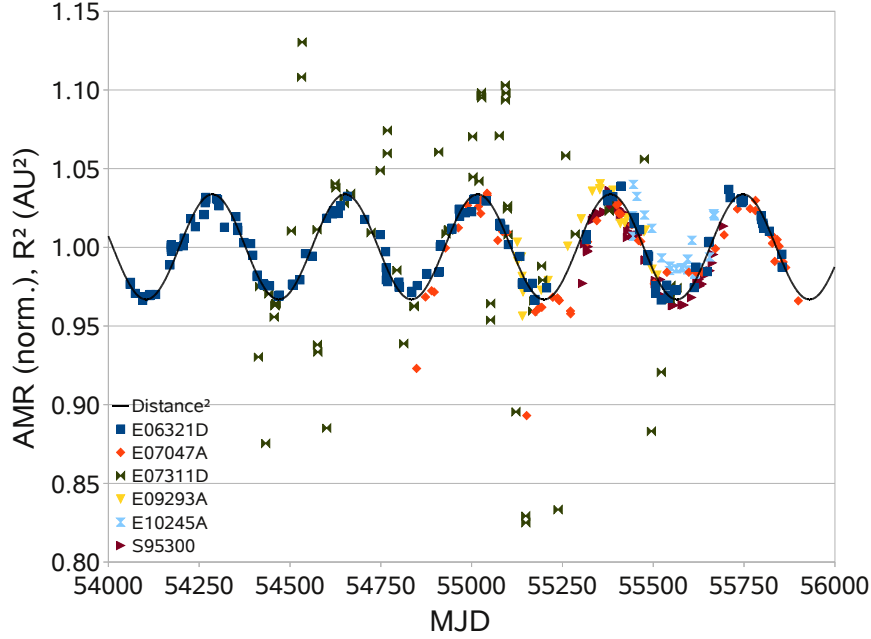
Figure 5.4: Normalised AMR values (coloured symbols) compared to the square of the radius vector

I chose again the Pearson correlation coefficient

$$\varrho_{M,F} = \frac{\text{cov}(X_M, X_F)}{\sigma_{X_M} \cdot \sigma_{X_F}},$$

where $\text{cov}(X_M, X_F)$ is the covariance between the measured data set X_M and the fitted one X_F. I expect $\varrho_{M,F}$ to be close to $+1$, which is a hint for a good correlation between the measured and the fitted data. The characteristics of the Pearson correlation coefficient were presented in more detail in subsection 2.3.4.

A correlation coefficient close to $+1$ only states that there is a linear correlation between two distributions, in an $X_M - X_F$-diagram the data will form a line. The slope of the regression line should be close to $+1$ and the intercept should be close to zero. Then, the measured data can perfectly represented by the fit. In practice the three values will deviate from the theoretic values.

Table 5.4: Results of the correlation between the measured and fitted data for the HAMR objects

Object	Pearson correlation coefficient $\varrho_{M,F}$	Slope	Intercept
E06321D	0.977	0.906	0.094
E09293A	0.913	0.959	0.039
E07047A	0.881	1.086	−0.085
E10245A	0.861	0.840	0.168
S95300	0.941	0.909	0.092

The results presented in Tab. 5.4 confirm the assumption that the variations of the AMR values are related to the square of the distance function (5.4). The reason might be a wrong model of the DRP which was applied or an error in the source code. Therefore the source code of SATORB had to be searched for the application of the DRP.

5.3   Bug Fixing in the Source Code of *SATORB*

The analyses in this chapter based only on the results. The connection to the programs and subroutines used for an orbit determination has not been established yet. The source code of *SATORB* had to be investigated, whether the model is wrong or there is an error in the application of the model.

Only in two subroutines called by SATORB the model for the DRP is used and the modifications could easily be done. The extract below show the lines where the model is applied.

```
DO K=1,3
  DF=-SCLDRP*SOLCON*CRAD/2*QDMRAD*(1.49597870D11/SUN(4))**2*(SUNPOS(K)-XV(K))/RSS
           *(1.49597870D11/RSS)**2
    F(K)=F(K)+DF
ENDDO
```

The terms `SUN(4)` and `RSS` are almost identical: the first represents the distance between the Sun and the Earth, the latter between the Sun and the observed object. The first factor is the explanation for the variation with the period of about one year as it refers to the motion of the Earth around the Sun and does not refer to the object.

The compensation for the distance variation between the Earth and the Sun was unnecessarily applied and had to be removed. Then same lines from above look now like:

```
SCLFAC=(1.49597870D11/RSS)**2
DO K=1,3
  DF=-SCLDRP*SOLCON*CRAD/2*QDMRAD*(SUNPOS(K)-XV(K))/RSS*(1.49597870D11/RSS)**2
    F(K)=F(K)+DF
ENDDO
```

It has to be said again that presenting the changed line was not the motivation behind the analysis and this chapter, but the changed determination leads to different AMR values without the annual signal.

5.4   AMR Value Analysis after the Correction of *SATORB*

After the correction of the subroutines the analysis was performed again to display the differences and gain results which represent the truth more likely.

The orbits were determined identically to the first run and the results are comparable. The Fig. 5.5a) to h) show the distribution of AMR values of the same subset of objects after the correction. The newly estimated AMR values are printed in blue, the old ones for comparison in grey.

Table 5.5 compares the newly calculated mean AMR values to the old ones. The standard deviation is of course lower for the new averages, because the sinusoidal variation led to an overestimated standard deviation. The averages themselves do not differ much, apart from the one of object E10245A. As mentioned before, the observations of this object did not cover one year.

5.4.1   Low Area-to-Mass Ratio Objects

The AMR value variation due to the distance variation was not dominant for LAMR objects, so I expected the newly determined values to be similar to the old ones. Nevertheless, some peaks could be reduced (like in the graph of 05049E around MJD=54 300) or vanished completely (same object around MJD=54 750 and E06327E around MJD=54 250 and MJD=55 100, respectively). These effects are related to longer arc length used in the orbit determination. Other AMR values hardly changed, like those of object 05049F.

(a) Z09338F, mean AMR=0.026 35 m^2 kg^{-1}

(b) 05049E, mean AMR=0.0470 m^2 kg^{-1}

(c) 05049F, mean AMR=0.070 m^2 kg^{-1}

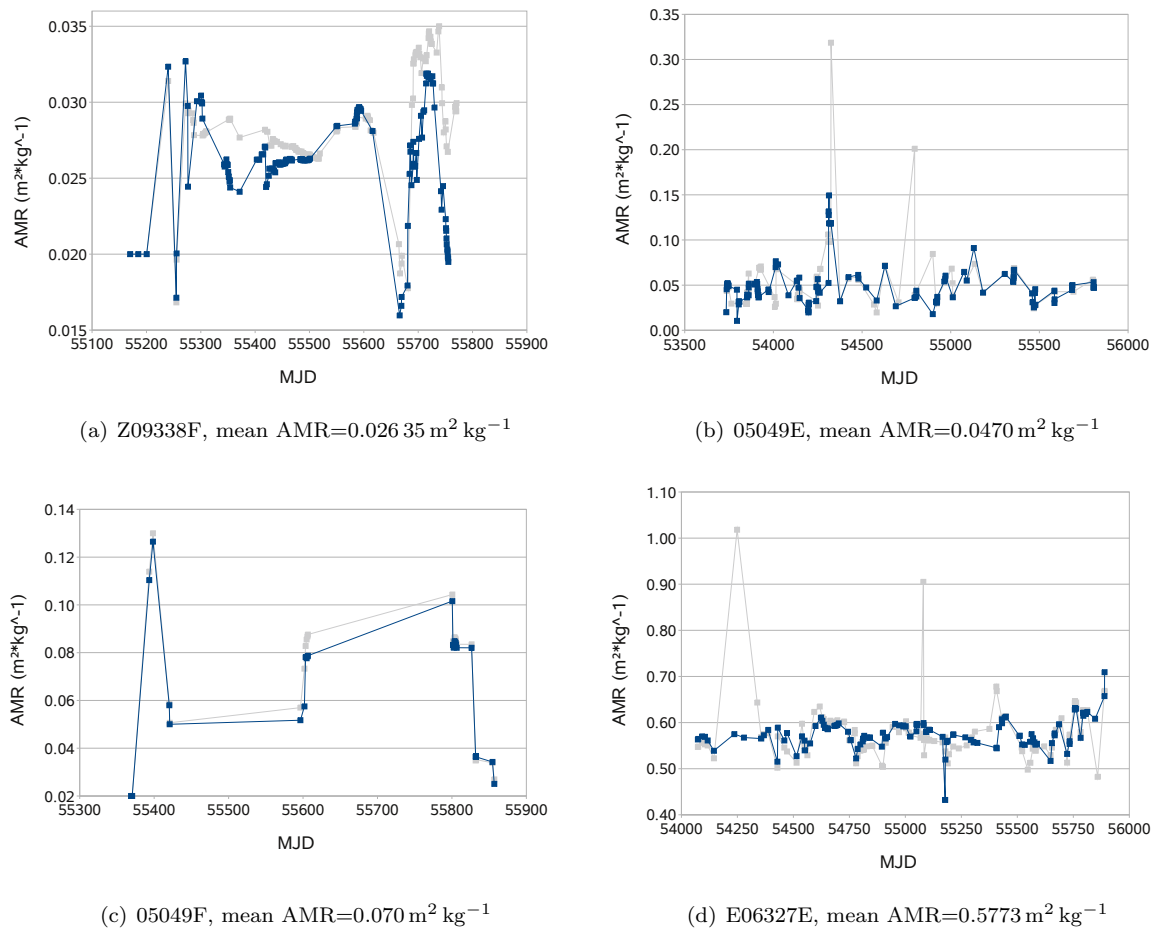(d) E06327E, mean AMR=0.5773 m^2 kg^{-1}

Figure 5.5: Newly determined AMR values over time; blue: after the correction of SATORB; grey: the old data for comparison (cf. Fig. 5.2)

**Table 5.5:** Comparison between the estimated mean AMR values before and after the correction of SATORB, respectively

Object	Mean AMR value (m^2 kg^{-1})	
	before	after
Z09338F	0.0282(3)	0.026 35(24)
05049E	0.0501(21)	0.0470(14)
05049F	0.076(4)	0.070(4)
E06327E	0.581(6)	0.5773(25)
E07311D	1.374(10)	1.378(8)
E06321D	2.510(5)	2.5115(3)
E09293A	4.235(19)	4.252(6)
E07047A	4.827(17)	4.792(6)
E10245A	13.37(4)	13.616(25)
S95300	28.77(8)	28.576(16)
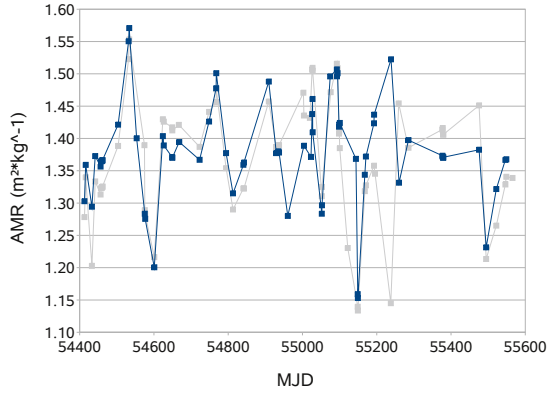
(e) E07311D, mean AMR=1.378 m^2 kg^{-1}
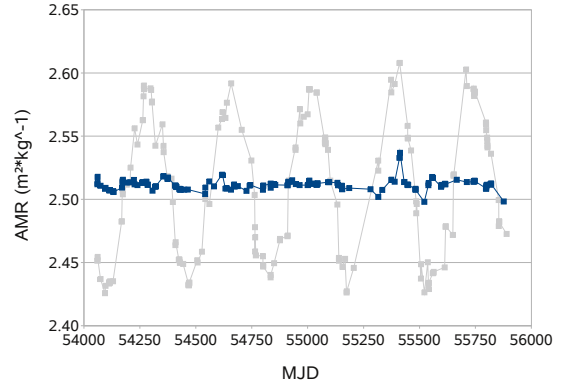
(f) E06321D, mean AMR=2.5115 m^2 kg^{-1}
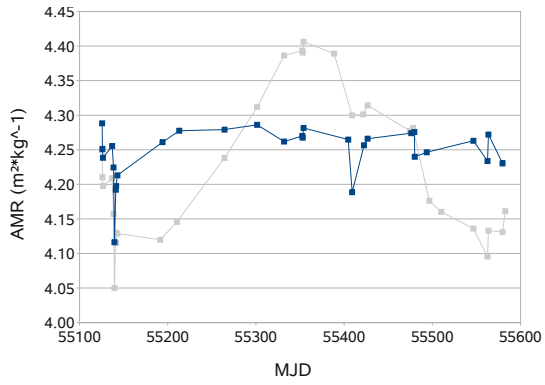
(g) E09293A, mean AMR=4.252 m^2 kg^{-1}
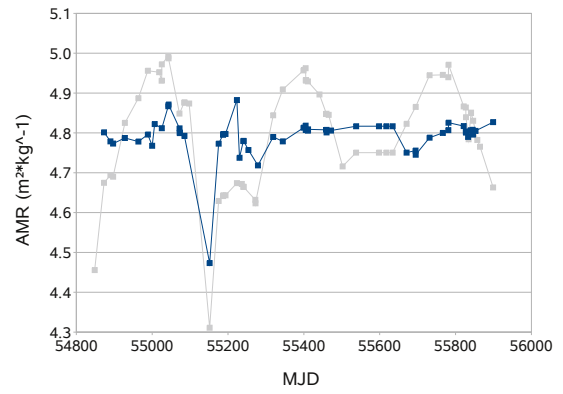
(h) E07047A, mean AMR=4.792 m^2 kg^{-1}
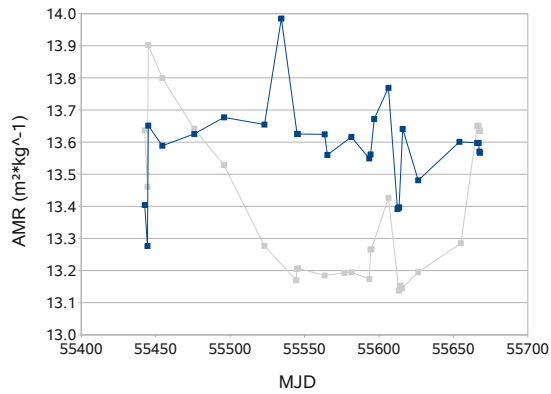
(i) E10245A, mean AMR=13.62 m^2 kg^{-1}
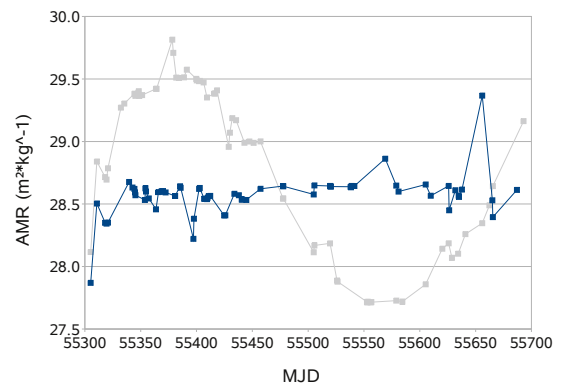
(j) S95300, mean AMR=28.58 m^2 kg^{-1}

Figure 5.5: Newly determined AMR values over time (cont.)

5.4.2   High Area-to-Mass Ratio Objects

Referring to Fig. 5.5e) to j), the sinusoidal variation has vanished, the graphs are flat. But some significant features, which are in prior graphs, are also in the corrected ones, like the peak in the graph of object E10245A around MJD=55 600. These may be true variation of the AMR value between these epochs.

Some more peaks in the graph of E10245 around MJD=55 530 and of S95300 around MJD=55 650 occur, respectively. Those may be true variation, that were suppressed in the prior analyses. Unfortunately, it is also possible that those features occur when the used arc was shortened significantly. Then the estimated AMR value does not represent necessarily the mean AMR value.

5.5   Concluding Remarks

In this chapter I presented an analysis concerning AMR value variations. I selected ten objects with a range of mean AMR values between $0.03\,\mathrm{m^2\,kg^{-1}}$ and $28.58\,\mathrm{m^2\,kg^{-1}}$ supported by numerous observations. Orbits were determined for each object with a maximum of observation and a minimum of dynamical parameters; the DRP-parameter was always estimated.

The data points of the AMR values of the HAMR objects followed a sinusoidal trend. The parameters of the cosine function led to the assumption that the trend was related to the distance between the Earth and the Sun, and therefore to orbit of the Earth. The investigation of the source code of *SATORB* confirmed this assumption and the false expression was deleted.

After debugging each object was analysed again, with the same procedure as before. The oscillation with the one year period vanished for the HAMR objects, as expected. The AMR values of the LAMR objects were similar to the prior analysis, but with a lower uncertainty of the mean AMR value.

Chapter 6

Conclusions

The main topic of this dissertation thesis was the built-up of an orbital elements catalogue of objects in the geostationary ring and the Medium Earth Orbit region. This included planning the observations and processing procedures thereafter. The telescope ZimSMART operated only in survey-only mode, which means that objects were not observed on purpose but regions of the sky were surveyed. Consequently, all observed objects were unknown and had to be identified afterwards.

Different survey scenarios were presented to observe the geostationary ring. The chosen survey scenario consisted of four declination stripes at fixed right ascensions, which were arranged in two pairs. Due to the rotation of the Earth around the Sun the stripes had to be adjusted twice a month to ensure that at least one pair is visible the entire night. The region around the galactic plane was also avoided, because of the large number of catalogue stars, whose identification would have been very time consuming when calculating and extracting the objects' positions.

For the observations of the MEO region, another survey method was chosen. The orbital planes of GNSS satellites were investigated one after another. In the orbital planes, pseudo-objects were defined with equidistant spacing. The distance between two pseudo-objects was equal to the FoV of ZimSMART which ensured a complete coverage of the orbit. After each field around a pseudo-object was observed several times, the orbital plane was changed. With this method the orbital planes of satellites of the NAVSTAR GPS, GLONASS, Galileo and Molniya system, respectively, could be investigated. As a disadvantage, observed objects in one orbital plane are not or only by chance observed when investigating another orbital plane. Tasked follow-up observations have to be performed with another telescope to maintain the orbits of these objects.

After the observations were extracted into tracklets, the object identification process had to be performed. The implemented processing pipeline *ZimPipe* compared the positions and determined velocities to those based on catalogued objects. When the deviation of one tracklet was within the defined limits, it was associated to that object. Tracklets, which were associated to object of the AIUB internal catalogues, were confirmed by an orbit determination and removed from further analysis.

Tracklets, which could not be filtered, were tested pairwise whether some of them belong to the same object, successful connections were called "object candidates". This led to more accurate results in the subsequent filter step, where the orbital elements of objects of the AIUB internal ZimSMART catalogue were compared to those of the "object candidates", than comparing just the single tracklets. Here again, when the deviations were below estimated limits, the tracklets were associated to the objects and confirmed with an orbit determination.

"Object candidates", which were not filtered to an object are stored into the catalogue as new detections. Also the newly calculated orbits are stored and used for the processing pipeline in the following night with observations.

The statistical analysis of the catalogue came to the results that maintaining a subcatalogue of GEO objects is hardly possible, approximately 77 % of the objects were lost after three nights. For GTO objects the fraction after three nights is much higher, about 83 % of the objects were lost. This means, a maintenance of a larger of a catalogue is only possible when a second telescope is used, which acquires follow-up observations.

When observing active satellites, either on purpose or by chance, the identifications process gets difficult in case of manoeuvres. Two kinds of manoeuvres were discussed: the East-West station keeping (EWSK) manoeuvre, which changes the shape of an orbit and the North-South station-keeping (NSSK) manoeuvre, which changes the orientation of the orbital plane.

The analysis based on the propagation of orbital elements before and after the assumed manoeuvre to the epoch and the subsequent comparison of the position and velocity vectors. Ideally, the position vectors would be equal, and the velocity vector would only differ by the thrust vector. In reality, there were deviations from the ideal case due to the uncertainties from the orbit determination.

Firstly, manoeuvres were investigated, from which epoch and thrust vector were known, to compare the determined results with the given values. These comparison were unsuccessful, the determined velocity vector components did not agree with the given components of the thrust vectors. The reasons therefore lay in the uncertainties of the orbits and the propagation to the epoch of the manoeuvre.

Secondly, manoeuvres of another satellite were investigated, from which only the epochs were given. The determined differences of the velocity vectors of the EWSK manoeuvres were with in the same range like before, but for the NSSK manoeuvres there was no data for comparison.

Thirdly, all manoeuvres were investigated again, but this time the manoeuvre epochs were assumed to be unknown. The time interval between the last orbit determination before the manoeuvre an the first thereafter was scanned with propagating both element sets to estimate the epoch with the minimum of the difference between both position vectors. The corresponding angle between the velocity vectors were also estimated. With this scanning method the EWSK manoeuvres could be identified with a maximum deviation of five hours from the given epochs, apart from special cases where the minima were not distinct. The epochs of the NSSK manoeuvres are more difficult to identify, while one was accurate to 26 min, the other differed by 735 min, which was approximately half an orbital period.

The identification of NSSK manoeuvre epochs might only be accurate to a natural number of half-integral orbital periods, especially when the time interval between both used orbital element sets is large. In contradiction, the identification of EWSK manoeuvre epochs is more accurate, when the element sets do not carry large errors.

The last part of this thesis was not related to catalogue built-up and maintenance directly. When analysing the AMR value variation, a sinusoidal variation appeared for most HAMR objects. An investigation of the cosine curve led to the results that the estimated AMR values depended on the distance between the Sun and the Earth. In the source code of *SATORB* there was a factor wrongly applied and after removing this factor, all objects only showed specific variation.

List of Publications

> When you write a story, you're telling yourself the story... When you rewrite, your main job is taking out all the things that are not the story.
>
> Stephen King

Papers

J. Herzog, C. Früh, T. Schildknecht
   "Build-up and maintenance of a catalogue of GEO objects with ZimSMART and ZimSMART 2", In Proceedings of the 61st International Astronautical Congress, Prague (Czech Republic), 2010

J. Herzog, T. Schildknecht, M. Ploner
   "Space Debris Observations with ZimSMART", In Proceedings of the European Space Surveillance Conference, Madrid (Spain), 2011

J. Herzog, T. Schildknecht
   "Search for space debris in the MEO region with ZimSMART", In Proceedings of the 63rd International Astronautical Congress, Naples (Italy), 2012

J. Herzog, T. Schildknecht, A. Hinze, M. Ploner, A. Vananti
   "Long-term evolution of orbits of high area-to-mass ratio objects in the Geostationary Ring", In Proceedings of the 61. Deutscher Luft- und Raumfahrtkongress, Berlin (Germany), 2012

J. Herzog, T. Schildknecht
   "Analysis of the long-term area-to-mass ratio variation of space debris", In Proceedings of the 2012 Advanced Maui Optical and Space Surveillance Technologies Conference, Maui (United States of America), 2012

J. Herzog, T. Schildknecht, A. Hinze, A. Vananti
   "Space Surveillance Observations at the Zimmerwald Observatory", In Proceedings of the Sixth European Conference on Space Debris, Darmstadt (Germany), 2013

Co-authored papers

S. Kaufmann, L. Gérard, S. Wagner, M. Hauser, J. Herzog
   "Multiwavelength view of the TeV Blazar RGB J0152+017", In Proceedings of the 31st International

Cosmic Ray Conference, Łódź (Poland), 2009

M. Ploner, T. Schildknecht, C. Früh, A. Vananti, J. Herzog
"Space Surveillance Observations at the Zimmerwald Observatory", In Proceedings of the Fifth European Conference on Space Debris, Darmstadt (Germany), 2009

T. Schildknecht, C. Früh, J. Herzog, A. Hinze, A. Vananti
"Efforts to Survey, Track, and Characterize Small-Size Objects at High Altitudes", In Proceedings of 2010 Advanced Maui Optical and Space Surveillance Technologies Conference, Maui (United States of America), 2010

T. Schildknecht, C. Früh, A. Hinze, J. Herzog
"Dynamical Properties of High Area to Mass Ratio Objects in GEO-Like Orbits", In Proceedings of the 38th COSPAR Scientific Assembly, Bremen (Germany), 2010

T. Schildknecht, W. Flury, C. Früh, J. Herzog, A. Hinze, A. Vananti
"Using Optical Observations to Survey, Track, and Characterize Small-Size Objects at High Altitudes", In Proceedings of the 28th International Symposium on Space Technology and Science, Okinawa (Japan), 2011

T. Schildknecht, A. Vananti, A. Hinze, J. Herzog, H. Krag
"Results of Optical Surveys for Space Debris in MEO", In Proceedings of the 62nd International Astronautical Congress, Cape Town (South Africa), 2011

T. Schildknecht, J. Herzog, A. Hinze, A. Vananti, M. Ploner
"AIUB Efforts to Survey, Track, and Characterize Small-Size Objects at High Altitudes", In Proceedings of the 61. Deutscher Luft- und Raumfahrtkongress, Berlin (Germany), 2012

K. Fujimoto, D. Scheeres, J. Herzog, T. Schildknecht
"Association of Short-Arc Optical Tracks via the Direct Bayesian Admissible Region: Theory and Application", In Proceedings of the Sixth European Conference on Space Debris, Darmstadt (Germany), 2013

Appendix

Two Line Element Format

> I have no special talents. I am
> only passionately curious.
>
> ———————————
> Albert Einstein

The Two Line Elements set (TLE) format is a worldwide standard format for orbital elements and other parameters of objects orbiting around the Earth. At AIUB, it is a second possibility to present the internal orbital elements catalogue. Orbital elements in this form are mainly used to calculate ephemerides in the planning phase of observations.

Figure A.1: Construction of a Two Line Element set (taken from [Vall 06]. Shaded cells must not contain data, the letter S indicates space for a sign ($+$, $-$ or blank), E is the exponent to the base 10.
Eccentricity, mean motion derivative and *Bstar* imply a decimal point before their first digit.
The mean motion derivative is divided by 2 and in units of rev/day^2, the second mean motion derivative is divided by 6 and in units of rev/day^3

In brief, the entries are as follows; a more detailed explanation can be read in [Vall 06]:

1. The number of the line is represented by the first digit in each line to avoid ambiguities when listing several TLEs.

2. The second number in both lines is the object number in the catalogue of the North American Aerospace Defense Command (NORAD), a joint organisation of Canada with the USA. The numbering is continuous according to the first observation, starting with 00001 for the rocket body of Sputnik 1. For a valid TLE the NORAD number has to be repeated in the second line at the very columns.

3. The following letter shows the class of the object. Only unclassified objects, displayed by "U" or a blank, are publicly available.

133

4. The International Lauch Designator was assigned in accordance of the "Convention on Registration of Objects Launched into Outer Space". The designator consists of five digits and a set of letters, where the first two digits represent the year of the launch and the other three digits stand for the launch number of that year. The last three columns in the TLE are reserved for the number of pieces of that launch which could be detected. It goes from A, B...Z, AA, AB...

5. The epoch for which the elements were determined consists of the two-digit year number. It is followed by the day of that year with the fraction thereof, i.e. the time in UTC divided by 24.

6. The mean motion derivative is given in revolutions per day squared and it can be preceded by a minus sign, a blank has the same meaning as a plus sign. The given value was already divied by 2 to use it directly for calculations in the SDP/SGP model.

7. The second mean motion derivative is given in revolutions per day cubed and is also used for the SDP/SGP model. There is an implicit decimal point before the first digit, which can also be preceded by a sign or a blank. At the end there is a signed exponent to the base ten; a blank is interpreted as a plus sign. Mostly this quantity will be given as zero, otherwise it is already divided by 6 to use it directly in the SDP/SGP model.

8. The format of *Bstar* is similar to the one before: a possible sign, followed by an implicit decimal point and five digits. The last columns are a signed exponent to the base ten. The quantity *Bstar* is a drag-like coefficient in the SGP4-model and adjusts the ballistic coefficient B_c. It is a free modelling parameter and may not be correlated to drag effects, which might be the fact in cases of satellite manoeuvres, Solar radiation pressure or large third body effects. For objects in the LEO region atmospheric perturbations or insufficient modelling of the gravitational potential of the Earth may also affect that quantity.

9. The model, with which the TLEs are generated, can be read from the ephemeris type. In [Vall 06] the authors suggest a number coding, but in general there might be a zero or blank, which stands for the SGP4/SDP4 model.

10. The element number is a continuous number and is increased for each new determined data set.

11. The entries of the second line show the orbital elements to the given epoch in the following order: inclination in degrees, right ascension of the ascending node in degrees, eccentricity with implicit leading decimal point, argument of the perigee in degrees, mean anomaly at epoch in degrees, mean motion in revolutions per day. The reference frame is a geocentric coordinate system with the true equator and mean equinox at given epoch.

12. The number of fully performed revolutions at epoch is written in five digits. In NORAD's convention a revolution starts when the object passes its ascending node. The time span until reaching the ascending node for the first time is called revolution zero, thereafter starts revolution one. However, for uncorrelated space debris this information is not available and these columns are filled with blanks.

13. The last column in each row stands for a check sum modulo 10. The digits of a line are summed up, ignoring decimal points, letters, plus signs and blanks. Each minus sign is interpreted as a digit 1.

Most uncertainties of the calculated ephemerides or propagated elements will be the result of the limited accuracy in the TLE format, given in Tab. A.1. The epoch is given with an accuracy of 1×10^{-8} d, which is equal to 8.64×10^{-4} s. For GEO objects with a velocity of about $3\,\mathrm{km\,s^{-1}}$, the uncertainty in epoch leads to an uncertainty of about $2.6\,\mathrm{m}$ of the position along the orbit. The inclination, the RAAN and the argument of the perigee are given with an accuracy of $1 \times 10^{-4\circ}$. The accuracy of the eccentricity is 1×10^{-7}, while that of the mean motion is at $1 \times 10^{-8}\,\mathrm{d^{-1}}$.

Table A.1: Accuracy of orbital elements in the TLE sets

Orbital element	Accuracy	Unit
Epoch	1×10^{-8}	d
Inclination	1×10^{-4}	°
RAAN	1×10^{-4}	°
Eccentricity	1×10^{-7}	
Argument of perigee	1×10^{-4}	°
Mean anomaly	1×10^{-4}	°
Mean motion	1×10^{-8}	d^{-1}

With $\delta_a \sim n^{-5/3} \delta_n$ the uncertainty of the semi-major axis of a geosynchronous object becomes approximately 6.31×10^{-4} km and can be neglected. The uncertainty of the geocentric distance is of the order of $\delta_r \sim a\delta_\varepsilon$ and for GEO objects of about $4\,$m. The uncertainty in the direction perpendicular to the orbital plane is $\sim a\delta_i$ and with about $74\,$m much larger.

Appendix A. Two Line Element Format

Appendix B

Flowchart Diagram of *ZimPipe*

> And you will find someday that, after all, it isn't as horrible as it looks.
>
> —— Richard Feynman

Unlike Fig. B.1, Fig. 3.4 on Page 75 does not give a detailed view on the processing pipeline. Figure B.1 does not only show the way of the tracklets, but also the orbital elements catalogue, which are needed for the processing step with *COROBS*. The colour-coded arrows display the ways of unfiltered, unassociated and single tracklets in light green, and associated tracklets in dark green. "Object candidates" and new detections are shown with blue arrows, while the successful associations are in orange. Orbital elements for the input are displayed with black arrows and updated orbital elements in grey.

The boxes in black show the databases for the observations and orbital elements, respectively. The individual subroutines of the pipeline are displayed in the boxes with transparent green colour.

Figure B.1: Detailed flowchart of the processing pipeline *ZimSMART*

Appendix C

Acknowledgements

> I don't know half of you half as
> well as I should like; and I like
> less than half of you half as well
> as you deserve.
>
> John Ronald Reuel Tolkien

Appendix C. Acknowledgements

[ASAa] ASA. *ASA Astrograph N f 3.6*. Webpage, `http://www.astrosysteme.at/de/astrographen_n-serie.html`. Retrieved January 05, 2013.

[ASAb] ASA. *ASA Direct Drive Montierung DDM85*. Webpage, `http://www.astrosysteme.at/de/montierung_ddm85.html`. Retrieved January 05, 2013.

[Basc 05] B. Baschek and A. Unsöld. *Der Neue Kosmos*. Springer-Verlag, Berlin, Heidelberg, New York, 7th Ed., 2005.

[Beut 05] G. Beutler. *Methods of Celestial Mechanics*. Springer-Verlag, Heidelberg, 2005.

[Bron 01] I. N. Bronštein *et al*. *Taschenbuch der Mathematik*. Verlag Harri Deutsch, Thun und Frankfurt am Main, 5th Ed., 2001.

[Clar 45] A. C. Clarke. "Extra-terrestrial Relays". *Wireless World*, Vol. LI, No. 10, pp. 305 – 308, October 1945.

[Clop 34] C. Clopper and E. Pearson. "The use of confidence or fiducial limits illustrated in the case of the binomial". *Biometrika*, No. 26, pp. 404–413, 1934.

[CNES] CNES. *Protected Regions*. Webpage, `http://www.cnes.fr/web/CNES-en/5003-concrete-recommendations.php`. Retrieved July 11, 2011.

[DLR] DLR. *ROSAT re-entered atmosphere over Bay of Bengal*. Webpage, `http://www.dlr.de/dlr/en/desktopdefault.aspx/tabid-10081/151_read-1779/`. Retrieved December 14, 2011.

[EUMETSAT] EUMETSAT. *Orbital data*. Webpage, `http://www.eumetsat.int/Home/Main/Satellites/orbital_parameters`. Retrieved March 19, 2012.

[FLI] FLI. *CCD Camera ProLine PL16803*. Webpage, `http://www.flicamera.com/spec_sheets/PL16803.pdf`. Retrieved January 03, 2013.

[Floh 09] T. Flohrer *et al*. "Improving ESA's Collision Risk Estimates by an Assessment of the TLE Orbit Errors of the US SSN Catalogue". In: *Proceedings of the Fifth European Conference on Space Debris*, 2009.

[Floh 11] C. Flohrer *et al*. "Generating precise and homogeneous orbits for Jason-1 and Jason-2". *Advances in Space Research*, No. 48, pp. 152–172, 2011.

Bibliography

[Früh 11]   C. Früh. *Identification of Space Debris.* Shaker Verlag, 2011.

[HeavAb]   "Height of the ISS". Retrieved May 31, 2013.

[Herz 12a]   J. Herzog *et al.* "Long-term evolution of orbits of high area-to-mass ratio objects in the Geostationary Ring". In: *Proceedings of the 61. Deutscher Luft- und Raumfahrtkongress*, 2012.

[Herz 12b]   J. Herzog and T. Schildknecht. "Analysis of the long-term area-to-mass ratio variation of space debris". In: *Proceedings of the Advanced Maui Optical and Space Surveillance Technologies Conference*, 2012.

[Hiro 10]   C. Hirose *et al.* "Evaluation of the TLE prediction errors for conjunction assessment". In: *Proceedings of the 61st International Astronautical Congress*, 2010.

[IAA 93]   IAA. "Orbital Debris". *Acta Astronautica*, Vol. 31, pp. 169–191, 1993.

[IADC 02]   IADC. *IADC Space Debris Migitation Guidelines.* `http://stage.tksc.jaxa.jp/spacelaw/kokusai_utyu/space_debris2/IADC.pdf`, 2002. Retrieved June 1, 2012.

[IGS ACC]   IGS ACC. *Final Orbits (AC solutions compared to IGLOS Final).* Webpage, `http://acc.igs.org/`. Retrieved August 22, 2011.

[Kaul 66]   W. M. Kaula. *Theory of Satellite Geodesy.* Blaisdell Publishing Company, Waltham, Toronto London, 1966.

[Kopp 11]   G. Kopp and J. L. Lean. "A new, lower value of total solar irradiance: Evidence and climate signifcance". *Geophysical Research Letters*, Vol. 38, No. L01706, 2011.

[Liou 10]   J.-C. Liou. "A parametric Study on using active Debris Removal for LEO Environment Remediation". In: *Proceedings of the 61st International Astronautical Congress*, 2010.

[Mont 00]   O. Montenbruck and E. Gill. *Satellite Orbits.* Springer, Berlin Heidelberg New York, 2000.

[Mulr 08]   M. Mulrooney *et al.* "A new Bond Albedo for performing Orbital Debris Brightness to Size Transformations". In: *Proceedings of the 59th International Astronautical Congress*, 2008.

[Musc 10]   R. Musci *et al.* "Analyzing long observation arcs for objects with high area-to-mass ratios in geostationary orbits". *Acta Astronautica*, No. 66, pp. 693–703, 2010.

[NASAa]   NASA. *Planetary data.* Webpage, `http://nssdc.gsfc.nasa.gov/planetary/factsheet/`. Retrieved September 12, 2011.

[NASAb]   NASA. *UARS re-entry overview.* Webpage, `http://www.nasa.gov/mission_pages/uars/index.html`. Retrieved December 14, 2011.

[NASAc]   NASA. *Vanguard 1.* Webpage, `http://nssdc.gsfc.nasa.gov/nmc/spacecraftDisplay.do?id=1958-002B`. Retrieved February 21, 2011.

[Noor 29]   H. Noordung. "Das Problem der Befahrung das Weltraums – der Raketenmotor". 1929.

[Paramount]   Paramount. *Paramount ME Web Site.* Webpage, `http://www.bisque.com/help/paramountme/technicalspecs_intro.htm`. Retrieved January 07, 2013.

[Payn 03]   T. P. Payne. "New Deep Space Optical Search Strategies". In: *Proceedings of the Fifth US/Russian Space Surveillance Workshop*, 2003.

[Ries 92]   J. Ries *et al.* "Progress in the determination of the gravitational coefficient of the Earth". *Geophys. Res. Letters*, Vol. 19, No. 6, pp. 529–531, 1992.

[Schi 03]   T. Schildknecht. *The Search for Space Debris in High-altitude Orbits.* PhD thesis, Universitiy of Bern, November 2003.

[Schi 04]   T. Schildknecht *et al.* "Optical obervations of space debris in GEO and highly-eccentric orbits". *Advanes in Space Research*, No. 34, pp. 901–911, 2004.

[Schi 07]   T. Schildknecht. "Optical surveys for space debris". *Astronomy & Astrophysics Review*, No. 14, p. 41, 2007.

[Schi 09]   T. Schildknecht *et al.* "Optical Surveys for Space Debris in MEO – Simulations and First Results". In: *Proceedings of the* 60th *International Astronautical Congress*, 2009.

[Soop 94]   E. Soop. *Handbook of Geostationary Orbits.* Microcosm, Inc. Torrance (USA); Kluwer Academic Publishers Dordrecht Boston London, 1994.

[Takahashi]   Takahashi Europe. *Takahashi Europe, ε-180AD, Optical specifications.* Webpage, `http://www.takahashi-europe.com/en/epsilon-180ED.specifications.php`. Retrieved January 05, 2013.

[Thal 11]   D. Thaller *et al.* "Combination of GNSS and SLR orbservations unsing satellite co-locations". *Journal of Geodesy*, No. 85, pp. 257–272, 2011.

[Vall 06]   D. A. Vallado *et al.* "Revisiting Spacetrack Report #3: Rev 1". Tech. Rep., American Institute of Aeronautics and Astronautics, 2006.

[Wang 09]   R. Wang *et al.* "Propagation errors analysis of TLE data". *Advances in Space Research*, No. 43, pp. 1065–1069, 2009.

Erklärung

Gemäss Art.28 Abs.2 RSL 05

Name	**Herzog, Johannes**
Matrikelnummer	**09-121-575**
Studiengang	**Astronomie**
	Dissertation
Titel der Arbeit	**Cataloguing of Objects on High and Intermediate Orbits**
Leiter der Arbeit	**Prof. Dr. Thomas Schildknecht**

Ich erkläre hiermit, dass ich diese Arbeit selbständig verfasst und keine anderen als die angegebenen Quellen benutzt habe. Alle Stellen, die wörtlich oder sinngemäss aus Quellen entnommen wurden, habe ich als solche gekennzeichnet. Mir ist bekannt, dass andernfalls der Senat gemäss Artikel 36 Absatz 1 Buchstabe r des Gesetzes vom 5. September 1996 über die Universität zum Entzug des auf Grund dieser Arbeit verliehenen Titels berechtigt ist.

Bern, 8.10.2013   Unterschrift

2008 – 2013 PhD student
Astronomical Institute,
University of Bern, Switzerland
Thesis title: *Cataloguing of Objects on High and Intermediate Altitude Orbits*
Supervisor: Prof. Dr. T. Schildknecht, University of Bern, Switzerland
Co-Referee: Prof. Dr. P. Seitzer, University of Michigan, United States of America

Sep 2008 Diploma (M.Sc.) in Physics,
Department of Physics and Astronomy,
University of Heidelberg, Germany

Aug 2007 – Aug 2008 Master thesis
Landessternwarte,
University of Heidelberg, Germany
Title: *Analysing the photometric accuracy of ATOM exemplified by RGB J0152+017*
Supervisor: Prof. Dr. S. Wagner, University of Heidelberg, Germany
Co-Referee: Prof. Dr. I. Appenzeller, University of Heidelberg, Germany

2005–2008 Graduate student
Department of Physics and Astronomy,
University of Heidelberg, Germany

2005 Vordiplom (B.Sc.) in Physics,
Department of Physics and Astronomy,
University of Heidelberg, Germany

2003–2005 Undergraduate student
Department of Physics and Astronomy,
University of Heidelberg, Germany

2002 Abitur (High School Diploma)
Georg-Cantor-Gymnasium, Halle (Saale), Germany